https://ntrs.nasa.gov/search.jsp?R=19650024800 2018-05-25T16:16:22+00:00Z

FINAL REPORT ON BELL TELEPHONE LABORATORIES EXPERIMENTS ON EXPLORER XV

PROJECT SERB

STUDY ON THE ENHANCED RADIATION BELTS

CONTRACT NAS 5-3058

June 30, 1964

PREFACE

Project Serb was conceived and executed within a remarkably short period of time. Less than eight weeks elapsed between project approval and launch. It is a tribute to those who planned, directed, built and tested in those often frantic weeks that the satellite achieved its prime objective of surveying the electron distribution as altered by high altitude nuclear tests. Particular acknowledgment is due to John Townsend who kept his finger on the pulse of the project from start to finish and to Gerry Longanecker and Paul Butler of the Project Office who saw it through. The Bell Laboratories collaborators on the program are also tremendously indebted to Roland Van Allen and U. Desai who fought with and successfully solved the problems of the digital circuitry into which the BTL experiments fed their information.

FACILITY FORM 602

N65-34401 (ACCESSION NUMBER)

(THRU) 1

159 (PAGES)

(CODE) 29

CR 67106 (NASA CR OR TMX OR AD NUMBER)

(CATEGORY)

GPO PRICE $

CFSTI PRICE(S) $

Hard copy (HC) 5.00

Microfiche (MF) 1.00

ff 653 July 65

5QT-38780

I. Introduction

The work carried out under this contract consists of two main tasks. The first is a study of the energetic particles in the trapped radiation belts in space, particularly the electrons artificially introduced by high altitude nuclear explosions during 1962. This task has involved fabrication, testing, and calibration of instrumentation for particle measurements and reduction and analysis of the data received from the satellite in space. The second is an investigation of the radiation damage to solar cells due to the particle exposure of Explorer XV in its orbit. It has included design, fabrication and testing of solar cell damage detectors and reduction and analysis of the data from space. A detailed account of these two main tasks is given in Sections II and III below.

The work of designing and constructing the hardware of the Bell Laboratories experiment was done by a group of people who had worked together on the Telstar program and in part on the BTL experiments of Project Relay.

T. M. Buck, G. H. Wheatley, J. W. Rodgers and W. M. Augustyniak who built and tested the particle detectors;

G. L. Miller (then of Brookhaven National Laboratories), E. W. Thomas and L. V. Medford who designed and tested the circuitry of the particle experiments;

CASE FILE COPY

P. T. Haury and J. E. Austin, who directed the fabrication of the circuit packages;

G. B. Skewis and members of Branch Shop #3 who did the mechanical fabrication of the particle detector hardware;

H. K. Gummel, B. H. McGahey and D. B. Cuttriss who designed. built and tested the solar cell damage experiment.

A newcomer to space projects, Mrs. W. L. Mammel deserves a special note of recognition. It was she who handled with imagination, persistence, and elegance the complex problems of data reduction required for these experiments.

W. L. Brown was responsible for the project.

II. The Particle Experiments

2.1 The Design of the Experiments

2.1.1 The Experimental Objectives

The particle experiments were designed to measure the distribution of electrons in the trapped radiation belts with good spatial and time resolution and to provide information on the spectral characteristics and angular distribution of these particles. The primary intent was to study the injection of new electrons into the trapping region by high altitude nuclear explosions and the subsequent disappearance of these particles by atmospheric scattering and other loss mechanisms. Explorer XV was launched on October 27, 1962, three and one-half months after the U.S. Starfish[1] nuclear test in the Pacific and five days after a high altitude nuclear test by the Soviet Union on October 22. On October 28, a few hours after launch, the satellite observed the addition of new particles as a result of a second Soviet high altitude test. Four days later, on November 1, it detected electrons from the third test in the Soviet series. There were thus opportunities to observe transient phenomena associated with impulsive injections of particles at widely different phases of their time history. With its apogee at about 4 earth radii, in the outer Van Allen electron belt, Explorer XV was able to measure the natural fluctuations[2] in the properties of that particle population. It was also possible to carry out measurements on relatively low energy protons whose distribution in space had not previously been determined.

2.1.2 The Particle Detectors

All of the particle experiments by Bell Laboratories on Explorer XV made use of semiconductor p-n junction detectors as their particle-sensitive elements. Figure 2-1 shows a cross-section of one of these devices as developed by Buck, et al[3] originally for use on the Telstar satellite. The p-n junction region of the detector contains a high electric field developed by an applied bias potential. This region is a solid state ionization chamber in which holes and electrons created by a high energy charged particle are collected and produce an output pulse. Holes and electrons are generated in silicon in proportion to the energy lost by incident particles. Thus the output pulse of charge is in magnitude proportional to the amount of energy the particle loses in the active, field containing region of the device. This region is disc shaped in the device of Fig. 2-1, about 2.6 mm in diameter and, at 100 volt bias, about .4 mm thick. By making use of the different energy loss characteristics of electrons and protons and by changing the thickness of the active region by a change in bias, it is possible to distinguish electrons and protons from one another in this type of device. These detectors have output pulse rise times of less than .2 μsec. As a result, they can readily be used to study the particle distribution in the high intensity regions of the inner and outer Van Allen belts.

A detailed account of the design and fabrication of these detectors for reliable performance in space is given in Reference 3. Particles are intended to reach the detector through an aperture 2 mm in diameter in the lid of the can,

Fig. 2-1. This aperture is covered with a 0.3 mil Kovar diaphragm which completes the vacuum tight encapsulation of the device to avoid changes in its surface. This window also serves the important function of excluding light and very low energy particles which are heavily damaging to semiconductor devices. In the detectors of Explorer XV, additional absorbers are added in front of the Kovar window to make the minimum mass thickness seen by the particles approximately 20 mg/cm^2.

2.1.3 The Detector Complement

The experiments utilize six detectors of the type described above, mounted in different arrangements of shielding and provided with different thicknesses of absorber for measurements of electrons of different energies. Table 2-1 lists the detectors, their approximate threshold energies, their angular acceptance and their effective geometrical factors. These will be discussed in more detail in sections to follow. For all six detectors a pulse height discrimination level of approximately 0.4 Mev has been established. Detector A is unique in having a second discrimination level set at 2.7 Mev. The effective geometrical factors given in Table 2-1 apply at a detector bias of 100 volts where the detectors have an active thickness of about 0.4 millimeters. The devices are also supplied a 5 volt bias in part of the experiment. At this lower value, the active thickness is reduced to approximately .12 millimeters. This change reduces the electron detection efficiency by a factor of approximately 100 because of the low

TABLE 2-1

Detector	Channel	Pulse Height Discrim. Mev+	Absorber g/cm^2	Threshold Energies Electrons Mev	Threshold Energies Protons Mev	Full Angular Aperture	Math. Geometrical Factor cm^2 ster.	Effective Geometrical Factor for Electrons cm^2 ster.
A	E1	0.408	.020	0.5	2.1	20°	2.9×10^{-3}	6.5×10^{-4}
	E4	2.7	.020	2.8	4.0	20°	2.9×10^{-3}	
B	E2	0.411	.42	1.9	15	2π (20°)	*2.9×10^{-3}	5.5×10^{-4}
C	E3	0.408	.84	2.9	22	2π (30°)	*6.5×10^{-3}	$\sim 9 \times 10^{-4}$
D	E5	0.402	6.3	background		4π	2×10^{-1}	
E	E6	0.410	.020	0.5	2.1	10°	4.7×10^{-4}	1.6×10^{-4}
F	E7	0.413	.41	1.9	15	14°	9.4×10^{-4}	$\sim 1.5 \times 10^{-4}$

*Assuming uniform scattering over 2π solid angle for electrons penetrating a hemispherical dome.

+Energy equivalent of charge pulse required by the discriminator.

probability that an electron will leave at least 0.4 Mev in such a thin active region. The detection efficiency for low energy protons is essentially unaffected. By comparing the counting rates at 100 volts and 5 volts bias, the proton and electron components of the counting rate can be separated. For the output channel E4 with its high discrimination level, the detection efficiency for electrons is extremely small and the detector counts only low energy protons.

2.1.4 The Logic of the Experiment

A block diagram of the experiment is shown in Fig. 2-2. Each of the detectors is followed by a preamplifier, a linear amplifier and a discriminator as shown, except for Detector A which has two discriminators as noted above. There are a total of seven outputs from this detector group, five of which time share a 21 bit accumulator in the Cosmic Ray Logic box provided by GSFC.[4] The other two go to analog logarithmic ratemeter circuits also in the CRL box. The basic data taking scheme for the digital channels is as follows. One of the outputs in the E1 through E5 group feeds pulses as they are detected by the associated particle detector into the accumulator for five frame times of the telemetry encoder, a total of approximately 1.46 seconds. With accumulation interrupted, the first eighteen bits are read out in the next three telemetry frames at two words per frame and three bits per word. During the five frame counting period the three most significant bits in the 21 bit accumulator are read out repeatedly. They change very slowly and provide a measure of overflow of the 18 bit

portion of the accumulator. After the eight frame period of counting and reading with one detector output, the next output in the E1 through E5 group is examined in the same way. Three of these five outputs are counted once each 32 frames. Outputs E4 and E5, however, are further time multiplexed, with E5 being examined only once on the 5x3 count-and-read cycle in each 160 frames.

The log ratemeter circuits fed by E6 and E7 are digital to analog converters that produce an analog output in proportion to the total number of events or counts that have occurred in a fixed time. They store pulses as charge on capacitors and dump this charge when read out. Leo Davis, who has used these circuits in Explorer XII[5] and XIV as well as on Explorer XV, generously provided them for use in the BTL experiments. Each log ratemeter is read once each frame. The intent of these measurements, taken with Detectors E and F with their narrow cones of angular acceptance, is to determine the angular distribution of the trapped particles by examining the counting rates at different orientations of the satellite in its spin. To increase the angular resolution of the measurement the log ratemeters are dumped twice each frame, although they are read only once. Thus, information is stored for essentially .146 second before each readout. Because of the anomalously high spin rate of the satellite (73 rather than the expected 10 rev per min.) even this half frame storage time corresponds to 64° rotation. This is unfortunately large for obtaining useful results on the angular distribution of the trapped particles.

Electrical bias is supplied to the particle detectors from the bias box shown at the bottom of the block diagram, Fig. 2-2. The bias is switched on a 320 by 960 frame basis, all detectors being at 100 volts for 960 frames (about 280 seconds) and at 5 volts for 320 frames (about 93 seconds). This provides for distinguishing protons and electrons as described above. The change in bias has the additional important effect of increasing the detector reliability. Continuous operation at high bias in the presence of high intensity ionizing radiation in some cases leads to increases in detector noise because of increases in surface leakage currents in the device.[6] It has been found that programmed cycling of the bias between high and low values as provided in Explorer XV substantially reduces the probability of this mode of failure.

2.2 Mechanical Design and Construction

2.2.1 The Main Detector Box

The BTL detector box, assembled with the six particle detectors and their associated electronic circuits, is shown in Fig. 2-3. The two protruding turrets are omnidirectional mounts containing Detector B on the right and C on the left. In the center of the box is a block containing the other four detectors, F, E, A, and D in order clockwise starting from the upper left. There are six coaxial test jacks along the upper edge of the front of the box. One of these is connected to the input of each preamplifier so that test pulses can be introduced for checking the electronic system. These points also permit test measurements of the bias on each detector. The box as mounted on the spacecraft can be seen in Fig. 2-4. All of the detectors look out perpendicular to the spin axis of the satellite. The two omnidirectional detector mounts protrude through the cover of the satellite and view an almost unobstructed 2π solid angle. In the photograph, the block of four detectors is covered with tape to exclude dirt during spacecraft integration. These detectors have sufficiently narrow cones of particle acceptance that they do not need to protrude through the skin. The six test jacks have clearance holes which provide access for tests on the assembled spacecraft.

The main detector box is made of aluminum sheet. The detector blocks are attached to the front and bottom of the box and extend several inches inside in depth. A view of the back of the box with the cover removed is shown in Fig. 2-5. A thin sheet-aluminum crate structure supports the electronics of the six detectors in individual shielded compartments and adds rigidity to the completed assembly. Figure 2-5 was taken before final foaming of the package. The vacant spaces around the stake-on terminal arrays at the back of the box and around the detector mounts and the circuit modules are completely filled in this process.

2.2.2 Detector Mounting Blocks

The block-of-four detector mount and one of the omnidirectional detector mounts are shown in exploded view in Fig. 2-6. Engineering drawings of these two assemblies are included as Figs. 2-7 and 2-8, respectively. Each p-n junction detector, such as shown in Fig. 2-1, is enclosed in a cartridge subassembly as shown in Fig. 2-9. One of these is spread out to show its parts in front of the block-of-four mount in Fig. 2-6. The detector cartridge is fitted at the back with a gold-plated pin which plugs into a mating jack inside the mounting block. This arrangement removes the necessity of soldering the detector pigtail to the preamp circuit in a inaccessible part of the circuit assembly and

makes it possible to insert and remove detectors on the assembled spacecraft. Almost all of the parts in the detector block assembly as well as the detector box and the crate structure inside it are aluminum which is gold plated for resistance to corrosion and for good electrical contact. The electrical ground of a particle detector itself is a mechanical connection between the gold-plated Kovar can of the detector, the gold-plated aluminum cartridge, and the gold-plated aluminum detector mount. These connections have been entirely satisfactory.

The omnidirectional detectors derive their broad angular acceptance from scattering domes placed outside the spacecraft as shown in Fig. 2-4. One of these devices is seen in the assembly of Fig. 2-8 and is a part of the exploded view in Fig. 2-6. These domes receive electrons over a 2π solid angle. As the electrons penetrate the dome wall they are multiply scattered and a portion of the scattered electrons is then selected by the internal defining cone, (see Fig. 2-8) and presented to the particle detector. The probability of electron scattering through a given angle decreases with increasing angle. Thus electrons incident on the dome in a direction nearly perpendicular to the detector axis are less likely to reach the detector than those incident along the detector axis. To compensate partially for this effect the dome is elongated to provide a larger effective area for electrons incident from the side. The effectiveness of

scattering has been enhanced by choice of brass as the scattering dome material because of its reasonably high atomic number. The angular uniformity of detection efficiency in the scattering arrangement will be discussed in Section 2.4.

Since large angle multiple scattering is much less probable for protons than for electrons, protons see the detector through an aperture defined by the internal cone alone. The thickness of dome wall protons must traverse to reach the detector is not independent of angle in this dome geometry, however, and the geometrical factor changes slightly with proton energy as a result.

2.3 Electronic Circuits

2.3.1 Circuit Elements of the System

Each of the blocks in the BTL portion of Fig. 2-2 represents a circuit module of which there are four main types: the preamplifier, the linear amplifier, the discriminator, and the bias supply. Schematics of the first three of these are shown in Fig. 2-10. The circuits are similar to those used in the Telstar[7] satellites with modifications made primarily to increase the maximum counting rate of the experiments. In the preamplifier, Part A of Fig. 2-10, a speedup was accomplished by taking the faster signal from the emitter of Q_3 rather than from the collector, and by eliminating the output transformer. This decresed the rise time of the preamplifier to less than 0.1 μ sec. The time constants of the two differentiating

networks which shape the pulse were reduced to 0.5 μ sec from about 1 μ sec. The first differentiation is provided by R_8 and C_6 of the preamplifier. The second differentiation is produced by R_{16} at the output of the preamplifier and C_1, the input of the linear amplifier. The linear amplifier, Part B of Fig. 2-10, is essentially unmodified from that used in the Telstar satellites. Provision for the E_4 output channel of detector A is made by taking a lower gain from the linear amplifier as shown in modification Y in the figure. The discriminator, Part C of Fig. 2-10, is modified by changing the 600 microampere current output in the Telstar case to a 6.6 volt output in R_{18} and adding a p-n-p emitter follower to drive the cable and the following circuits. This modification eliminates the logic shaper circuit and its fairly long recovery time (10 μ sec) but it does not provide differential pulse height analysis that was available in the Telstar design.

Schematics of the detector bias supply circuits are shown in Fig. 2-11. The bias converter is essentially the same as that used in the Telstar experiments. The bias switch receives a 320 frame by 960 frame signal from the spacecraft timing circuits and turns off the bias converter during the 320 frame interval. When the bias converter is off, 5 volts is supplied to the detector from a voltage divider off of the 17.8 volt spacecraft supply. Failure of the bias supply would

be extremely serious because it is common to all experiments. As a result two independent converters and switches are used. Failure of one of the supplies or one of the bias switches will not effect the bias presented to the detectors unless one of the switches fails in such a way that one converter is always on. In this case the detector bias will be kept at the bias converter output voltage.

All circuits were designed so that any circuit failure except the very unlikely case of multiple direct shorts (including at least one resistor) will not present a load of more than 17.8 milliamps to the supply nor will it terminate the whole experiment. A circuit failure in any of the six channels cannot effect the other five.

2.3.2 Circuit Construction

With the exception of the preamplifier, the circuit elements of this system are constructed of two fiberglass epoxy circuit board wafers forming the top and bottom of a sandwich with components stacked like cordwood between them. The interconnections are wired. The preamplifier is constructed on a single board. The modules are foamed as individual blocks and mounted to "mother boards" by module component leads. Figure 2-12 shows a pair of the mother board assemblies. The block marked 17 contains a single discriminator and that marked 16, two discriminators such as are used in output channels E1

and E4. These mother board assemblies are placed in the compartments of the aluminum crate structure as seen in Fig. 2-5. Figure 2-13 shows a mother board assembly of the bias supply which is mounted in the spacecraft in a box separate from the main detector box. In this figure the two bias switch modules are still unfoamed.

2.3.3 Circuit Performance

The temperature stability of the threshold on a typical detector channel is shown in Fig. 2-14. The threshold sensitivity was measured with a pulser providing calibrated charge pulses to the preamplifier. These are expressed in equivalent particle energy as in Table 2-1. All channels operated satisfactorily from -80 to +100°C. The threshold sensitivity increased with temperature by about 35% at the extremes of this temperature range but in the conservative range of possible operating temperatures from -20 to +60°C the variation is less than ~~10%~~ 5%. Figure 2-15 shows the sensivitity of this channel as a function of the supply voltage. Over a ± 2 volt range around 17.8 volts, the voltage of the spacecraft supply rail, the variation is seen to be less than ~~5%~~ 10%.

Figure 2-16 gives the paired pulse resolution of the detector channels as a function of the pulse magnitude. The measurements were carried out with a paired pulse generator

producing two charge pulses of equal magnitude and variable spacing. The magnitude is plotted in the figure as a ratio to the threshold of the channel as defined for widely spaced pulses. The two sets of data are for a channel with a single discriminator (output E_3) and for the upper discriminator level of detector A (output E_4). At the threshold, pulses of approximately 5 microsecond separation are counted as two pulses and pulses more closely spaced are seen by the system as only one. As the magnitude is increased the minimum distinguishable time separation decreases slowly. In counting electrons in one of the p-n junction detectors, the pulse height distribution is heavily weighted to small values and the effective paired pulse separation is approximately 4 microseconds.

2.3.4 Environmental Testing

The completed units were tested at BTL between -10° and +50°C with no failures. They were also tested under swept sinusoidal vibration at flight acceptance levels with no failures. The flight 1 package, however, developed a failure in channel E1 during random vibration on the assembled flight 1 spacecraft before thermal vacuum testing. The failure was found to be due to a deposited carbon resistor which developed an open circuit during vibration. This failure was traced to a particular batch of resistors manufactured with improper adjustment of the terminal forming machine. No other failures occurred in the

test series. The flight 1 BTL package was replaced on the spacecraft by the flight 2 unit during the investigation and correction of the failure in channel E1. It was this spacecraft that was launched to become Explorer XV.

2.4 Detector Calibration

2.4.1 Detector A, Channel E_1

The detection characteristics of this detector have been measured with a Sr^{90} beta source and with monoenergetic electrons up to 2 Mev. The angular response of the detector is shown in Fig. 2-17 with the Sr^{90} source. Measurements were made with essentially point source geometry. The detector is displaced behind the truncated end of the entrance cone of the shielding block in order to reduce the probability of electron scatter into the detector, (see Figs. 2-7 and 9). The sharpness of the cutoff in the detector response near 10°, the geometrical edge of the detector aperture, indicates the success of this design.

Figure 2-18 shows the geometrical factor of the detector for monoenergetic electrons. For energies up to one Mev, an electron Van deGraaff at BTL, Murray Hill was used in these measurements, and for the higher energies, a Van deGraaff at MIT [9]. The detector's effective geometrical factor rises steeply at about 0.5 Mev as electrons succeed in penetrating a 20 mg/cm^2 entrance window and satisfying the 0.4 Mev pulse height requirement of the discriminator. The mathematical geometrical factor given in Table 2-1 is approximately 29×10^{-4} cm^2 steradian. Thus the peak efficiency of the detector, which occurs at an energy of about 1.7 Mev is between 35 and 40%. The active thickness of the silicon p-n

junction detector is .37 mm and a minimum ionizing electron will on the average lose only about .15 Mev in passing through it. The discriminator level was set considerably higher than this to avoid possible problems of detector noise. Thus the detector efficiency goes through a maximum for electrons that stop with high probability in the active thickness and slowly decreases toward higher energy as the mean energy loss drops below the discrimination level. The average geometrical factor clearly depends on the spectrum of electrons, but for an exponential spectrum with an e-folding energy of 1 Mev, the geometrical factor for electrons above 0.5 Mev is 6.5×10^{-4} cm^2 steradian.

2.4.2 Detector B, Channel E_2

The angular response of this detector is shown in Fig. 2-19 as measured with a Sr^{90} source. This detector depends on the properties of the brass scattering dome for its wide angle characteristics as described in Section 2.2.2. The curve $1/2\ (1 + \cos\theta)$ shown on the figure is the response that would be obtained if the electrons were isotropically distributed in angle when they penetrated a truly hemispherical dome. The actual dome is elongated to compensate for the incompleteness of the scattering, but the detector is nonetheless a factor of approximately 2 down in response at 90°. From the standpoint of measuring an omnidirectional flux by averaging the counting rate of this detector as the satellite rotates around its spin axis, this discrepancy is undetectable.

Figure 2-20 shows the effective geometrical factor for monoenergetic electrons up to 2.8 Mev. The brass dome, 0.42 g/cm^2 in thickness, broadens the rise of the detector response because of the statistical variability of electron energy loss in penetrating the dome. It was not feasible to extend the measurements above 3 Mev and the dashed line is a reasonable extrapolation to higher energies. Because of the variability of the electron energy loss in this relatively thick absorber, it is likely that the curve will come down at high energies only very slowly if at all. The measured curve has been approximated by an ideal step in detector effective geometrical factor from zero below a threshold to a constant value above. Using a fission electron spectrum the effective threshold is found to be 1.85 Mev. For a soft exponential spectrum with an e-folding energy of .5 Mev the threshold is found to be 1.8 Mev. These values may be compared with the estimated 1.9 Mev energy for half penetration of the shield with 0.5 Mev average penetration energy. For simplicity this detector will be said to measure electrons above 1.9 Mev.

2.4.3 Detector C, Channel E_3

This detector has a brass scattering dome .84 g/cm^2 in thickness. This is too thick to make measurements with a Sr^{90} source and too thick even using the high energy Van deGraaff to see more than the start of its energy dependence. As a result, the geometrical factor and the equivalent

threshold energy for this detector have been estimated by analogue with detector B.

2.4.4 Proton Detection in Detector A

Figure 2-21 shows the computed response of detector A to protons under the two conditions of detector bias and with the two discrimination levels corresponding to channels E_1 and E_4. The energy deposited in the detector, ΔE, rises from zero as protons are able to penetrate the 20 mg/cm^2 window of the detector. The energy deposited meets the requirements of the low discrimination threshold at an incident proton energy of about 2.1 Mev and a high threshold at approximately 4 Mev. The curve is double valued because of the lower energy loss of protons having ranges greater than the active thickness of the device (.37 mm at 100 volts bias; .105 mm at 5 volts bias as measured with 18 Mev protons from the Princeton cyclotron[10]). This double valued character of the curve defines bands of energies within which protons can satisfy the pulse height discrimination requirements. The detector will detect protons with essentially 100% efficiency within these energy bands. The effective geometrical factor of the detector for protons is essentially the mathematical geometrical factor determined by the entrance cone and aperture.

2.4.5 Directional Detectors E and F

The lower energy directional detector, detector E, is very similar to detector A in characteristics but with a smaller entrance cone. This cone was provided to improve the

angular definition of the measurements. With the high spin of the satellite a larger aperture with its associated improvement in statistics would have been more valuable.

The detector F was arranged to have a similar threshold to the omnidirectional detector B. The absorber, however, is at the bottom of the entrance cone, in the cap of the detector cartridge, in order to preserve the directional properties of the detector. The counting statistics observed in this detector are poor and as in detector E, a larger aperture angle would have been more valuable under the conditions of particle flux and at the spin rate at which the experiment was performed.

2.4.6 Background Detector D

The active device of this detector is essentially identical to those of the other five detectors. Buried in the block-of-four with a solid front plug this detector is measuring bremstrahlung from electrons stopped in the housing and the additional small contribution from protons with energies of more than 70 Mev.

2.5 Performance in Space

For most of the active life of the satellite the experiments functioned extremely well and provided a large quantity of useful data. The anomalously high spin rate of the satellite reduced the value of the directional detector information from channels E6 and E7 very seriously. Apart from this difficulty, there were two failures which affected only the results of the BTL experiments. These are discussed below.

2.5.1 Difficulty in the Encoder

Beginning on about November 9, all digital channels of BTL data began to show errors simultaneously. On November 15th the error rate was extremely high, and in fact the general trend of the data was barely visible. By November 21, however, the errors were no longer present. The predominant error seems to have been that the most significant bit of each octal number (the three bit-per-word readout of the register mentioned in Section 2.1.4) preferred to be a "1" instead of a "0". This failure in the GSFC equipment was investigated by R. Van Allen and U. Desai. The 21-bit register apparently was scaling correctly and since the failure was evident in all octal numbers read from the register, it must have occurred in the amplifier following the register or in the clamp on the voltage controlled oscillator in the encoder. The first transistor in the amplifier would be most susceptible to errors due to leakage

currents.[8] This possibility was investigated by BTL. The results show that the radiation dose at which failure in the significant transistors occur is orders of magnitude greater than the dose it is estimated they received in orbit. Thus, failure due to radiation-produced leakage does not seem to be a probable cause of failure. The actual source of failure has not been determined.

The possibility of machine-correcting the data was examined. However, it did not seem possible to correct more than the two most significant octal digits by examining the progression of the numbers. This process would have been extremely difficult and time consuming and of doubtful reliability. Since the failure cleared itself in about 10 days, attempts to carry out these corrections were abandoned.

2.5.2 Failure in Channel E3

On December 23, at approximately 0700, channel E3 at high bias suddenly became noisy. From that time until the end of Explorer XV's useful life in space, the output of channel E3 at high bias remained pinned at a counting rate of approximately 150 kc. The data at low bias showed no corresponding effects throughout this time. Failure of detectors under high bias and radiation have sometimes been observed in laboratory tests as a gradual increase in noise due to changes in the chemistry of the device surface.[6] A sudden failure such as observed

is difficult to attribute to surface changes. It is possible that detector failure of some other type occurred. Alternatively, a component within the preamplifier which sees detector bias may have broken down and generated noise only at high bias.

2.6 Data Processing

2.6.1 Data Presentation

The original digital data from the BTL experiments have been machine sorted into individual detector channels and merged with the ephemeris information concerning the position of the satellite in the McIlwain magnetic coordinates B and L.[11] Since Explorer XV is a satellite with low orbital inclination its most important motion from the standpoint of the trapped particle distribution is across lines of constant L. As a consequence the merged and sorted data is presented in machine made plots of the observed counts in each channel as a function of L. A plot is made for each half orbit of the satellite, the separation between plots being decided on the basis of maxima and minima in the L coordinate.

A plot of the results for channel E1 of Detector A for the first half orbit of the satellite in space is shown in Fig. 2-22. The abscissa is L, and the complete range of the magnetic shells accessible to the satellite is included between L = 1 and 5. This pass is outgoing (increasing in L with time) as indicated by the arrow at the top of the plot. The pass starts on October 27 at 2341, about 11 minutes after injection of the satellite into orbit. The heavy line marked B shows the trace of the satellite position in magnetic field intensity as the satellite moves to increasing values of L.

The data for channel E1 are plotted as individual points, the upper set corresponding to the detector at high bias, the lower set to the detector at low bias (see Section 2.13). Each data point is the number of counts recorded in the 21 bit register of the CRL box during the 5 frame (1.46 seconds) storage interval. The points are separated in time by 32 frames (approximately 9.3 seconds) and by a distance in L which depends on the details of the satellite orbital motion. The data sampling period is small enough to provide an almost continuous curve.

In the high bias data there are two maxima in intensity, the first at L approximately 1.4 earth radii, the second at the extreme value of L, approximately 4.5 earth radii. These correspond to the inner and outer Van Allen belt maxima. The relative importance of electrons and protons, for both of which E1 at high bias has a high sensitivity, can be seen immediately by comparison with the low bias data. In the region of the outer belt the low bias points fall below the high bias points by approximately a factor of 100. This is the effect to be expected for electrons. A similar situation exists at the smallest values of L. In the region between L = 1.8 and 3.0 however a major part of the high bias counting rate is due to protons, since the low bias rate is less than

an order of magnitude smaller. There is thus a maximum in the intensity of protons with energies above approximately 2.1 Mev (Fig. 2-21) occurring at about L = 2.0.

The large scatter in the data points at low bias in a region beyond L = 3.0 is due to statistics. At L = 3 the average number of counts recorded is approximately 20 and the statistical variations in the number measured is consistent with random particle arrival. At a value of L = 1.4 for high bias however this is not the case. The points are very smooth between L = 1.55 and 2.0, but in the region of the maximum intensity where the statistics are even better, there is a substantial scatter in successive readings. This is due to the directional properties of Detector A and to the finiteness of the counting interval for a data point. The satellite is rotating at approximately 73 rpm. In the 1.46 second sampling time for the detector output the satellite rotates 1.75 times. During one rotation the detector looks perpendicular to the local magnetic field twice. Whatever the distribution of particles in pitch angle, the flux of particles into the detector will be symmetrical around these two points. In 1.75 rotations, a minimum of 3 and a maximum of 4 passes will be made through the perpendicular, depending on the phase of the spin with respect to the encoder timing. Under very special conditions the readings from channel E1 might show a modulation as large as 4 to 3. The observed modulation is less than half this much.

Figure 2-23 gives the results of channel E1 during an inbound pass on January 3, 1963. The pass has a somewhat different trace in B than Fig. 2-22 and is more nearly equatorial between L = 1.4 and 4. The maximum L is also larger as a result of the precession of apogee of the orbit toward its maximum in latitude. The character of the outer belt electrons is quite different as the result of a large change which occurred starting on December 18, 1962. This will be discussed in more detail in Section 2.7. The maximum intensity of the inner belt is very much the same as seen in the two figures although the shape of the maximum is different because of differences in in the B variation along the orbit. Modulation arising from the directional character of the detector is apparent out to $L \approx 3.5$. In the region between L = 2.2 and 3.4 there are almost no measurable electrons. The high and low bias response of the detector are almost identical, as they would be ideally if only protons were being counted. This difference in comparison to the results of Fig. 2-22 is due to the loss in electrons which were present at the time of the earlier data. The electrons present in the slot between the inner and outer belts on October 27 were produced by the Soviet nuclear explosion on October 22. They disappeared in this region rather rapidly.

Figure 2-24 is a set of data for channel E2 on the first outgoing pass of the satellite as in Fig. 2-22. The maximum in the inner belt is not apparent in this figure. In comparison with Fig. 2-22 this shows that the peak of the inner belt for higher energy electrons is at smaller values of L. The decrease in flux on the high L side of the inner belt is steeper for the electrons greater than 1.9 Mev than for those greater than 0.5 Mev. There is also structure in the L = 1.8 to 2.0 region which does not show at the lower energies. These peaks in intensity probably are a result of the first Soviet test. There are other differences between Figs. 2-24 and 2-22: the region of the slot between the inner and outer belts is remarkably uniform in intensity between L = 2 and 3.8 at higher energies, and the rise toward the outer belt maximum occurs at large values of L. Notice that there is no scatter of the data points between L = 1.3 and 1.5 as in Fig. 2-22. Detector B is omnidirectional so that it is not subject to the same questions of the phase of satellite rotation with respect to the encoder timing. The low bias data do not follow the high bias results, depressed by a factor of 100. The spacing of the clusters of data is too large to deduce a shape for the distribution, but except in the region below L = 1.5, where the electrons make a substantial difference, the low bias response is probably due to protons of greater than 15 Mev.

Figure 2-25 is a set of data for the same pass as Figs. 2-22 and -24 but for output channel E4. There is a single maximum at L approximately 1.85 in the high bias results. These are protons above 4 Mev. The low bias data are at such low counting rates that no systematic shape is distinguishable. The detector may count in this mode due to a very narrow band of protons as shown in Fig. 2-21, but it also may count due to background particles penetrating the absorber outside the acceptance cone.

All of the data for the output channels of detectors A through D have been plotted in this way to provide direct inspection of the conditions of the experiment and the manipulation of the data and to permit examination of at least the qualitative results. There are a maximum of 9 half orbits of Explorer XV per day. Thus there are 9 plots for each output channel per day, a total of about 4000 plots for the life of the satellite. Visual inspection of plotted results is surprisingly quick and a week of data can be scanned in about one hour.

2.6.2 Data Interpolation

The data have a number of features which need to be preserved and yet the number of data points is too large to work with in its entirety in a reasonable way. With a point every 9.3 seconds, a pass from maximum to minimum L, requiring about 2.7 hours, contains over a thousand data

points for a single detector channel such as E1. The high density of points can be used in either of two ways. In regions where the flux of particles is not changing rapidly with L, the large number of data points can be used to improve the statistical definition of that flux, by taking some sort of average. In regions where the flux dependence on L is very sharp, such as the bottom edge of the lower belt in Fig. 2-23 and the peaks near L = 1.9 in Fig. 2-24, the fineness in the grain of the data can be used to define the position and shape of such structure. There are, of course, places where the data for a particular channel is nonexistent, either because it wasn't received from the satellite in suitable form for processing or more often because the programmed bias changes produce holes in the high bias data and clusters of points at low bias. An elaborate system of machine smoothing and interpolation has been used to provide values of the counting rate or flux at specific values of L. These 62 L values are listed in Table 2-2 below.

TABLE 2-2

1.10	1.26	1.45	1.76	1.92	2.2	2.8	3.8
1.12	1.28	1.50	1.78	1.94	2.25	2.9	4.0
1.14	1.30	1.55	1.80	1.96	2.3	3.0	4.2
1.16	1.32	1.60	1.82	1.98	2.35	3.1	4.4
1.18	1.34	1.65	1.84	2.00	2.4	3.2	4.6
1.20	1.36	1.70	1.86	2.05	2.5	3.3	4.8
1.22	1.38	1.72	1.88	2.1	2.6	3.4	
1.24	1.40	1.74	1.90	2.15	2.7	3.6	

The spacings between these chosen L lines is small in the region of the very rapid rise at the bottom of the inner belt and between L = 1.7 and 2.0 where new particles were introduced with detailed structure by the Soviet explosions in October and early November. It has been found necessary to use different processes of smoothing and interpolation in different parts of the coordinate space in order to get satisfactory results. Smoothing of the E1 response has been accomplished with a mathematical filter at the appropriate frequency.[12] The actual mathematical form of the L and B dependence of the flux of any particular class of particles is not known, particularly in the complicated time immediately following injection of new particles, and a visual criteria of satisfactory interpolation has been required.

Figure 2-26 is a replot of the data shown in Fig. 2-22. The machine interpolated values are indicated on the figure by small plus signs for high bias and small minus signs for low bias. The plus signs are almost indistinguishable from the data except where there are low bias breaks. A judgment of the correct curve in the low bias case is, of course, made more difficult because of the broad spacings between the neighboring sets of points, and it is not obvious that the machine choice around L = 1.6 is ideal. One way of expressing the degree of satisfaction with the interpolated results is to ask how nearly they fit on the curve one would

have drawn by hand through the existing points. This "eyeball" criteria is a remarkably severe one for the computer to satisfy. At places where this criteria shows the machine values are incorrect or where the machine has interpolated across regions where structure may exist, the L-tables are edited accordingly.

2.6.3 Gamma Correction

For an omnidirectional detector such as detector B, the observed counting rates can be converted to omnidirectional flux simply by use of the effective geometrical factor of the detector. This is not the case, however, for a directional detector such as detector A. The detector looks out at right angles to the spin-axis of the satellite and measures an average flux as the satellite rotates which is not in general equivalent to the omnidirectional flux because of the anisotropic distribution of the particle pitch angles in the local magnetic field. The geometry of this situation is shown in Fig. 2-27. Here the spin-axis ω makes an angle γ to a local field vector B. The detector is shown as a cone whose axis rotates around ω. When $\Delta = 0$ and π the cone is looking out perpendicular to the magnetic field. At $\Delta = \pi/2$, the detector is looking out at angle $\pi/2 - \gamma$ with respect to the field. Trapped particle flux may be defined in terms of the local pitch angle distribution $f(\cos \alpha)$ where α is the angle between a particle's velocity vector and B. Ordinarily,

$f(\cos\alpha)$ has a maximum at $\cos\alpha = 0$, that is for particles moving at right angles to the field line and thus mirroring at the position of the satellite. If $\gamma = 0$, the detector is always looking perpendicular to B as well as to ω, and the average flux it will observe will be higher than the true omnidirectional flux, the average over an entire sphere. However, if $\gamma = \pi/2$, the detector cuts through the perpendicular to B twice each rotation, and also looks parallel to B twice each rotation, and its average is less than the average over a sphere. A γ correction is needed for this effect.

Figure 2-28 shows the ratio of the omnidirectional flux to the average directional flux as measured in a detector with 20° full cone angle (Detector A). The various curves are for different particle distributions all of which were assumed to be of the form $\varphi = \sin^n \alpha$. For $n = 2$ the distribution is rather broad and the detector only fails to measure the omnidirectional value of the flux by about 30%. At $n = 64$, however, the distribution is sharply confined near $\alpha = \pi/2$ and the discrepancy becomes 1.55 at $\gamma = 90°$ and .195 at $\gamma = 0$.

The γ correction is carried out in an iterative process, since it depends on the local pitch angle distribution which in turn depends on the change in intensity as a function of B along a given L line. The uncorrected data as a function of B, interpolated as in Section 2.6.2 to a

particular field line, is used to derive an approximate equitorial pitch angle distribution for that line.[13] This is then transformed along the line to the position of a particular data point in B, to produce the local pitch angle distribution. With this local distribution the individual data point can be corrected for γ. All the points on the line are similarly handled and the first corrected set of data produced. This is then used to derive a new equitorial pitch angle distribution and the iteration continues. In the first attempts at γ correction, the local pitch angle distribution was approximated by functions of the form $\sin^n \alpha$, like those in Fig. 2-28. This constraint on the local pitch angle distribution has been removed and the γ correction is carried out by use of a matrix. The response of a particular detector to a conical shell of particles in a narrow interval of local pitch angle is computed for various values of γ and for various narrow shells. This matrix of numbers then makes it possible to deduce the correction for any value of γ (by interpolation between the matrix entries) and for any local pitch angle distribution, by properly weighting the response to the original narrow shells of particles.

2.7 Results

2.7.1 Early Data

On October 22, 28, and November 1, the Soviet Union carried out three nuclear tests which introduced new particles into the radiation belt in the region above L = 1.7. The second of these occurred only a few hours after the Explorer XV Satellite had been put into orbit. Figure 2-29 illustrates the observations of channel E1 for the first passes of October 28. The figure is a φ,L plot of the omnidirectional flux of electrons with energies >0.5 Mev. On these particular orbits the satellite was nearly equitorial in the magnetic coordinate space so that the figure is an almost equitorial representation of the particle distribution. The curve marked 1′ was obtained on the second half of the first orbit of Explorer XV as it returned from apogee at an L of approximately 4.4. This pass crossed L = 2 at 0407 on October 28. Curve 1′ clearly shows the inner side of the outer electron belt, the slot, and the rise toward the inner belt maximum. Curve 2 is the outgoing half of the next orbit and the particle distribution has radically changed with the addition of electrons above L = 1.8. This orbit crosses L = 2 about one hour after the orbit 1′. The initial transient of new particles is not yet complete at this time as evidenced by the further increase in flux seen on the returning half of the second orbit some four hours later, curve 2′. The fortuitious observation of this transient illustrates the

longitudinal drift of magnetically trapped particles. At L = 2 on orbit 2 the satellite is over the Altantic and observing electrons which have drifted eastward around the world from their injection by the explosion over Asia. For 0.5 Mev electrons the drift rate on L = 2 is approximately 5.7°/min.[14] For the 270° of longitudinal drift required, the corresponding time is 47 minutes. On L = 3, the drift rate is 3.8°/min. During the time between its passage across L = 2 and 3, the satellite is moving eastward at approximately 1°/min. On all of the significant L shells the particles are thus drifting faster than the satellite and catching up with it on their first transit around the earth. From the drift rates on different L shells, it is possible to deduce the time at which the injection of new particles must have taken place to be consistent with the observations. This time cannot be determined with great precision because of the energy dependence of the drift rate, but it appears to have been 0440 ± 10 minutes. On orbit 2′, Fig. 2-29, the electrons have drifted at least five times around the earth. The distribution in various L shells should be longitudinally quite uniform.

Figure 2-30 shows the results for the same passes as in Fig. 2-29, but for the detector channel E2 measuring electrons above 1.9 Mev. On orbit 1′, in this case, there are two small spikes in electron intensity at about L = 1.85 and 2.0. These were noted previously in connection with Fig. 2-24.

These seem to be the remnants from the first Soviet test six days earlier. There is no question but that much of the flux between L = 2 and 3 is also left over from that earlier test since the slot region is not nearly as deep as it was observed by Telstar I [15] to have been just before the Soviet test series. In orbit 2 on Fig. 2-30, the new electrons of greater than 1.9 Mev have clearly already arrived. In fact, in comparison with orbit 2′, there are more electrons seen earlier than later. This does not seem to be a decay phenomen but rather a decrease in flux associated with the longitudinal dispersion of the originally rather well clumped group of electrons. The drift rates for 1.9 Mev electrons on L = 2 is approximately 20°/min. These particles are probably being observed on their second transit around the earth. If they were in their first transit the injection time would have to have been at about 0500, rather late for the lower energy particles seen in Fig. 2-29. The structure in the electron distribution as observed on orbits 2 and 2′, is quite complex and can in principle at least be related to the motion of the radioactive fragments carried in the expanding plasma of the nuclear explosion.

2.7.2 The Energy Spectrum

In Figs. 2-31, -32, and -33 results from channel E_1, E_2, and E_3 are shown together for the first passes of the satellite to illustrate the L variation in the energy spectrum along the equator. The vertical spacings between these curves on the semilogarithmic plot give the relative spectral hardness of the electron distribution. From Fig. 2-31 for orbit 1′ the residue of the first Soviet explosion is seen at greater than 1.9 and greater than 2.9 Mev, but is not distinguishable as sharp structure at greater than 0.5 Mev. In the outer belt region the detectors indicate fluxes approximately in the ratio 1:.1:.01. In the bottom of the slot at about L = 3 the ratios are 1:.8:.3 a very much harder spectrum. In Fig. 2-32, orbit 2, the peak of the inner belt is seen to have ratios 1:.3:.09. These are in quite good agreement with the equilibrium spectrum of electrons created in fission beta decay.[16] The electrons in the inner belt peak are dominantly those produced by the U.S. Starfish test, and in the peak region they have not decayed very much between July and the end of October as observed by Telstar I.[15] Between L = 1.8 and L $\simeq$ 3 the spectra in Fig. 2-32 are confused by the transient of the newly added electrons in their drift around the world immediately after the second test. Figure 2-33 shows the electron distribution after it had time to disperse uniformly in longitude. Comparing these curves with those of Fig. 2-31 it is clear that electrons of greater

than 0.5 Mev have been added out to as far as L = 3.2 or 3.3 whereas no significant number of the higher energy electrons has been added above L = 3. This indication that the spectrum of added electrons is not everywhere the same is born out by comparisons over the whole L region in which new particles have been added. Even at the maxima at L = 1.85 and 2.15 in Fig. 2-33 the spectra are different and in neither case are they what would be expected from beta decay of fission fragments. Somehow in the injection process the electron energies are reduced, possibly by the mechanism of Fermi deceleration in collision with the walls of the expanding plasma from the explosion as suggested by Hess.[17] Similar phenomena apparently occurred in Starfish as well, and served to produce a much softer spectrum of electrons at large L values than at small. Through such spectral differences and the difference in the detector response characteristics it is possible to account in a qualitative way for the apparent discrepancy between the Telstar I and Injun I measurements of the Starfish electron distribution in space.[18]

Figure 2-34 shows the situation on November 3 following the third Soviet test on November 1. The actual data are presentedin the region between L = 1.5 and 2 to illustrate how narrow and well defined the spike of injection was at about L = 1.78. Unlike the earlier tests, the third test seems to have added no significant numbers of electrons

outside of the single narrow spike. At L = 1.85 and above, the electrons from the second test appear with decreased flux in comparison with Fig. 2-33 because of particle decay over the week since their introduction. The decay of particles in the well defined injection peaks from these two tests appears to occur by loss on the L shell, not by diffusion between L shells. That is, the peaks do not broaden substantially as they decrease in magnitude with time. This is to be expected of Dungey's[19] whistler loss mechanism but perhaps not by a mechanism which produces a general mixing of the different field lines due to broad magnetic disturbances.

2.7.3 B and L Dependence of the Electron Distribution and Decay

In Fig. 2-35 the > 1.9 Mev electron distribution is shown as a function of B, along the L = 1.75 line for several intervals of time. The minimum value of B in the figure corresponds to the equator on this field line. The orbit of November 3 in Fig. 2-34 contributes one of the near equatorial points in Fig. 2-35. The electron flux decreases with increasing B in all cases in the figure. This is equivalent to saying that the distribution of mirror points is peaked at the equator. The triangles in Fig. 2-35 which fall in with the solid circles of the December 14-18 time interval are points measured before the third Soviet test. This region at L = 1.75 has been essentially unaffected by the earlier tests so the triangles

give enough data points to define a "before" particle distribution on this field line rather well. The new particles added on November 1 not only increase the equitorial flux as indicated in Fig. 2-34 but also drastically alter the distribution of electrons in B. The very flat uppermost distribution that is produced, gradually loses its anomalous shape over the next few weeks and reassumes the approximately linear dependence of log φ on log B it had before the test. The whole distribution then decays together. More rapid disappearance of particles at large values of B and the decay of the distribution as a whole at long times are to be expected in processes controlled by diffusion of particle mirror points along field lines with ultimate particle loss in the atmosphere. This is the situation found by Hess[20] and by Walt[21] for lower L values where the atmosphere controls the whole process. It should also be expected in the whistler controlled diffusion of Dungey.[19] The fact that the flux in January in Fig. 2-35 has dropped below the data of the triangles for late October is presumably due to a continuing decay of electrons either from the Starfish test or from the first Soviet test.

Figure 2-36 is analogous to Fig. 2-35 but for L = 2.0. There are now only two data points (triangles) before the test on October 28. One of these corresponds to the outgoing, the other to the incoming pass of the first orbit of Explorer XV.

The equitorial point is that for orbit 1′ of Fig. 2-30. The star marked "earliest point," is for orbit 2, at which time the high energy electrons had not dispersed in longitude. At L = 2.0 the φ, B variation shows a maximum off the equator, an even more anomalous distribution than that on L = 1.75. Such a distribution results from injection of new particles far off the equator. This shape rapidly disappeared and the decay process carries past the triangles of October 28 because of continuing decay of electrons from the first Soviet test. Results for a third field line, L = 2.4, are shown in Fig. 2-37. On this line the injection is much less anomalous and a steady state linear dependence of log φ on log B is rapidly reassumed.

Comparisons of Fig. 2-35, -36 and -37 show two particular features. First, the decay is more rapid on the higher L lines. This is in agreement with the results of Telstar I[22] following Starfish and observed by Telstar I for the Soviet tests as well.[15] Second, the slope of the log φ, log B lines decreases with increasing L. This is qualitatively consistent with the diffusion mechanism of particle loss because the ultimate sink for particles in the atmosphere is more remote for higher L lines. This is shown more extensively in Fig. 3-38, in log φ-log B plots in 15 different L lines for a time approximately November 22. The curves have been separated horizontally to avoid overlapping and the vertical marks identify

specific values of B. The L = 1.8 line stands out above the others because of the injected particles which have not yet decayed. It's slope at this time has however approximately achieved equilibrium.

Detailed considerations of the shapes of the electron distributions produced by the explosions and the consequences of the proposed whistler loss mechanisms which may remove them are in progress. It has recently been found by comparing the >0.5 Mev electron results from Explorer XV with those of the Telstar I electron detector measuring electrons of essentially the same energy just before the Soviet tests, that the first Soviet test injected electrons below L = 1.7 as well as above. There is a definite indication of off equatorial particles in the later distribution. This observation is presently being examined.

2.7.4 Protons

The data from channels E4 at high bias and E1 at low bias have been used to study the distribution of low energy protons. The equatorial variation of their omnidirectional flux is shown in Fig. 2-39, together with results from other measurements of higher energy protons. The 2.1-25 Mev curve, E1 at low bias, is discontinued at L = 1.7 becuase the inner belt electrons, even with their low detection sensitivity begin to dominate the detector. This is evident in Fig. 2-22. The plot shows protons measured in Telstar I[15] and II[23] and in Explorer XV by McIlwain.[24]

In all cases there is a single equatorial maximum, but there is a systematic increase of both maximum proton flux and the radial distance at which the maximum occurs, with a decrease in proton energy. This same trend continues to still lower energies as measured by Davis and Williamson.[5] The distributions over several months of observation were quite stable. They represent thus an essentially steady state between particle source and loss mechanisms. There seems to be no doubt that a major source for the higher energy protons is provided by the decay of albedo neutrons produced by galactic cosmic rays and solar protons reacting with the earth's atmosphere.[25] There also seems to be no doubt that the atmosphere serves as the dominant loss mechanism controlling the very rapid fall off in the proton flux at low altitudes.[26] The source for the low energy protons, however, and the mechanism which controls the upper altitude fall off in the flux are still uncertain. It has been suggested that the protons are lost above the flux maximum by scattering with hydromagnetic waves in the plasma,[27] the waves perhaps arising at the magnetospheric boundary. It is also possible that acceleration mechanisms exist as a result of magnetic field fluctuations associated with boundary variations and that the lower energy protons of Fig. 2-39 were once a part of the low temperature plasma. The importance of unravelling the details of such possibilities is quite evident.

2.7.5 Outer Belt Electrons

The instability of the outer electron belt has been known for some time,[2] but Explorer XV has provided a number of interesting observations concerning the time dependence for electrons of different energies. Figure 2-40 shows the time record of greater than 0.5 Mev electrons at L = 4, in the outer electron belt. The two sets of points divide the data into near equitorial and off equitorial B regions. There is very little B dependence as might be expected by extension of the decrease of the φ, B slope observed in Fig. 2-38 for increasing L. Notice that there is a very rapid electron flux decline shown by the early data. It yields an approximately 5 day time constant. The two B regions change together. Data is missing for about 12 days following day 314, (Section 2.3.1) but when the flux is measured on day 327, it is high again. There is a second decline with a similar but not identical decay time. Then on day 352, there is the start of a very large increase which in two days amounts to more than an order of magnitude. This phenomena occurs at the same time as Snyder[28] has reported observing very large disturbances in the plasma on the Mariner Spacecraft and large fluctuations in magnetic field on the earth. On day 354, the flux reaches a peak and once again begins a rapid decline.

The situation for higher energy electrons is interesting in comparison. Figure 2-41 reproduces the curve drawn in Fig. 2-40 to represent the shape of the 0.5 Mev data. This curve is superimposed on the greater than 1.9 Mev results with a factor of 10 scale change to make comparisons easier. The features of the two sets of data are similar, but note that the 1.9 Mev electrons rise before they decay in the region of day 300 and that the rise at approximately day 327 is visible after the data break whereas for the low energy electrons it was not. In the large rise on about day 352 the 1.9 Mev electrons again lag behind. The 0.5 Mev electrons have started to decline before the high energy electrons have reached their maximum. The increase for the 1.9 Mev electrons is about a factor of 40. These effects are certainly associated with plasma from the sun. Possibly magnetic disturbances initiated in interactions of the solar wind plasma with the earth's field are responsible. It is tempting to believe the observations are showing an acceleration mechanism in operation. It goes on for several days, increasing the energy of very low energy electrons until they are measured by the 0.5 Mev detector and then later by the 1.9 Mev detector. One might also interpret the results as due to a time varying source or particles outside the magnetosphere, the source producing more high energy electrons later. There are difficulties

of course in carrying out injection of such electrons through the magnetospheric boundary and there is no evidence for such energetic electrons from the sun. The interpretation of these effects is presently unknown. It seems almost certain to require a mechanism that involves the plasma from the sun in interaction with the earth's field, a subject which will receive a great deal of attention in presently planned space experiments.

REFERENCES
Section 2

1. Collected Papers on the Artificial Radiation Belt for the July 9, 1962 Nuclear Detonation, J. Geophys. Res. 68 605 (1963).

2. L. A. Frank, J. A. Van Allen, W. A. Whelpley, and J. D. Craven, J. Geophys. Res. 68 1573 (1963).

3. Buck, T. M., Wheatley, G. H., and Rodgers, J. W., Proceedings of the Ninth Scintillation and Semiconductor Counter Symposium, March 1964, to be published IEEE Trans. Nucl. Sci.
   See also Brown, Buck, et al, B.S.T.J. 42 899 (1963).

4. The Cosmic Ray Logic Box is so designated because it provided logical functions in Explorer XII and XIV for cosmic ray experiments by F. B. McDonald, GSFC.

5. Davis, L. R. and Williamson, J. M., Space Science Review, Vol. III, edited by W. Priester, Interscience Publishers Inc., New York 1963.

6. T. M. Buck, private communication. These effects are closely related to surface radiation effects on other semiconductor devices, see Ref. 8.

7. W. L. Brown, T. M. Buck, L. V. Medford, E. W. Thomas, H. K. Gummel, G. L. Miller, and F. M. Smits, B.S.T.J. 42 899, (1963).

8. D. S. Peck, R. R. Blair, W. L. Brown, and F. M. Smits, B.S.T.J. 42 95 (1963).

9. These calibrations were carried out with a Van de Graaff at the High Voltage Research Laboratory of M.I.T. and with the valuable assistance of K. A. Wright.

10. These calibrations were made with the kind cooperation of Professor R. Scheer of Princeton University and with the assistance of A. Emann.

11. McIlwain, C. E., J. Geophys. Res. 66 3681 (1961).

12. R. W. Hamming, Numerical Method for Scientists and Engineers, Chapter 24, McGraw Hill Book Co., Inc. New York (1962).

13. T. A. Farley and N. L. Sanders, J. Geophys. Res. 67 2159 (1962).

14. Welsh, J. A. Jr., and Whitaker, W. A., J. Geophys. Res. 909 (1959).

15. Brown, W. L., Gabbe, J. D., and Rosenzweig, W., B.S.T.J. 42 1505 (1963).

16. R. E. Carter, F. Reines, J. V. Wagner and M. E. Wyman, Phys. Rev. 113 280 (1959).

17. W. N. Hess, Bulletin of the American Geophysical Union, p. 76, April 1963.

18. Brown, W. L., Hess, W. N., and Van Allen, J. A., J. Geophys. Res. 68 605 (1963).

19. Dungey, J. W., Planet Space Sci. 11 591 (1963).

20. Welch, J. A. Jr., Kaufman, R. L., and Hess, W. N., J. Geophys. Res. 68 685 (1963).

21. Walt, M., G. E. Crane, and W. M. MacDonald, Trans. Am. Geophys. Union 44, 78 (1963).

22. W. L. Brown and J. D. Gabbe, J. Geophys. Res. 68 607 (1963).

23. The Telstar II Experiment, Report in press.

24. McIlwain, C. E., Science 142 3590 (1963).

25. Singer, S. F., Space Research, Proceedings of the First International Space Science Symposium, ed. H. K. Kaleman-Bijl, North Holland, Amsterdam 1960.

Hess, W. N., Phys. Rev. Letters 3 11 (1959), ibid 3 145 (1959).

26. Ray, E. C., J. Geophys. Res. 65 1125 (1960).

27. Dragt, A. J., J. Geophys. Res. 66 1641 (1961).

28. Snyder, C. W., Neugebauer, M. and Rao, V. R., J. Geophys. Res. 68 6361 (1963).

FIGURE CAPTIONS

Section 2

Fig. 2-1 The cross section of a silicon p-n junction particle detector used in the Explorer XV experiments.

Fig. 2-2 A block diagram of the circuitry.

Fig. 2-3 The completely assembled BTL detector box.

Fig. 2-4 The BTL experiment as seen mounted on the assembled spacecraft.

Fig. 2-5 Back view of the main BTL detector box with the cover removed before final foaming.

Fig. 2-6 An exploded view of the detector mounting blocks.

Fig. 2-7 Assembly drawing of the block-of-four-detector mount.

Fig. 2-8 Assembly drawing of the omnidirectional detector block.

Fig. 2-9 The detector cartridge subassembly.

Fig. 2-10 Circuit schematics of the circuits in the main detector box.

A. The Preamplifier

B. The Linear Amplifier

C. The Discriminator

Fig. 2-11 Schematics of the bias box circuits.

Fig. 2-12 Completed mother board assemblies for a channel with a single discriminator and with two discriminators.

Fig. 2-13 The bias supply disassembled.

Fig. 2-14 Temperature dependence of the discrimination level.

Fig. 2-15 The dependence of the discrimination level on the supply voltage.

Fig. 2-16 The paired pulse resolution of Channel E3 and E4.

Fig. 2-17 The directional sensitivity of Detector A.

Fig. 2-18 The energy dependence of the geometrical factor of Detector A for electrons.

Fig. 2-19 The directional sensitivity of Detector B.

Fig. 2-20 The energy dependence of the geometrical factor of Detector B for electrons.

Fig. 2-21 The calculated response of Detector A for protons at high and low bias.

Fig. 2-22 Data for Channel E1 versus L for the first outgoing orbit of Explorer XV, beginning at 2341 on October 27.

Fig. 2-23 Data for Channel E1 versus L for January 3, 1963.

Fig. 2-24 Data for Channel E2 versus L for the first outgoing pass of the satellite.

Fig. 2-25 The data from Channel E4 for the first outgoing pass of the satellite.

Fig. 2-26 The data of Fig. 2-22 including the machine interpolated values. These are shown at small plus signs at high bias and small minus signs as low bias.

Fig. 2-27 The geometry of the detector, the spin axis of the satellite, and the local magnetic field.

Fig. 2-28 Gamma correction factors for a detector with 20° full angle.

Fig. 2-29 Results for Channel E1, electrons > 0.5 Mev, for several orbits on October 28, 1962.

Fig. 2-30 Results for Channel E2, electrons > 1.9 Mev, for several orbits on October 28, 1962.

Fig. 2-31 The results of Channels E1, E2, and E3 for orbit 1′.

Fig. 2-32 The results of Channels E1, E2, and E3 for orbit 2.

Fig. 2-33 The results of Channels E1, E2, and E3 for orbit 2′.

Fig. 2-34 The results for Channels E1, E2, and E3 for November 3, 1962.

Fig. 2-35 Log φ-Log B plots of the electrons > 1.9 Mev at L = 1.75 for several intervals of time.

Fig. 2-36 Log φ-Log B plots of electrons > 1.9 Mev on L = 2.0 for several intervals of time.

Fig. 2-37 Log φ-Log B plots of electrons > 1.9 Mev on L = 2.4 for several intervals of time.

Fig. 2-38 Log φ-Log B distributions of electrons > 1.9 Mev for 15 different L lines.

Fig. 2-39 The equatorial omnidirectional flux of protons from E1 low and E4 high compared with higher energy proton measurements.

Fig. 2-40 The fluctuations in the > .5 Mev electrons in the outer electron belt L = 4.0 from October 28, 1962 to January 4, 1963.

Fig. 2-41 The fluctuations in the > 1.9 Mev electrons in the outer electron belt at L = 4.0 for the same time period as Fig. 2-40. The totally dashed curve in the figure is reproduced from Fig. 2-40 with the change in vertical scale of a factor of 10.

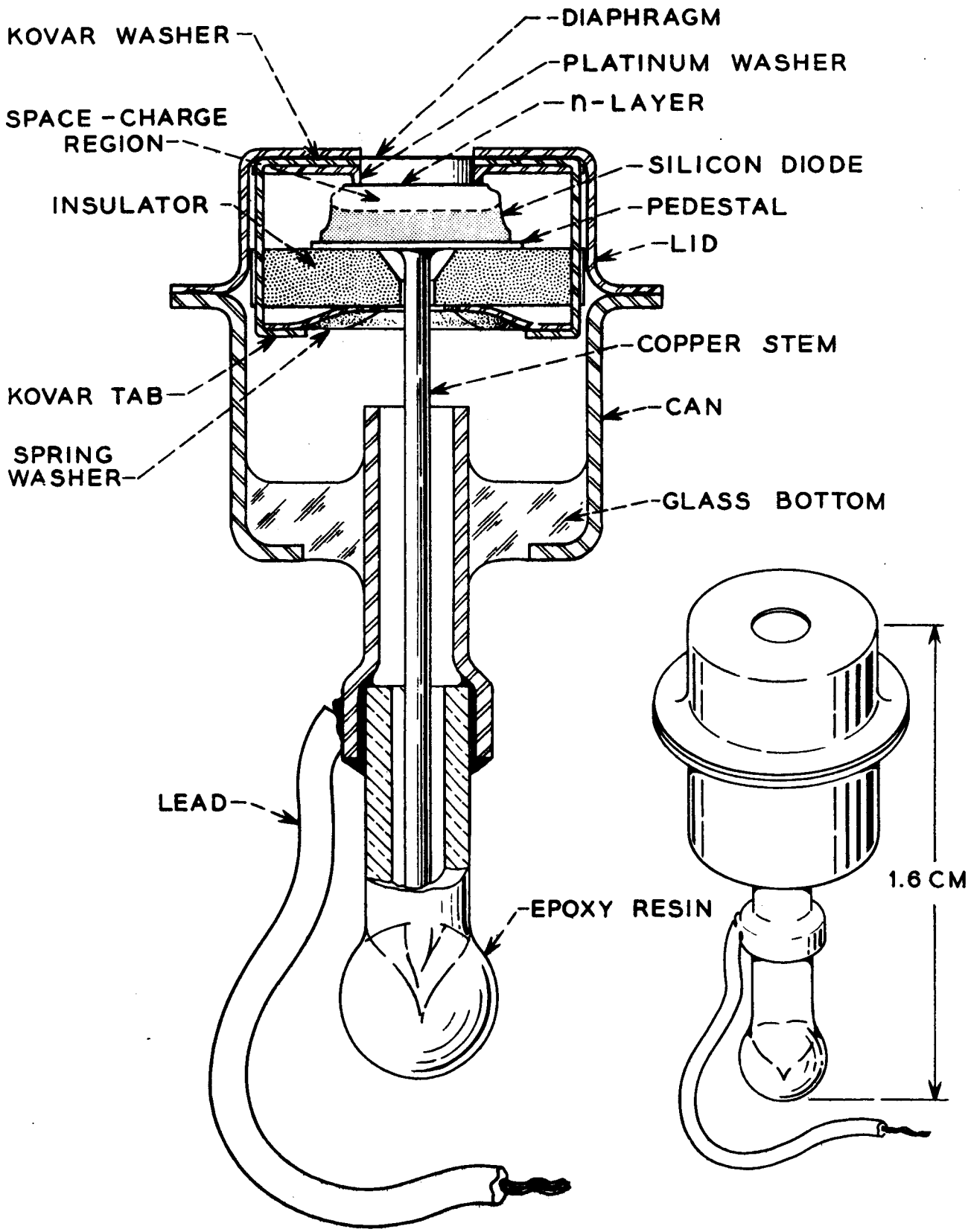
KOVAR WASHER
DIAPHRAGM
PLATINUM WASHER
n-LAYER
SPACE-CHARGE REGION
SILICON DIODE
INSULATOR
PEDESTAL
LID
COPPER STEM
KOVAR TAB
CAN
SPRING WASHER
GLASS BOTTOM
LEAD
EPOXY RESIN
1.6 CM

Fig. 2-1

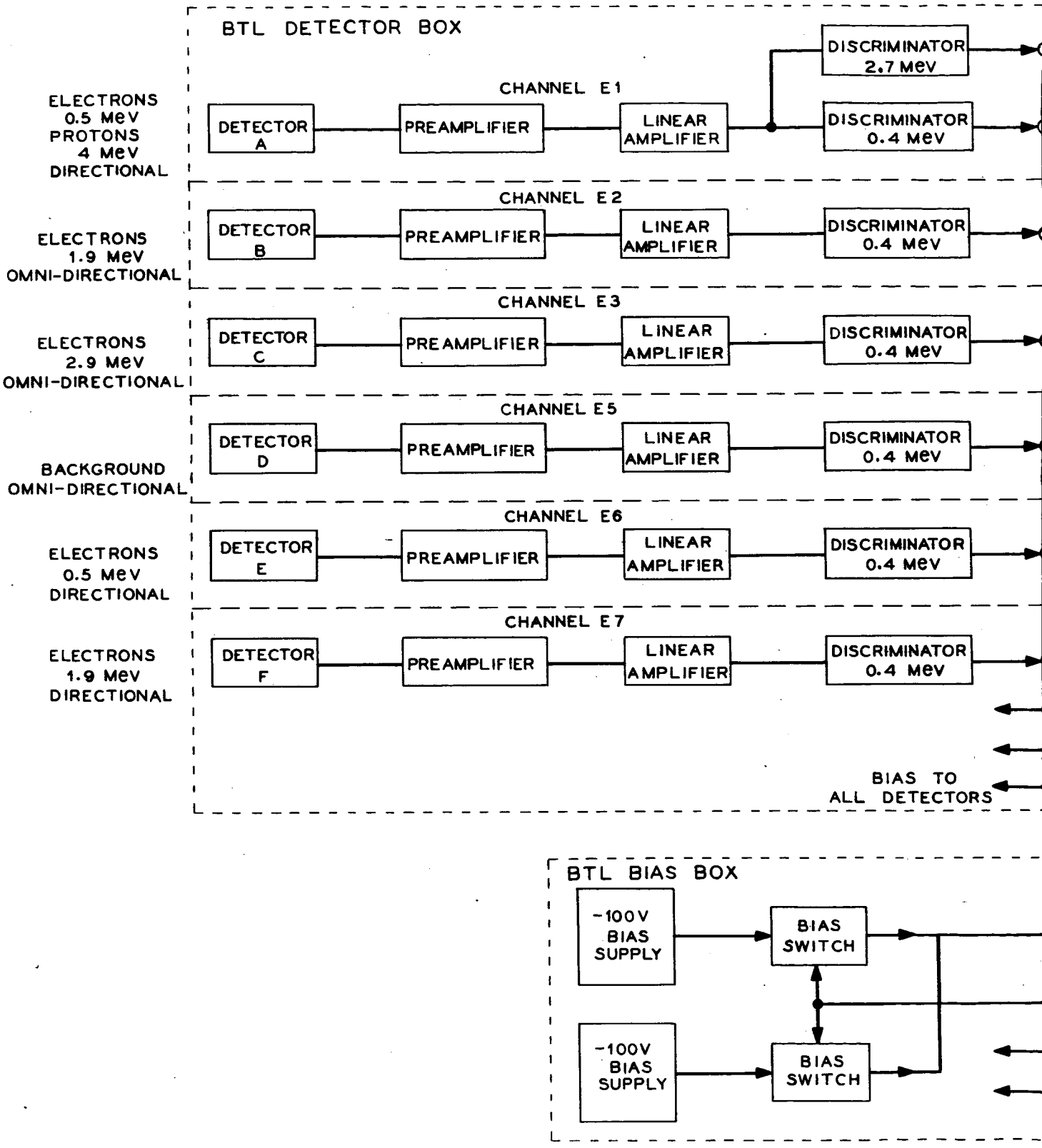
BTL DETECTOR BOX
CHANNEL E1
ELECTRONS 0.5 MeV PROTONS 4 MeV DIRECTIONAL
DETECTOR A
PREAMPLIFIER
LINEAR AMPLIFIER
DISCRIMINATOR 2.7 MeV
DISCRIMINATOR 0.4 MeV
CHANNEL E2
ELECTRONS 1.9 MeV OMNI-DIRECTIONAL
DETECTOR B
PREAMPLIFIER
LINEAR AMPLIFIER
DISCRIMINATOR 0.4 MeV
CHANNEL E3
ELECTRONS 2.9 MeV OMNI-DIRECTIONAL
DETECTOR C
PREAMPLIFIER
LINEAR AMPLIFIER
DISCRIMINATOR 0.4 MeV
CHANNEL E5
BACKGROUND OMNI-DIRECTIONAL
DETECTOR D
PREAMPLIFIER
LINEAR AMPLIFIER
DISCRIMINATOR 0.4 MeV
CHANNEL E6
ELECTRONS 0.5 MeV DIRECTIONAL
DETECTOR E
PREAMPLIFIER
LINEAR AMPLIFIER
DISCRIMINATOR 0.4 MeV
CHANNEL E7
ELECTRONS 1.9 MeV DIRECTIONAL
DETECTOR F
PREAMPLIFIER
LINEAR AMPLIFIER
DISCRIMINATOR 0.4 MeV
BIAS TO ALL DETECTORS
BTL BIAS BOX
-100V BIAS SUPPLY
BIAS SWITCH
-100V BIAS SUPPLY
BIAS SWITCH

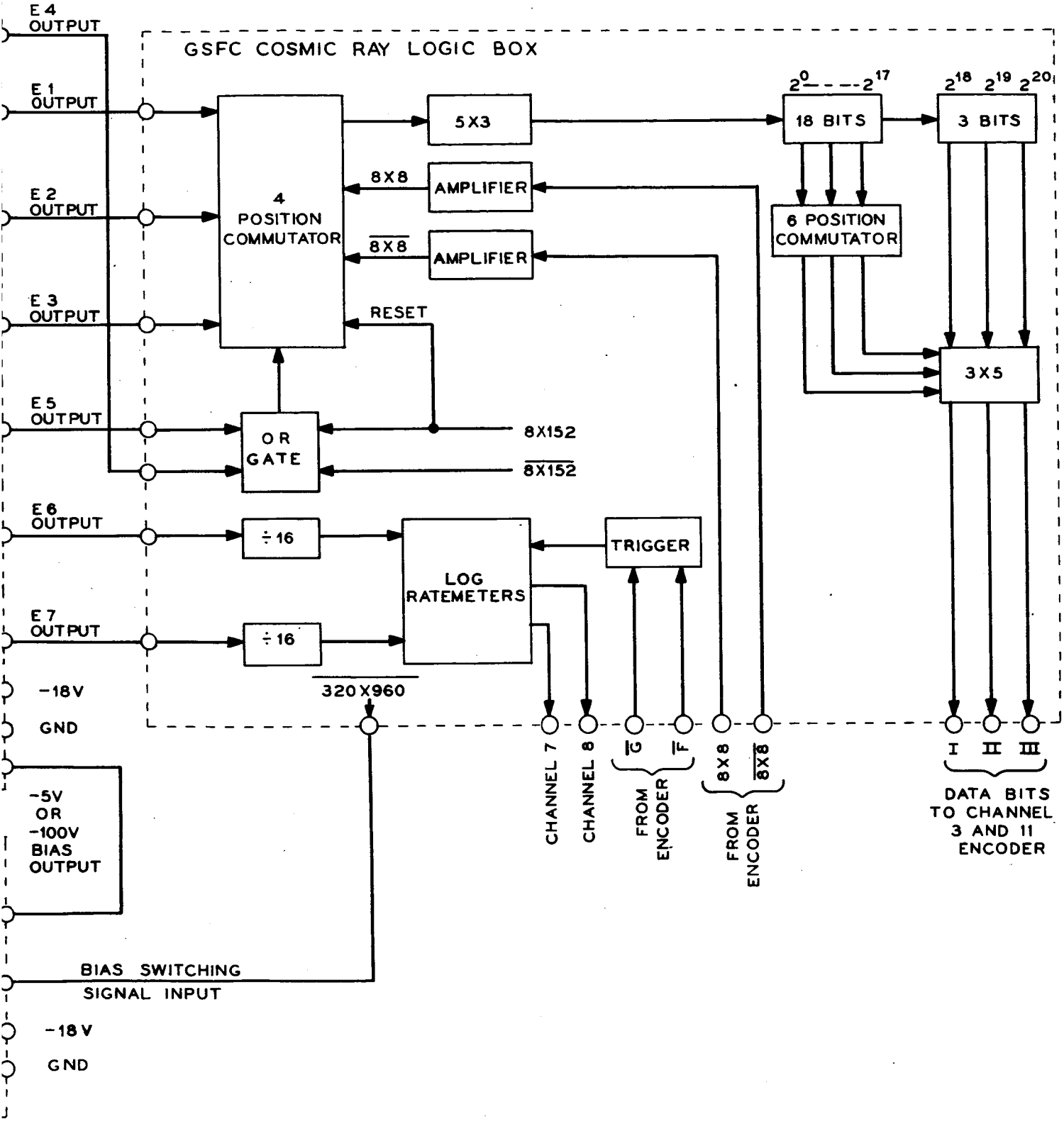
GSFC COSMIC RAY LOGIC BOX
E 4 OUTPUT
E 1 OUTPUT
E 2 OUTPUT
E 3 OUTPUT
E 5 OUTPUT
E 6 OUTPUT
E 7 OUTPUT
-18V
GND
-5V OR -100V BIAS OUTPUT
BIAS SWITCHING SIGNAL INPUT
-18 V
GND
4 POSITION COMMUTATOR
5X3
8X8
AMPLIFIER
$\overline{8X8}$
AMPLIFIER
RESET
OR GATE
8X152
$\overline{8X152}$
÷16
÷16
LOG RATEMETERS
TRIGGER
$\overline{320X960}$
2^0 - - - 2^{17}
18 BITS
2^{18} 2^{19} 2^{20}
3 BITS
6 POSITION COMMUTATOR
3X5
CHANNEL 7
CHANNEL 8
$\overline{G}$ $\overline{F}$
FROM ENCODER
8X8 $\overline{8X8}$
FROM ENCODER
I II III
DATA BITS TO CHANNEL 3 AND 11 ENCODER

Fig. 2 2

PH NO.
B63-3767-MH
BELL TELEPHONE LABORATORIES
CASE NO.
38140-13

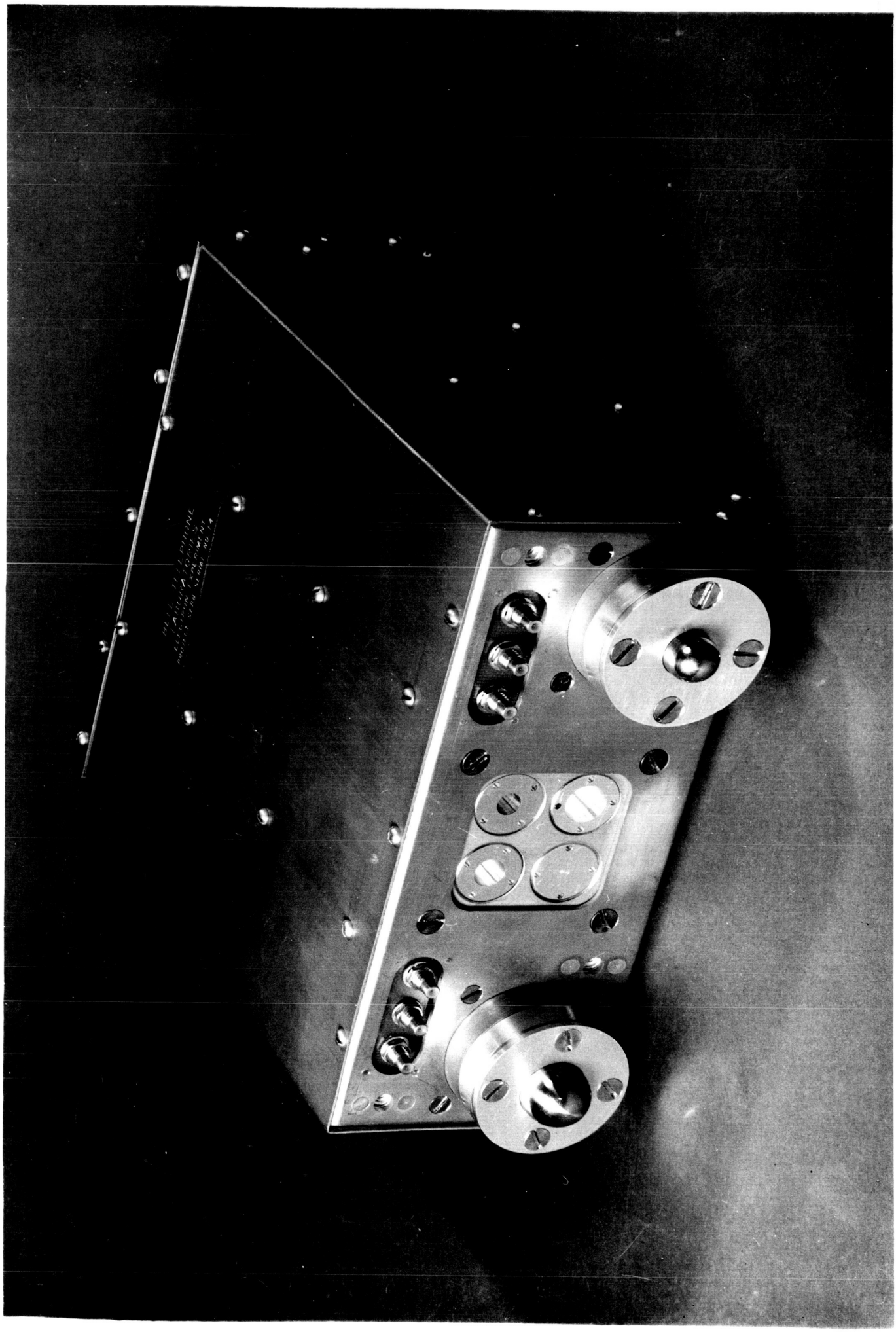

Fig. 2-3

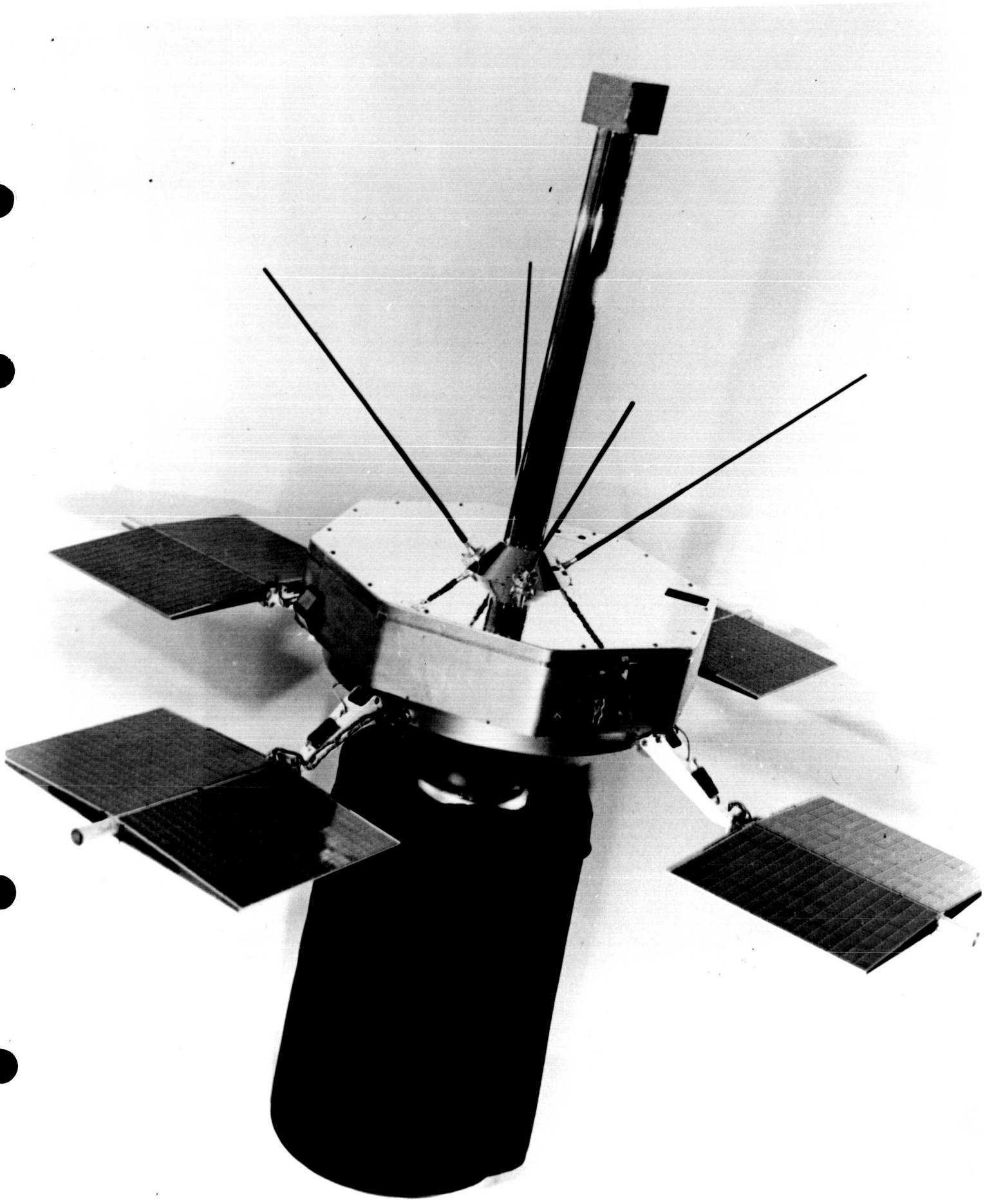

Fig. 2-4

CASE NO.
38140-13

BELL TELEPHONE LABORATORIES

PHOTO NO.
B63-3765-MH

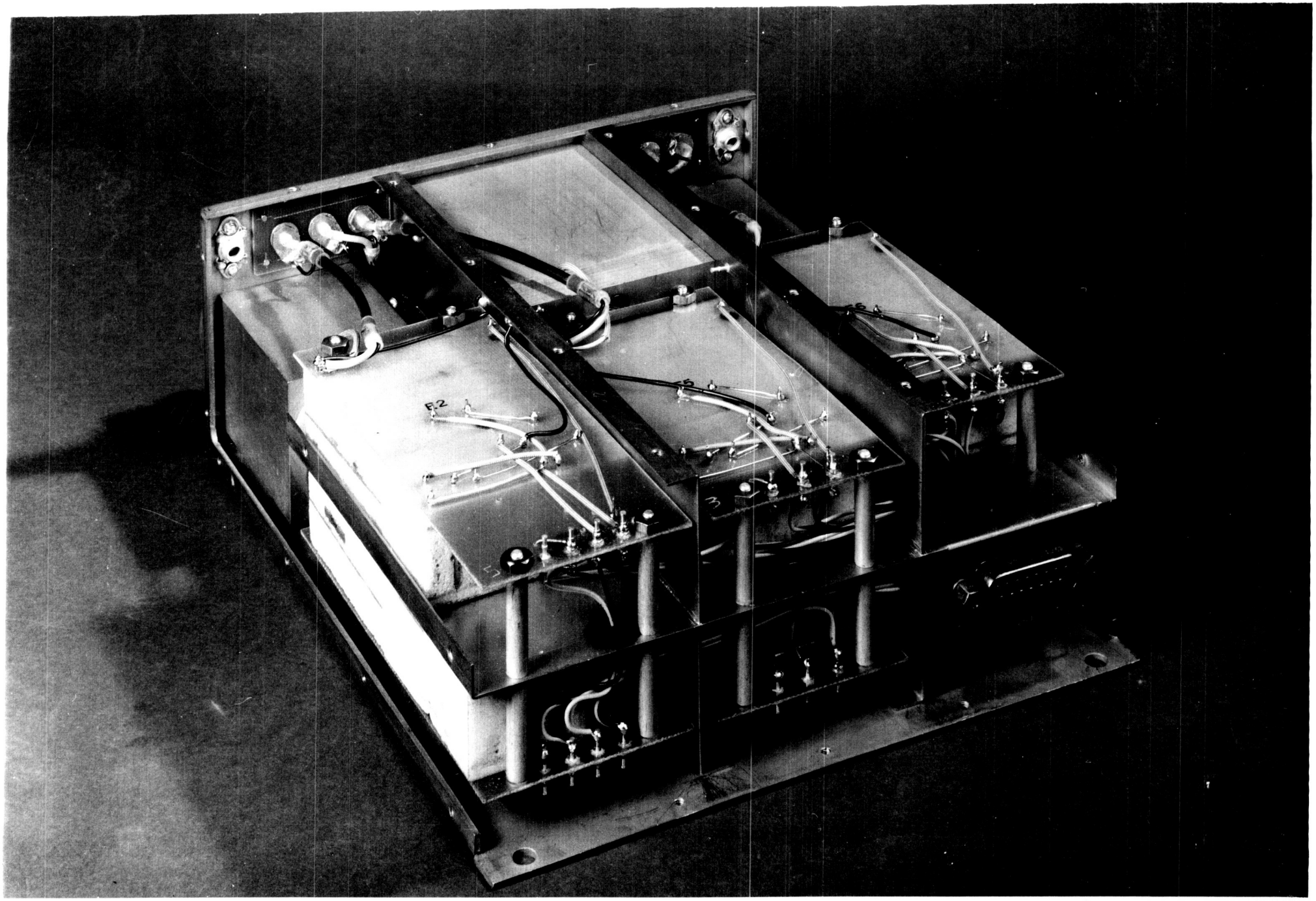

Fig. 2-5

PHOTO NO. 362-102281-MH
BELL TELEPHONE LABORATORIES
CASE NO. 39090-2

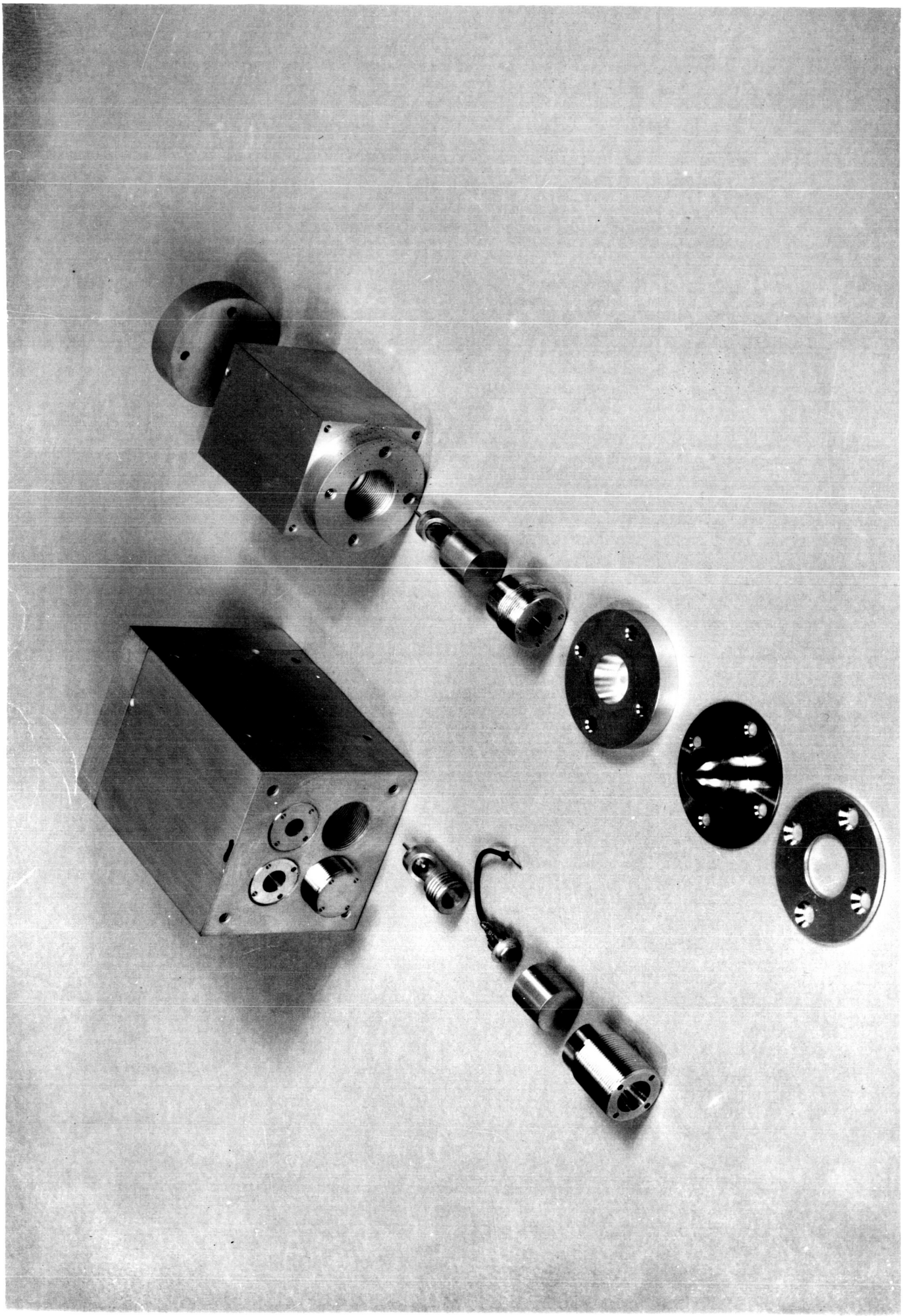

Fig. 2-6

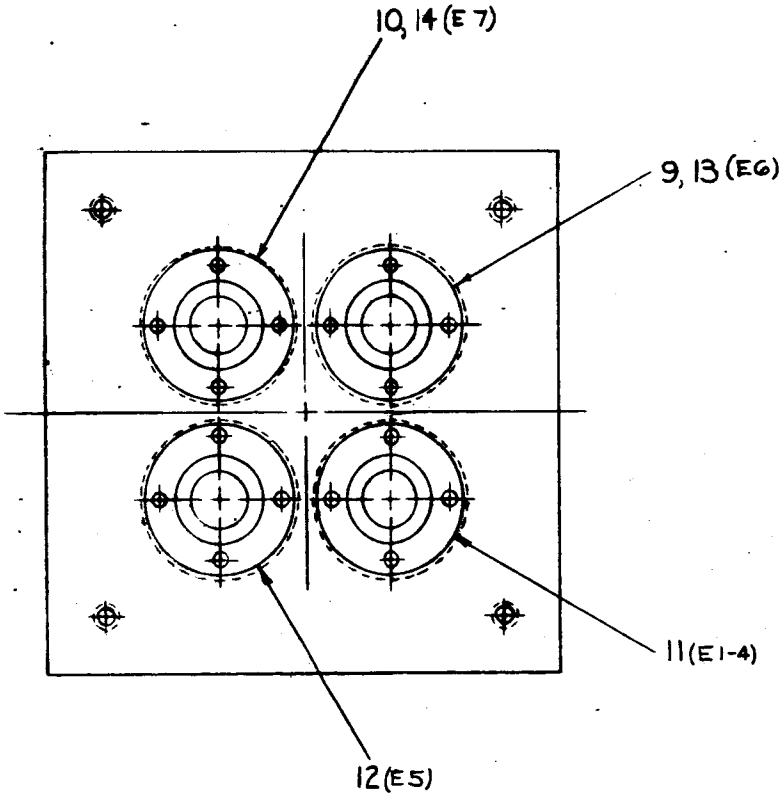

PRINTED IN U.S.A.
E-7944-C-3 (5-61)

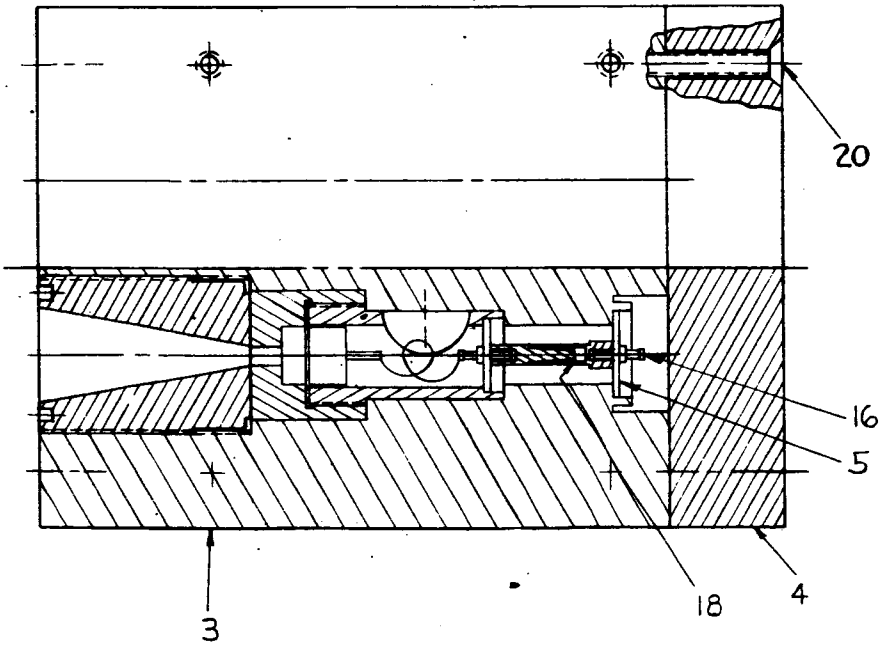

Fig. 2-7

BOOK FOLD 5 | BOOK FOLD 6

NOTES:

1. CRIMP ITEM 3 TO RETAIN WASHER, ITEM 5.

A-

DRT. W.T. BROWN
CHKD. E.A. HOPE
ISSUE 1 10-15-62

REQ	IDENTIFICATION NO.	DESCRIPTION	REF DESIG	NOTE	ITEM
4		SCR, FHM, .112-40 x .68 LG			20
4		FEMALE PIN			18
4		TERMINAL			16
1	B-611707-2	SENSOR ASSEMBLY			14
3	B-611707-1	SENSOR ASSEMBLY			13
1	B-605248-4	PLUG (E5)			12
1	B-605248-3	PLUG (E1-4)			11
1	B-605248-2	PLUG (E7)			10
1	B-605248-1	PLUG (E6)			9
4	B-605234	BLOCK WASHER			5
1	B-605232	BACK PLATE			4
1	B-605230	BLOCK DIRECTIONAL DETECTOR			3

STOCK LIST

SUPPLEMENTARY DRAWINGS

SIGNIFICANCE OF SYMBOLS AND ITEM NUMBER SUFFIXES

S—PARTIAL ASSEMBLIES ON OTHER DRAWINGS WITH STOCK LISTS
D—PARTS SHIPPED LOOSE
} ITEMS NOT SPECIFIED AS "S" OR "D" PARTS IN ITEM COLUMN ARE INDIVIDUAL ("A") PARTS

WHERE ITEMS HAVE REFERENCE DESIGNATIONS, THEY MAY BE USED IN LIEU OF ITEM NUMBERS ON THE DELINEATION.

✓ IN "REQ" COLUMN OF STOCK LIST—QUANTITY AS REQUIRED
✓ IN "REQ" COLUMN OF SUPPLEMENTARY DWG LIST DRAWING REQUIRED
● DENOTES MANUFACTURE DISCONTINUED
■ DENOTES MANUFACTURE LIMITED
AB—DENOTES APPARATUS BOOK DRAWINGS

UNLESS OTHERWISE SPECIFIED, ALL DIMENSIONS ARE IN INCHES. NONLIMITED DIMENSIONS OTHER THAN SIZE OF RAW MATERIAL SHALL BE HELD AS FOLLOWS WHEN EXPRESSED:

TO 2 DECIMAL PLACES ± AS ANGLES ±
TO 3 DECIMAL PLACES ±

FOR GENERAL INFORMATION ON SYMBOLS AND NOTES REFER TO MANUFACTURING STANDARD 16.003, PART 2, SECTION 227.

DWG SIZE 4 S

USED ON | DWG

DIRECTIONAL DETECTOR ASSEMBLY

S-3B

SCALE 2/1

WESTERN ELECTRIC CO. INC
ENGINEER OF MANUFACTURE

BELL TELEPHONE LABORATORIES INCORPORATED

B-605243
A-

ISSUE 1 B-605243

BOOK FOLD 2 | BOOK FOLD 1 | LOOSE PRINT FOLD 3

A-
25
PRINT FOLD 1
BOOK FOLD TRIM LINE
BOOK FOLD TRIM LINE
16

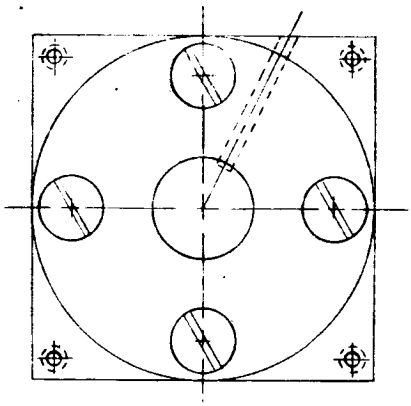

PRINTED IN U.S.A.
E-73444-0-3 (9-61)

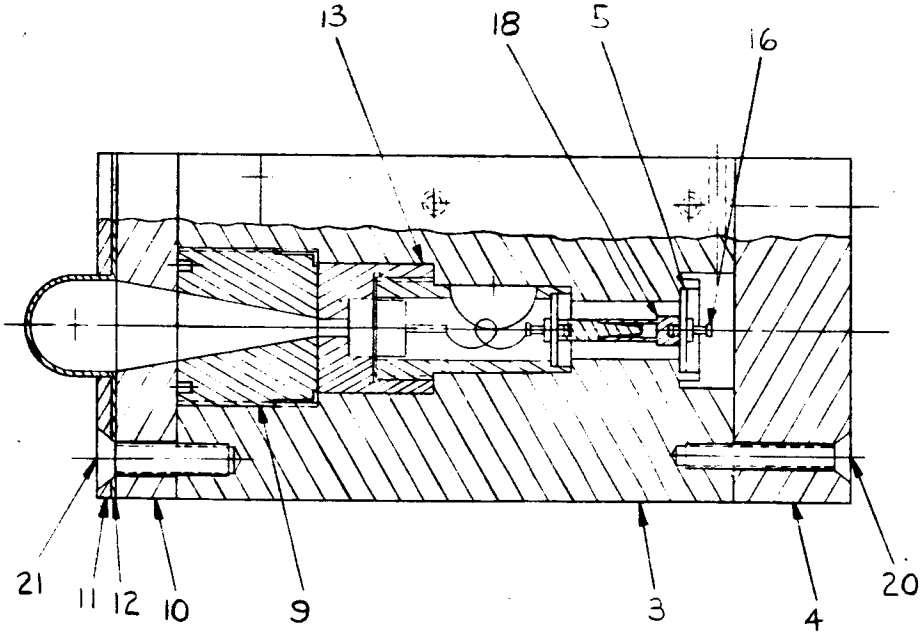

Fig. 2-8

BOOK FOLD 5

BLOCK FOLD 6

NOTES:

1. CRIMP ITEM 3 TO RETAIN WASHER (ITEM 5)

REQ	IDENTIFICATION NO.	DESCRIPTION	REF DESIG	NOTE	ITEM
4		SCR., FHM, 138-32 × .50 LG			21
3		SCR., FHM, .112-40 × .68 LG			20
1		FEMALE PIN			18
1		TERMINAL			16
1	B-611707-1	SENSOR ASSEMBLY			13
1	B-605247	SCATTERING DOME			12
1	B-605241	RETAINER RING			11
1	B-605239	FRONT PLATE			10
1	B-605238	PLUG (E4)			9
1	B-605234	BLOCK WASHER			5
1	B-605231	BACK PLATE			4
1	B-605229-2	BLOCK OMNI-DETECTOR			3

STOCK LIST

SUPPLEMENTARY DRAWINGS

SIGNIFICANCE OF SYMBOLS AND ITEM NUMBER SUFFIXES

B—PARTIAL ASSEMBLIES ON OTHER DRAWINGS WITH STOCK LISTS
D PARTS SHIPPED LOOSE
ITEMS NOT SPECIFIED AS "B" OR "D" PARTS IN ITEM COLUMN ARE INDIVIDUAL ("A") PARTS

WHERE ITEMS HAVE REFERENCE DESIGNATIONS, THEY MAY BE USED IN LIEU OF ITEM NUMBERS ON THE DELINEATION.

✓ IN "REQ" COLUMN OF STOCK LIST—QUANTITY AS REQUIRED
✓ IN "REQ" COLUMN OF SUPPLEMENTARY DWG LIST DRAWING REQUIRED
● DENOTES MANUFACTURE DISCONTINUED
■ DENOTES MANUFACTURE LIMITED
AB DENOTES APPARATUS BOOK DRAWINGS

UNLESS OTHERWISE SPECIFIED, ALL DIMENSIONS ARE IN INCHES. NONLIMITED DIMENSIONS OTHER THAN SIZE OF RAW MATERIAL SHALL BE HELD AS FOLLOWS WHEN EXPRESSED:

TO 2 DECIMAL PLACES ± AS ANGLES ±
TO 3 DECIMAL PLACES ±

FOR GENERAL INFORMATION ON SYMBOLS AND NOTES REFER TO MANUFACTURING STANDARD 16.00[illegible] PART [illegible] SECTION 22[illegible]

DWG SIZE 4 S

A-

ENGR W.L. BROWN
DRAWN C. SWOPE
ISSUE 1 10-11-62

BOOK FOLD 2

BOOK FOLD 1

LOOSE PRINT FOLD 3

ISSUE 1 B-605245

USED ON | DWG

DETECTOR ASSEMBLY, E2

S-3B

SCALE 2/1

WESTERN ELECTRIC CO. INC
ENGINEER OF MANUFACTURE

BELL TELEPHONE LABORATORIES
INCORPORATED

B-605245
A-

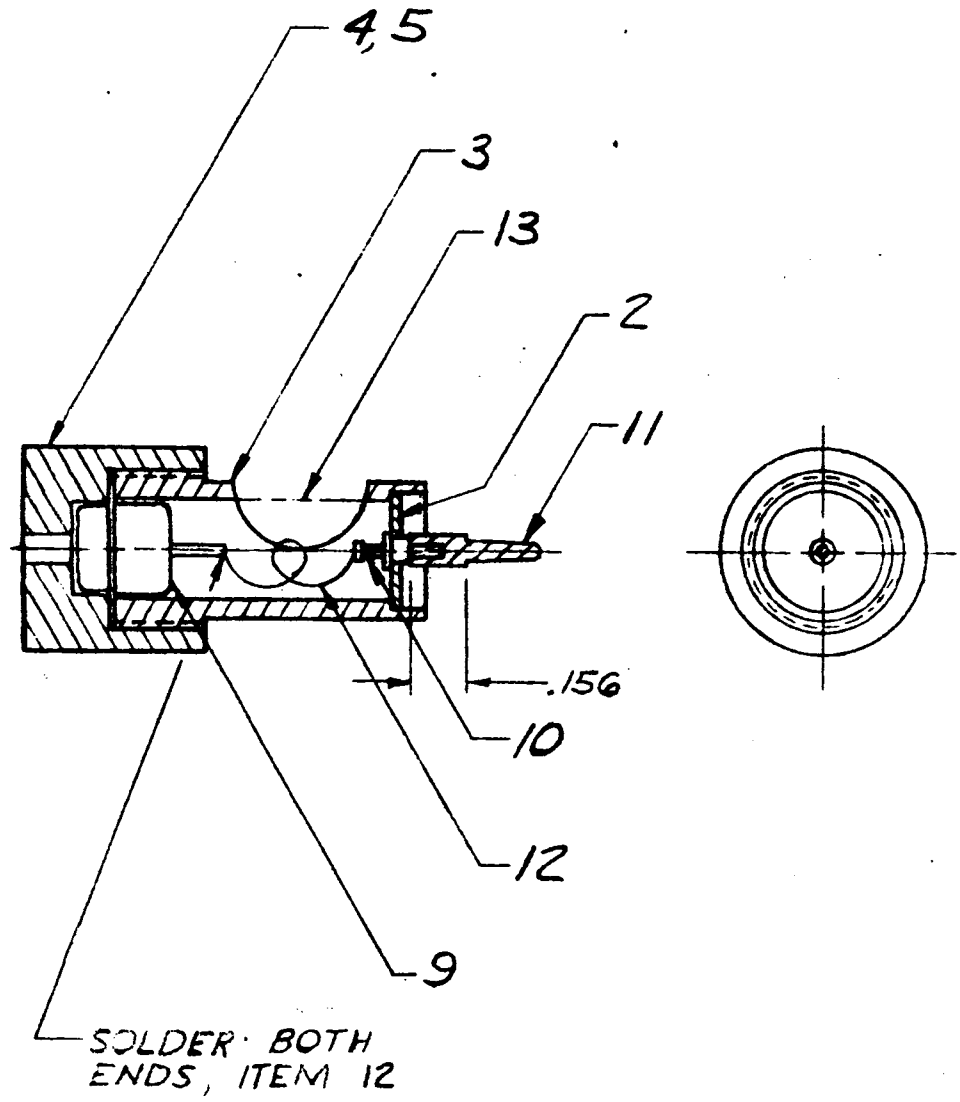

Fig. 2-9

15 5/8
10 3/4
No. 170 K & E CO. 56279
PRINTED IN U.S.A.
E-7344-B-3P (12-61)

RETAIN

		25
		24
		23
		22
		21
		20
		19
		18
		17
		16
		15
		14
	/	13
	/	12
	/	11
	/	10
	/	9
		8
		7
		6
		5
		4
		3
		2
		1
IF DESIG	NOTE	ITEM

ES

DIMENSIONS
RESSED:

DWG SIZE
2S

ENGR W.L. BROWN
DRAWN C. SWOPE
6-23-64 ISSUE 1

USED ON	DWG
	B-605245
	B-605244
	B-605243

SENSOR
ASSEMBLY

SCALE 2/1

BELL TELEPHONE
LABORATORIES
INCORPORATED

B-611707

LOOSE PRINT FOLD 1 | BOOK FOLD 1 | BOOK FOLD 2

LOL119-8 | ISSUE 1

NOTES:
1. SUPPLIED BY ENGINEER
2. CRIMP END OF BARREL (ITEM 3) TO WASHER (ITEM 2) AT ASSEMBLY

REQ	REQ	IDENTIFICATION NO.	DESCRIPTION	R
✓	✓		MYLAR FILM	
✓	✓		WIRE, COPPER, BRAIDED	
1	1		MALE PIN	
1	1		TERMINAL	
1	1		SENSOR	
1		B-611708	CAP	
	1	B-605236	CAP	
1	1	B-605235	BARREL	
1	1	B-605233	INSERT WASHER	

STOCK LIST

SUPPLEMENTARY DRAWINGS

SIGNIFICANCE OF SYMBOLS AND ITEM NUMBER SUFFIX

B—PARTIAL ASSEMBLIES ON OTHER DRAWINGS WITH STOCK LISTS
D—PARTS SHIPPED LOOSE
} ITEMS NOT SPECIFIED AS "B" OR "D" PARTS IN ITEM COLUMN ARE INDIVIDUAL ("A") PARTS.

WHERE ITEMS HAVE REFERENCE DESIGNATIONS, THEY MAY BE USED IN LIEU OF ITEM NUMBERS ON THE DELINEATION.

✓ IN "REQ" COLUMN OF STOCK LIST—QUANTITY AS REQUIRED
✓ IN "REQ" COLUMN OF SUPPLEMENTARY DWG LIST—DRAWING REQUIRED
● DENOTES MANUFACTURE DISCONTINUED
■ DENOTES MANUFACTURE LIMITED
AB—DENOTES APPARATUS BOOK DRAWINGS

UNLESS OTHERWISE SPECIFIED, ALL DIMENSIONS ARE IN INCHES. NONLIMITED OTHER THAN SIZE OF RAW MATERIAL SHALL BE HELD AS FOLLOWS WHEN EXP

TO 2 DECIMAL PLACES ± AS ANGLES ±

TO 3 DECIMAL PLACES ± .005

B-611707-2

B-611707-1

FIG. 2 A
PREAMPLIFIER
6 REQD

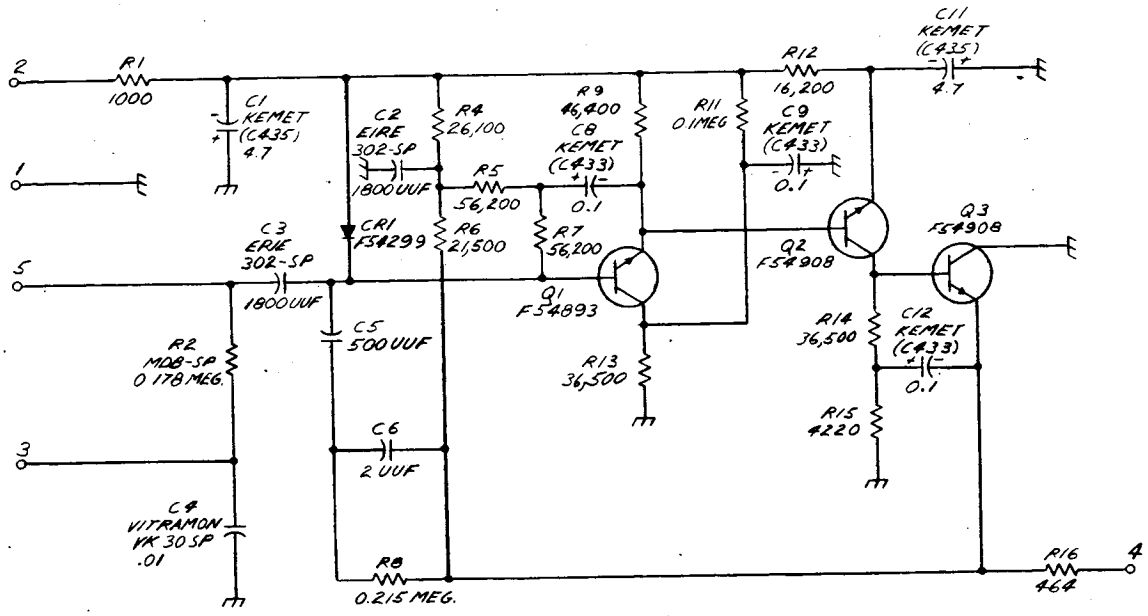

C
FIG 4
DISCRIMINATOR
7 REQD

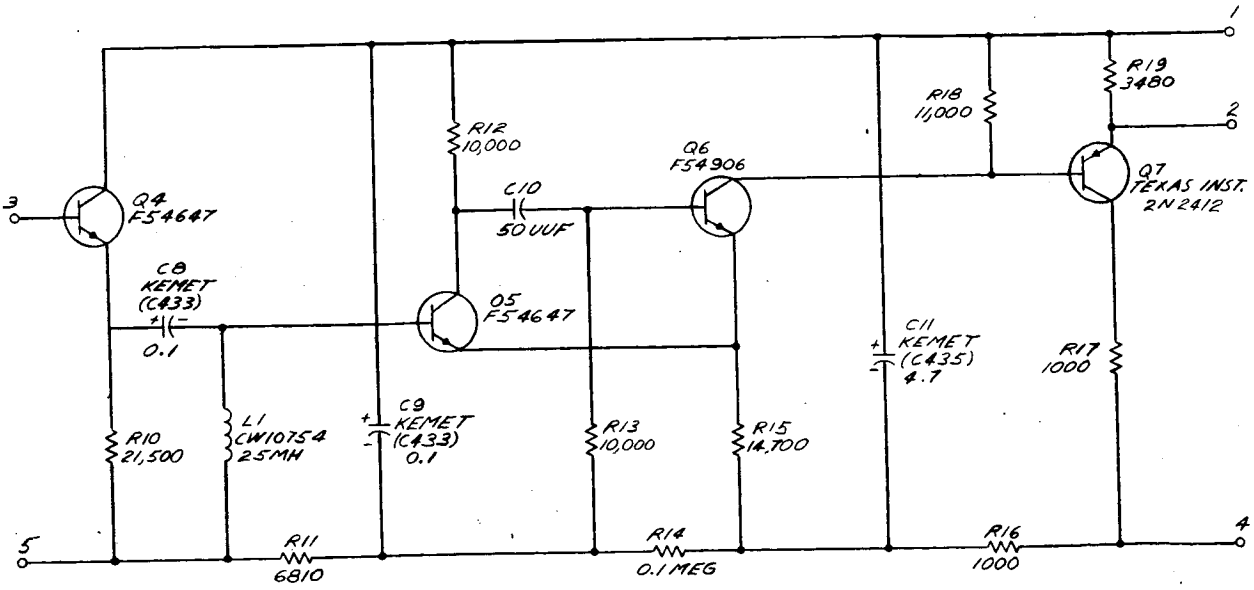

Fig. 2-10

B-891431

B

~~FIG. 3~~

LINEAR AMPLIFIER
5 REQD GRP 1
1 REQD GRP 2

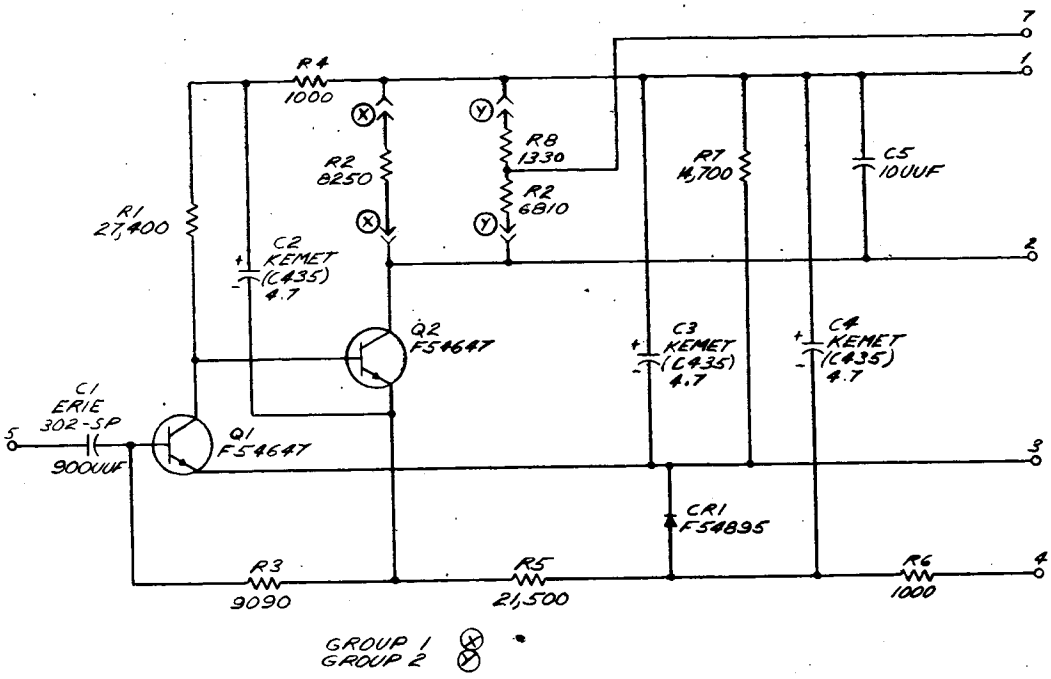

DRAWING ISSUE

RADIATION DETECTOR
CIRCUIT
(SERB EXPERIMENT)

BELL TELEPHONE LABORATORIES
INCORPORATED

DWG SIZE 6S

B-89143J
SHEET 3

PRINTED IN U.S.A.

INFORMATION NOTES:

30% UNLESS OTHERWISE SPECIFIED:

ALL RESISTANCE VALUES ARE OHMS
ALL CAPACITANCE VALUES ARE IN MICROFARADS
ALL RESISTORS ARE ALLEN BRADLEY EB-SP
ALL DIODES ARE FS4299.

FIG.
BIAS SUP

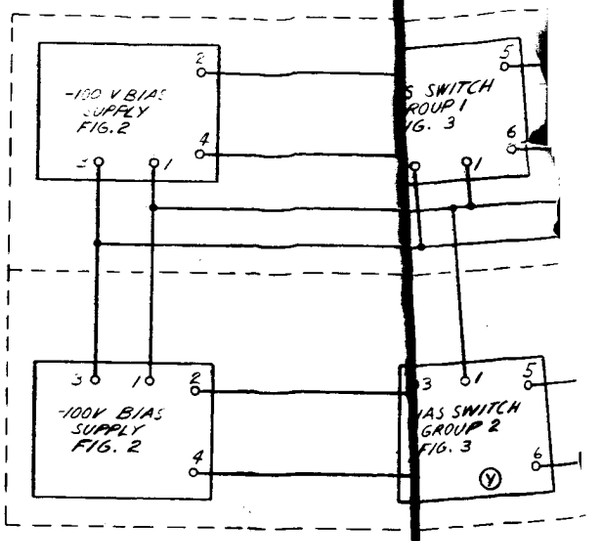

FIG. 2
-100 V BIAS SUPPLY
2 REQD

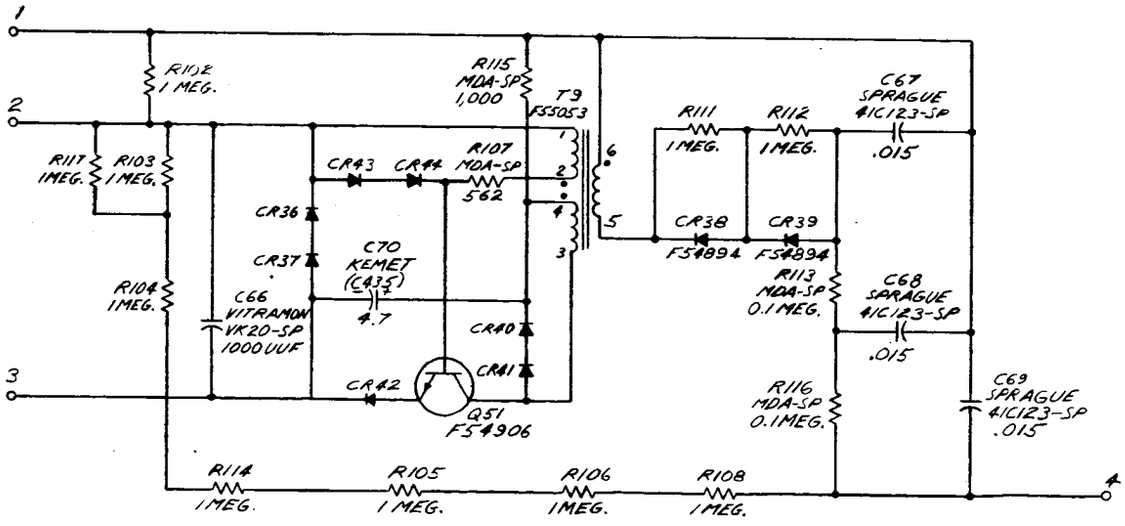

B-891434

Fig. 2-11

B-89143

DWG ISSUE	EE OR CD ISSUE	DATE ISSUED	DRAWN	APPD.
1	–	[illegible]	LES	[illegible]

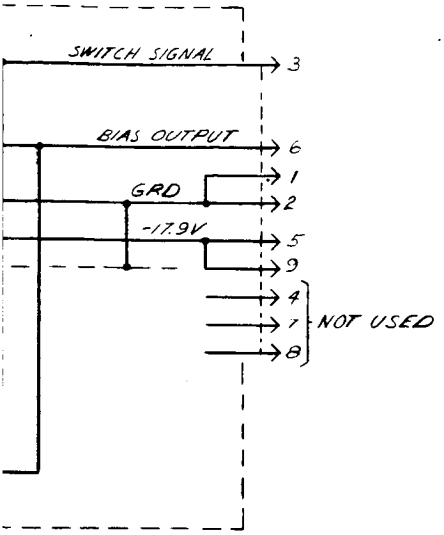

FIG. 3
BIAS SWITCH
GROUP 1 1REQD
GROUP 2 1REQD

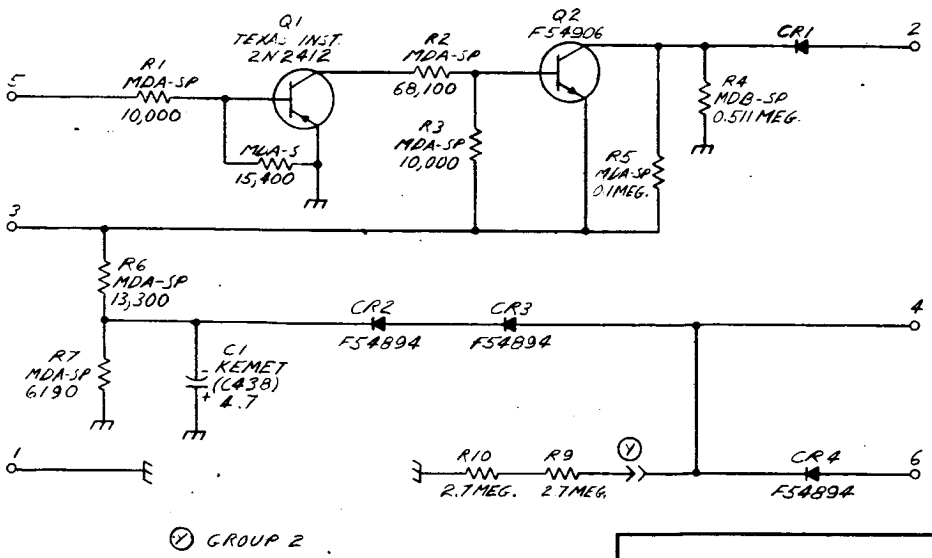

B-891433
EQUIPMENT INFO

1

B-891433

BIAS SUPPLY
CIRCUIT
(SERB EXPERIMENT)

INFORMATION

B-891434

BELL TELEPHONE LABORATORIES
INCORPORATED

DWG SIZE 6S

PRINTED IN U.S.A.

PHOTO NO. [redacted]

BELL TELEPHONE LABORATORIES

CASE NO. [redacted]

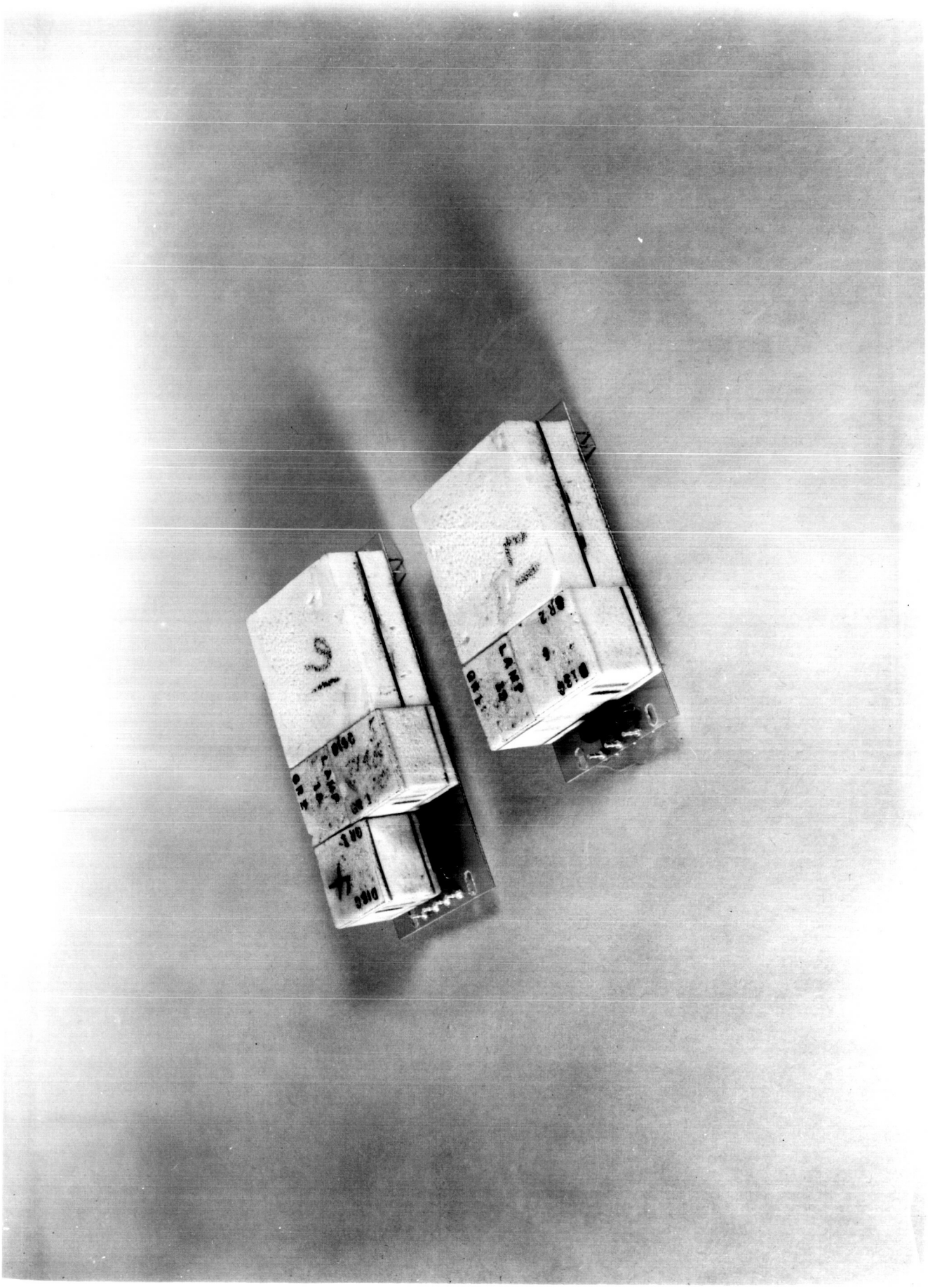

Fig. 2-12

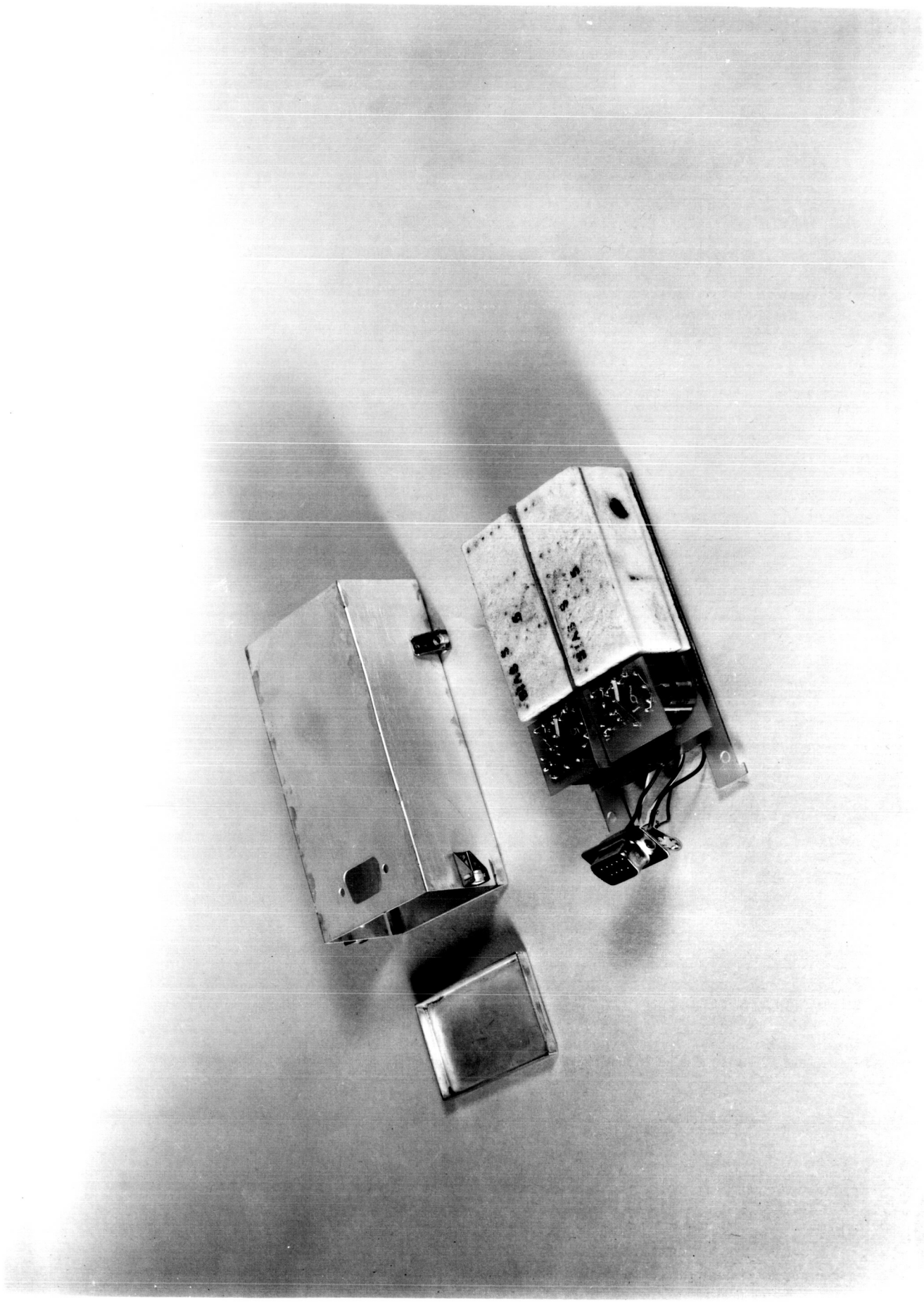

PHOTO NO. [redacted]

BELL TELEPHONE LABORATORIES

CASE NO. [redacted]

Fig. 2-13

BELL TELEPHONE LABORATORIES
INCORPORATED

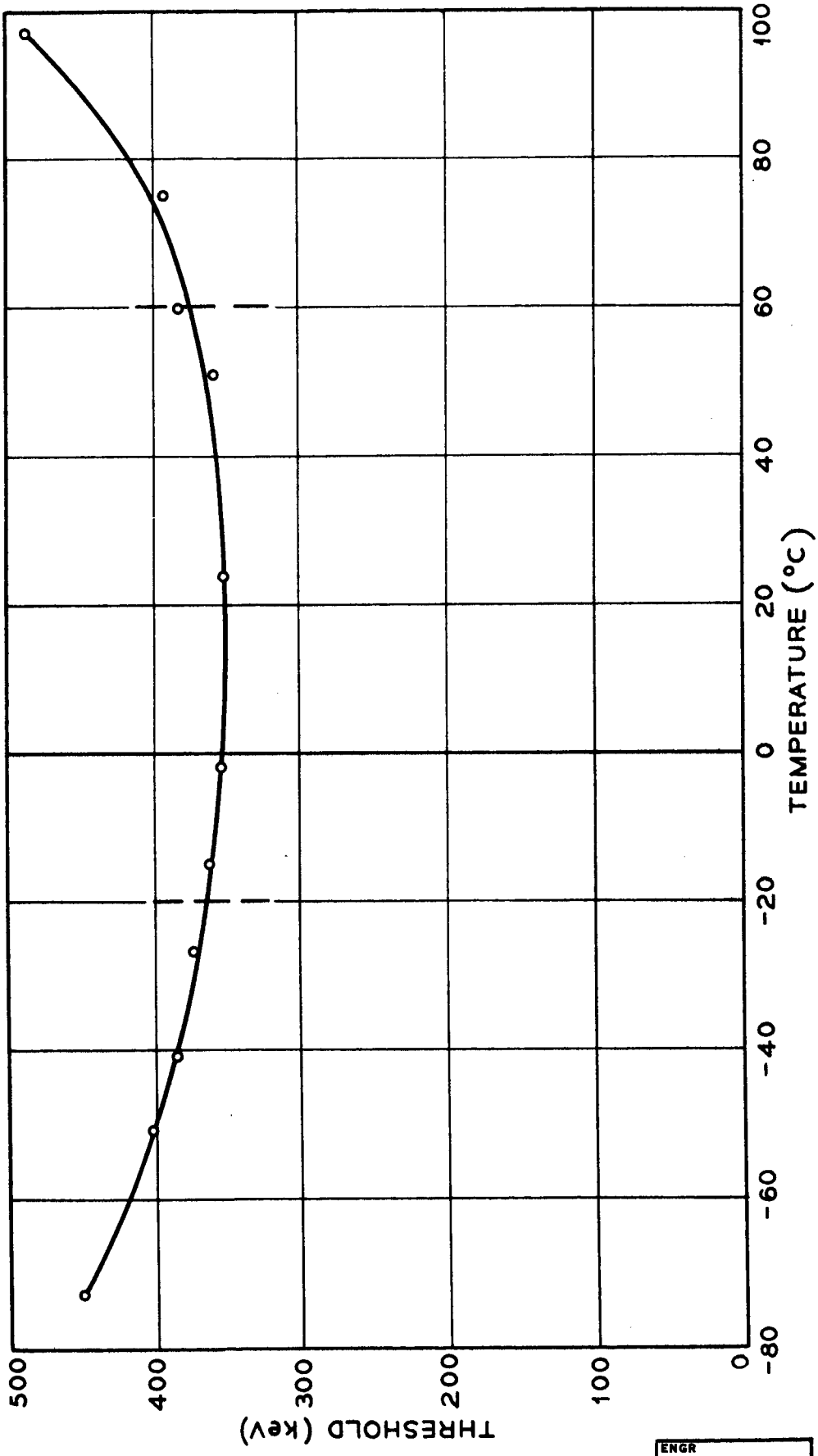

Fig. 2-14

			ENGR
			DRAWN
		DATE	CASE

OGILVIE PRESS, INC. PI 128
PRINTED IN U.S.A. E-7544 (8-60)

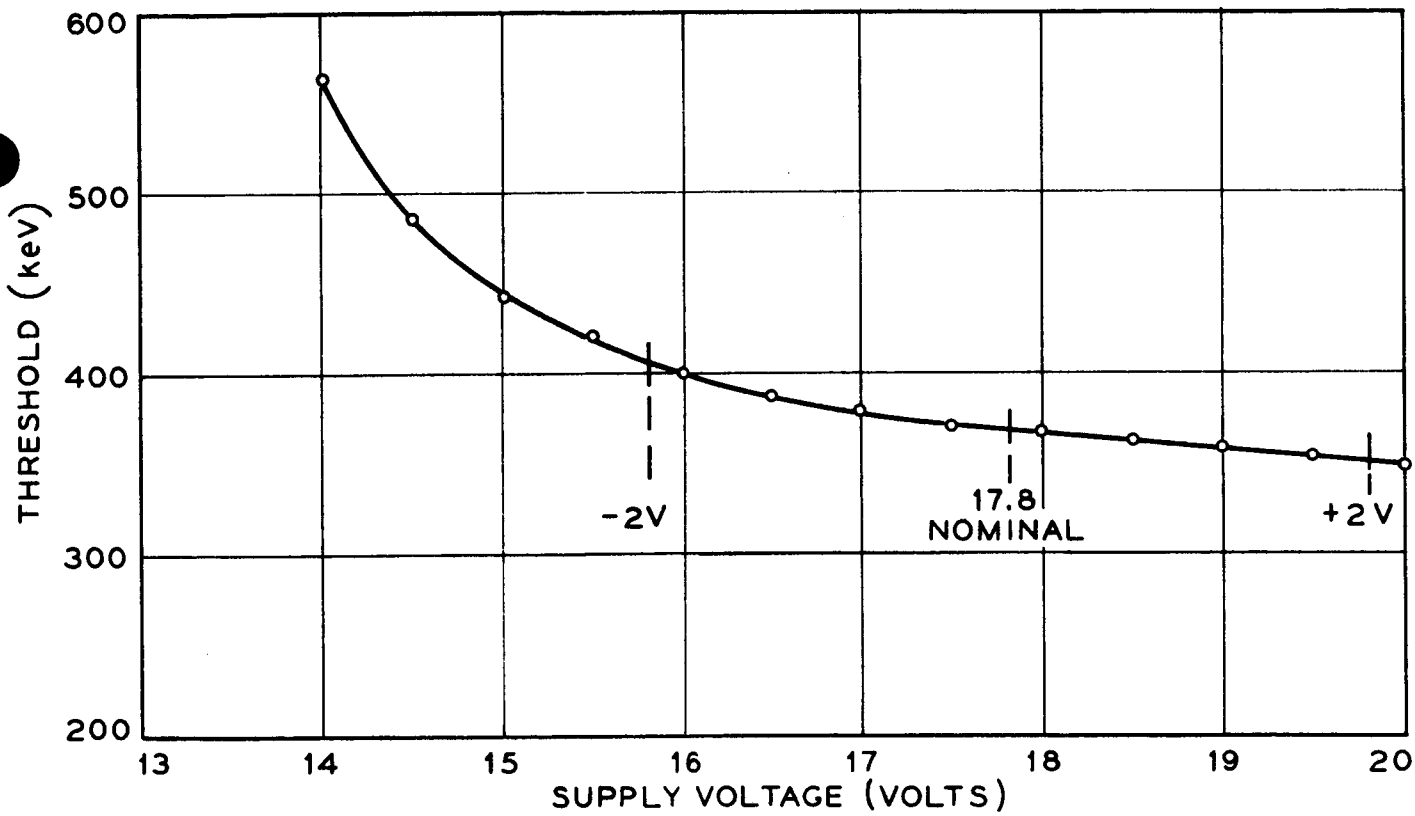

Fig. 2-15

OGILVIE PRESS, INC. PI 125
PRINTED IN U.S.A. E-7544 (8-60)

		ENGR
		DRAWN
	DATE	CASE

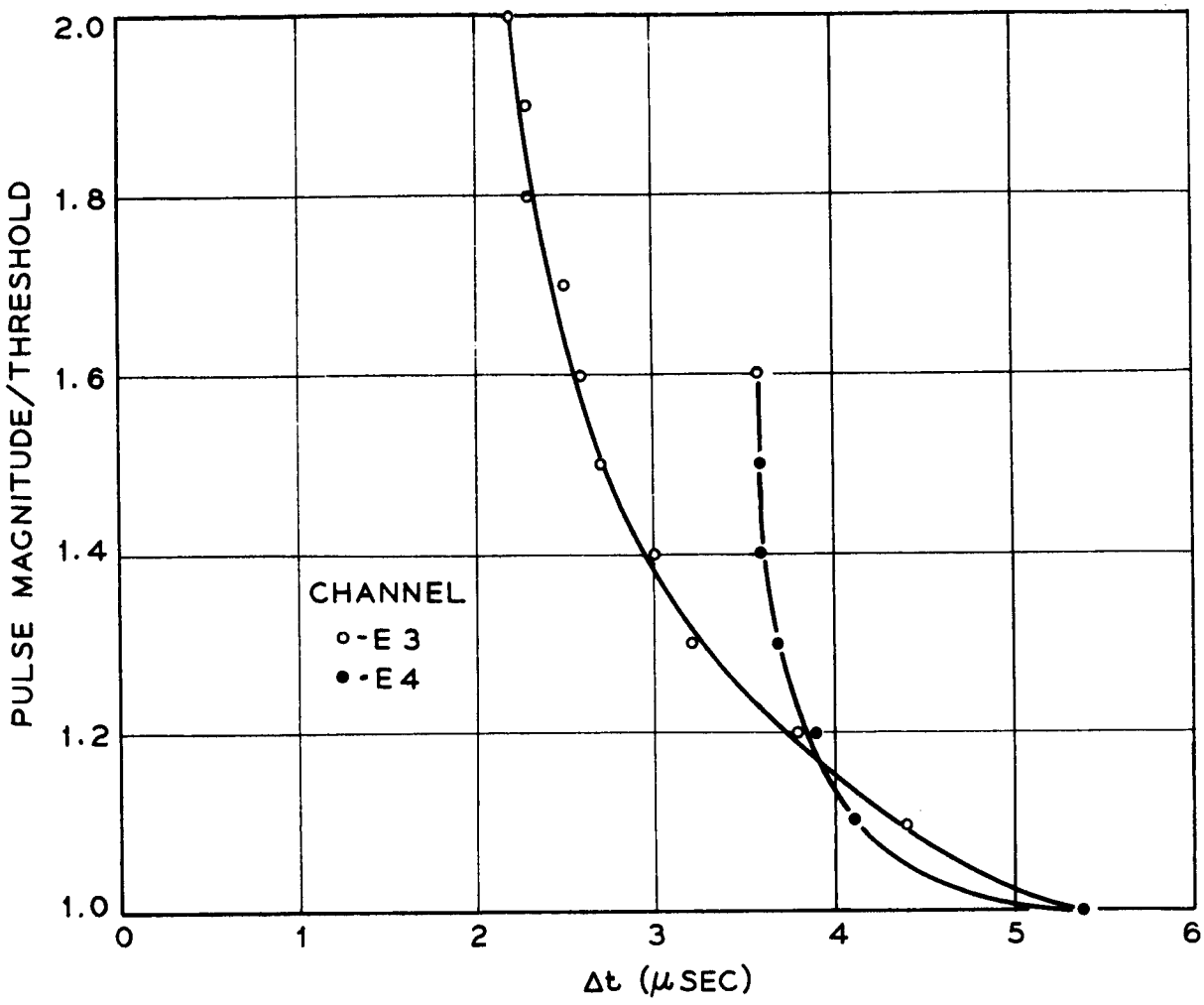

Fig. 2-16

			ENGR
			DRAWN
		DATE	CASE

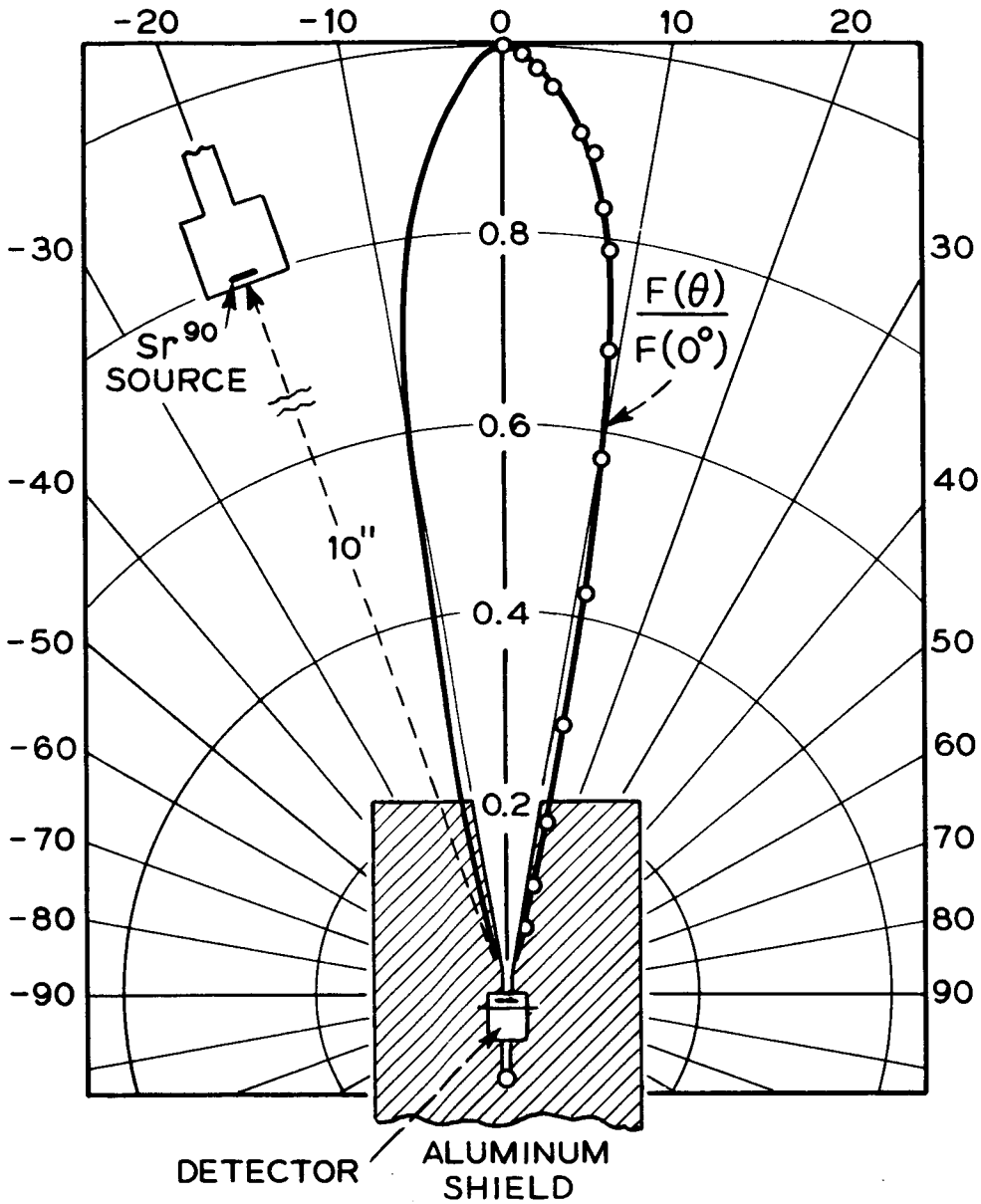
-20
-10
0
10
20
-30
30
-40
40
-50
50
-60
60
-70
70
-80
80
-90
90
0.8
0.6
0.4
0.2
F(θ)
F(0°)
Sr 90
SOURCE
10"
DETECTOR
ALUMINUM
SHIELD

Fig. 2-17

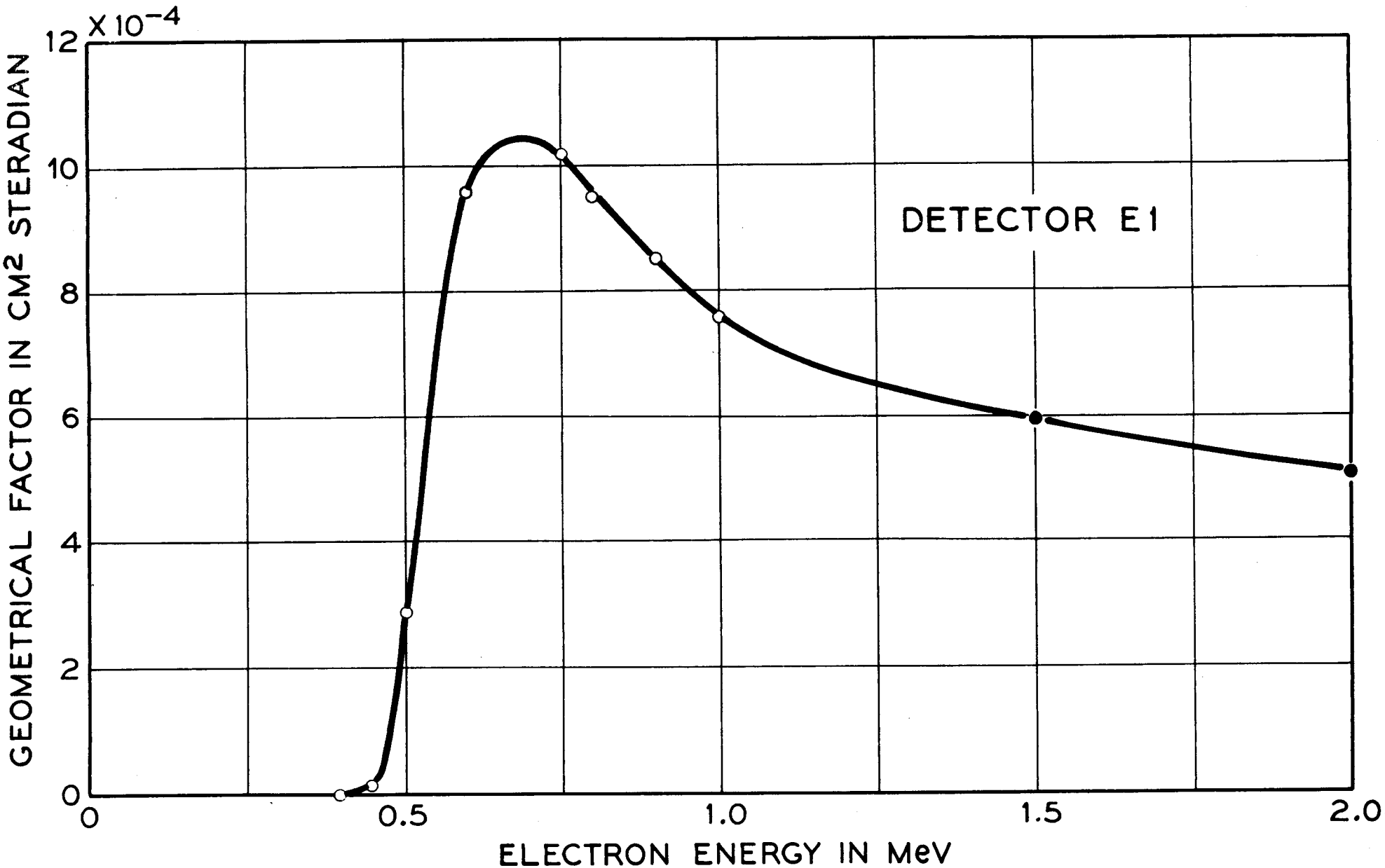
X 10⁻⁴
12
10
8
6
4
2
0
GEOMETRICAL FACTOR IN CM² STERADIAN
DETECTOR E1
0
0.5
1.0
1.5
2.0
ELECTRON ENERGY IN MeV

Fig. 2-18

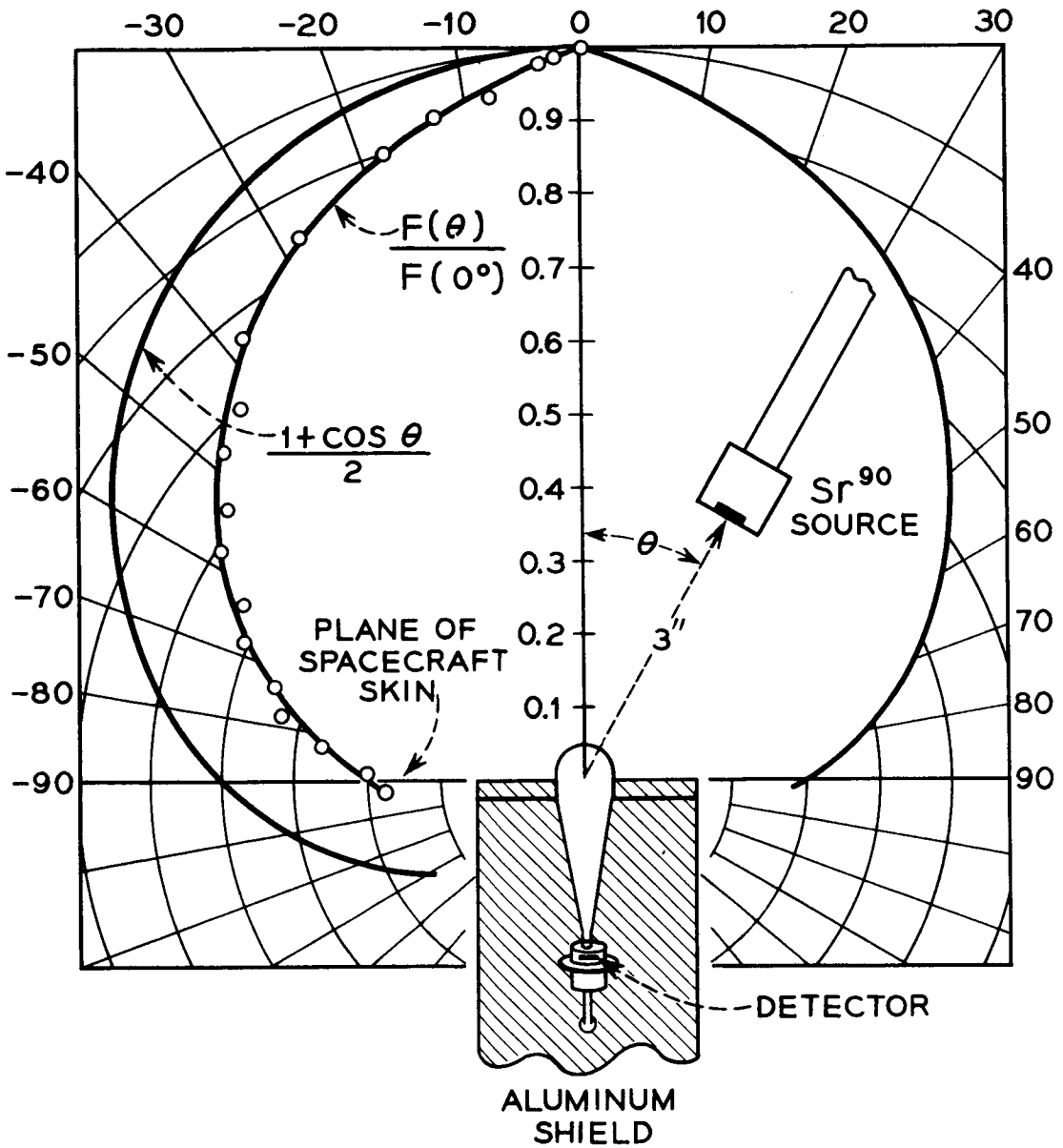
-30
-20
-10
0
10
20
30
-40
-50
-60
-70
-80
-90
40
50
60
70
80
90
0.9
0.8
0.7
0.6
0.5
0.4
0.3
0.2
0.1
F(θ) / F(0°)
1+COS θ / 2
Sr90 SOURCE
θ
3"
PLANE OF SPACECRAFT SKIN
DETECTOR
ALUMINUM SHIELD

Fig. 2-19

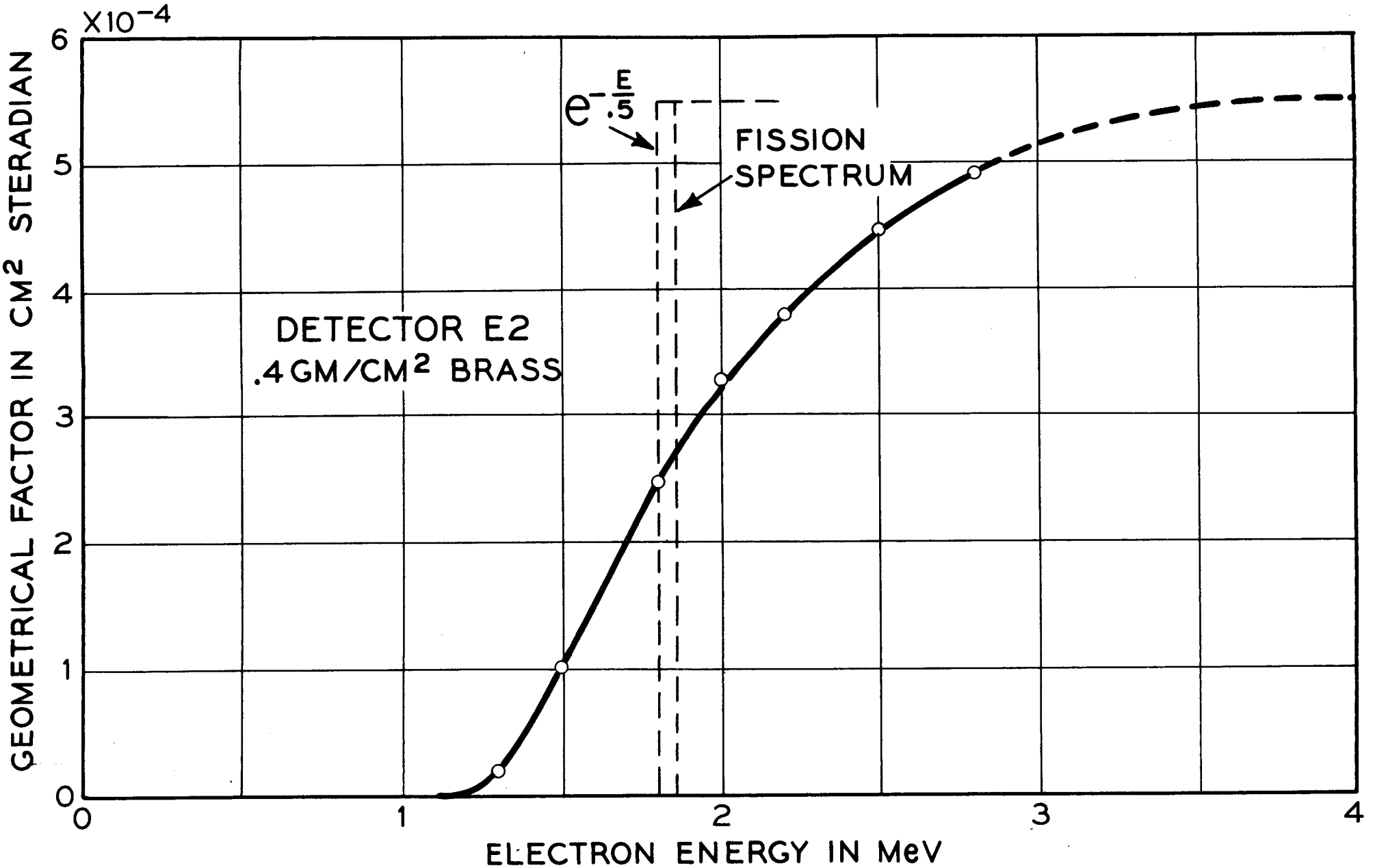
X10⁻⁴
6
5
4
3
2
1
0
GEOMETRICAL FACTOR IN CM² STERADIAN
0
1
2
3
4
ELECTRON ENERGY IN MeV
e^(-E/.5)
FISSION
SPECTRUM
DETECTOR E2
.4 GM/CM² BRASS

Fig. 2-20

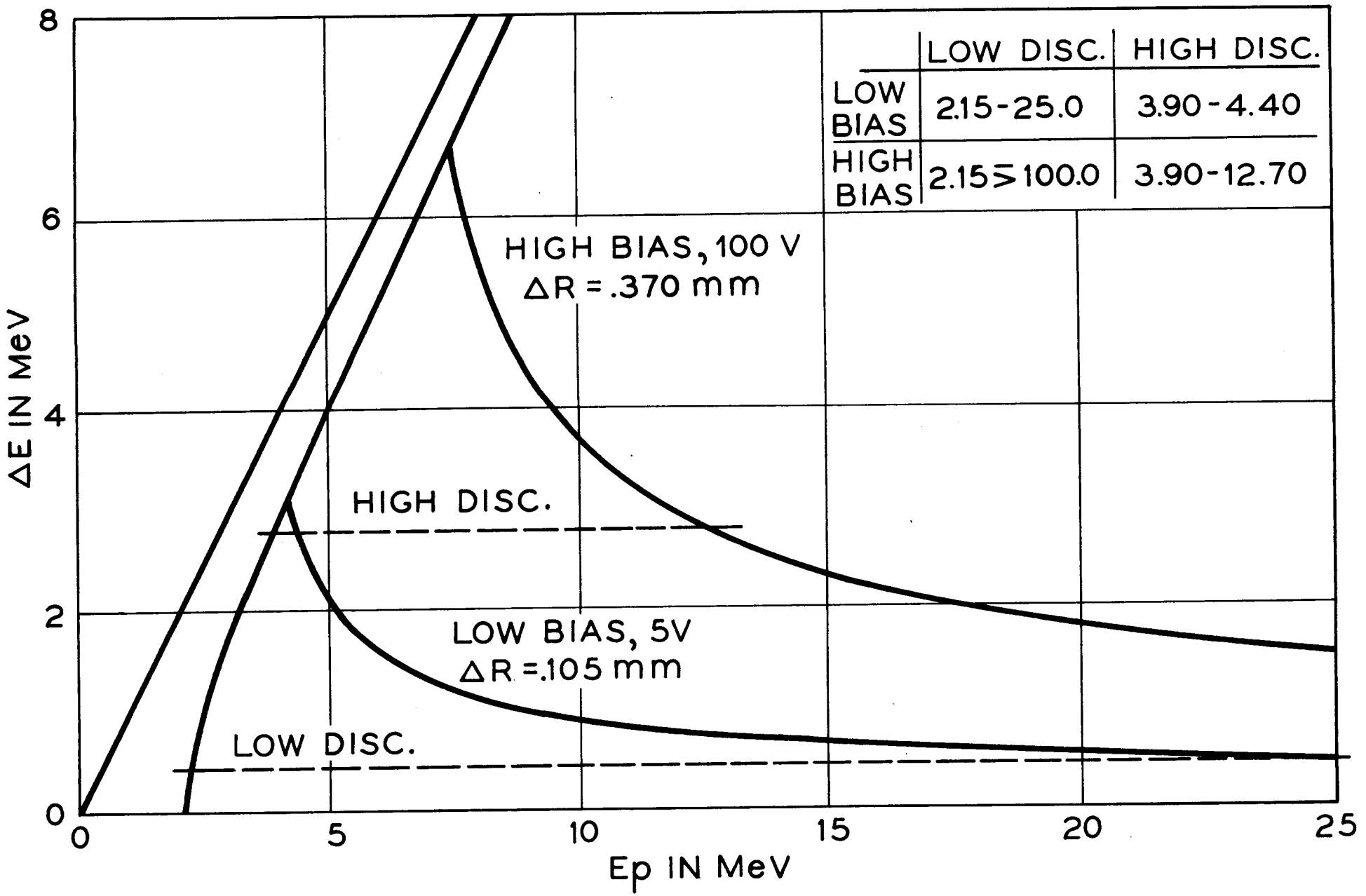
LOW DISC.
HIGH DISC.
LOW BIAS
2.15-25.0
3.90-4.40
HIGH BIAS
2.15≥100.0
3.90-12.70
HIGH BIAS, 100 V
ΔR = .370 mm
HIGH DISC.
LOW BIAS, 5V
ΔR =.105 mm
LOW DISC.
ΔE IN MeV
Ep IN MeV
0
2
4
6
8
0
5
10
15
20
25

Fig. 2-21

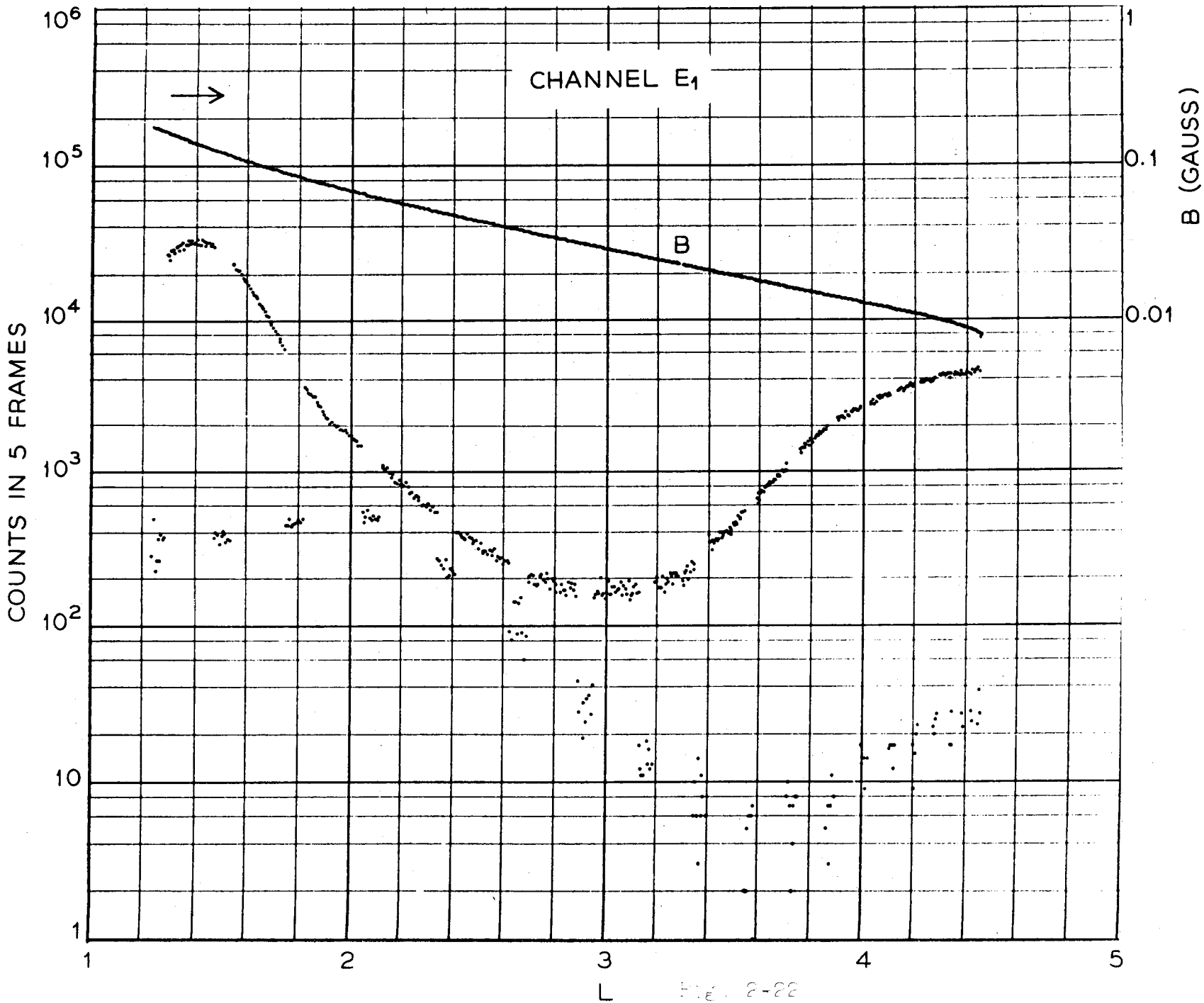
CHANNEL E_1
B
COUNTS IN 5 FRAMES
B (GAUSS)
L
10^6
10^5
10^4
10^3
10^2
10
1
1
0.1
0.01
1
2
3
4
5

FIG. 2-22

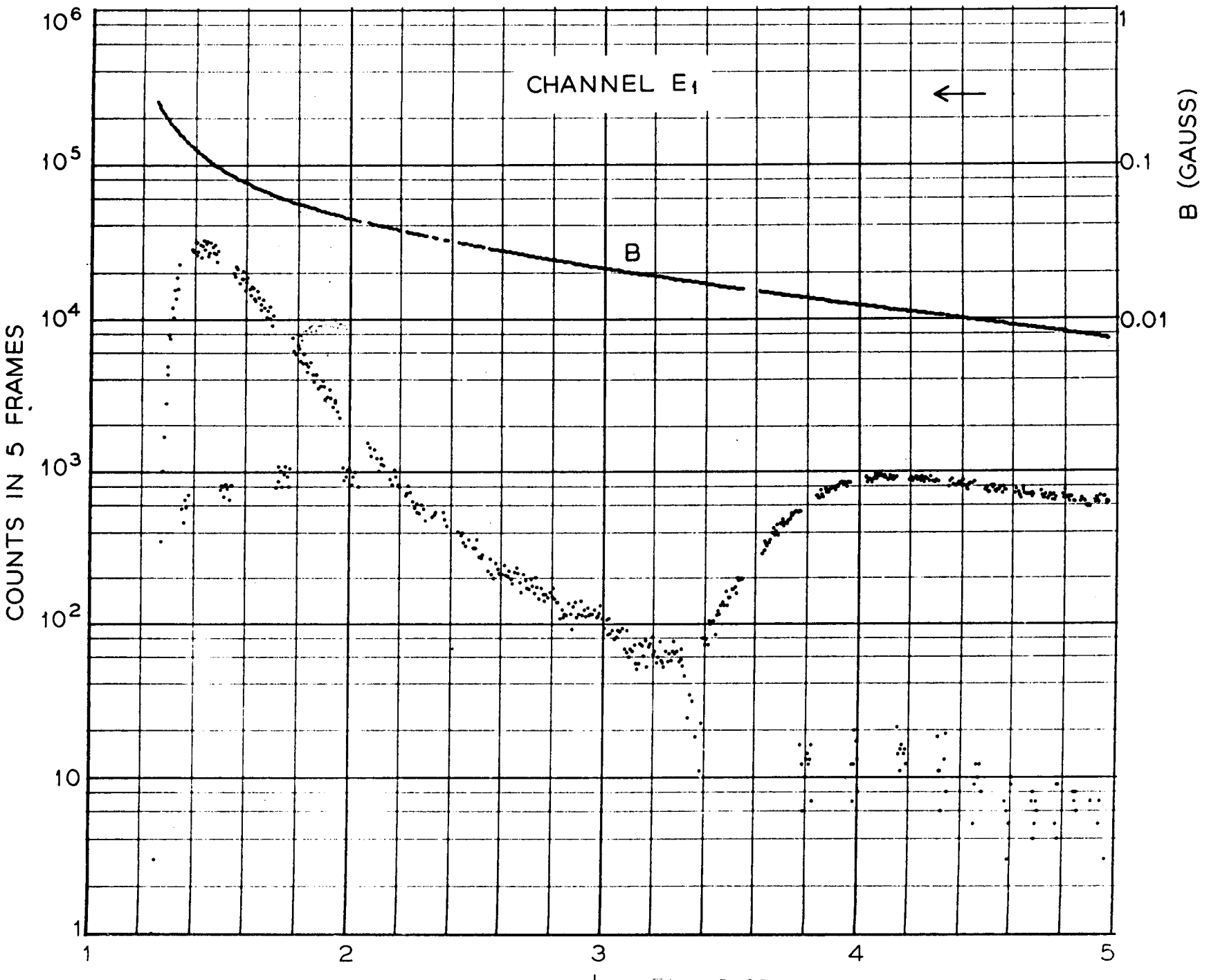
CHANNEL E1
B
COUNTS IN 5 FRAMES
B (GAUSS)
L
10^6
10^5
10^4
10^3
10^2
10
1
1
0.1
0.01
1
2
3
4
5

Fig. 2-23

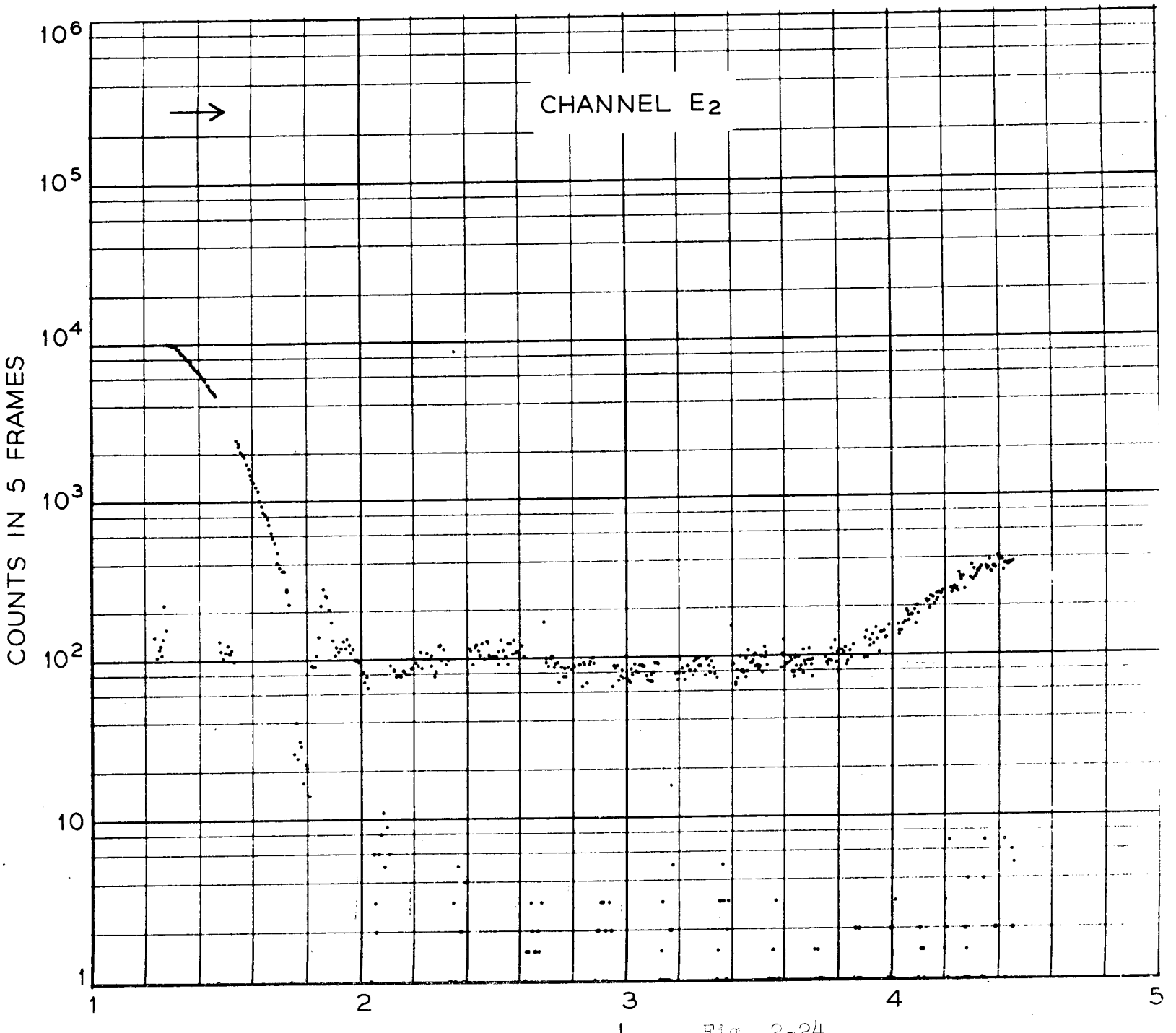

Fig. 2-24

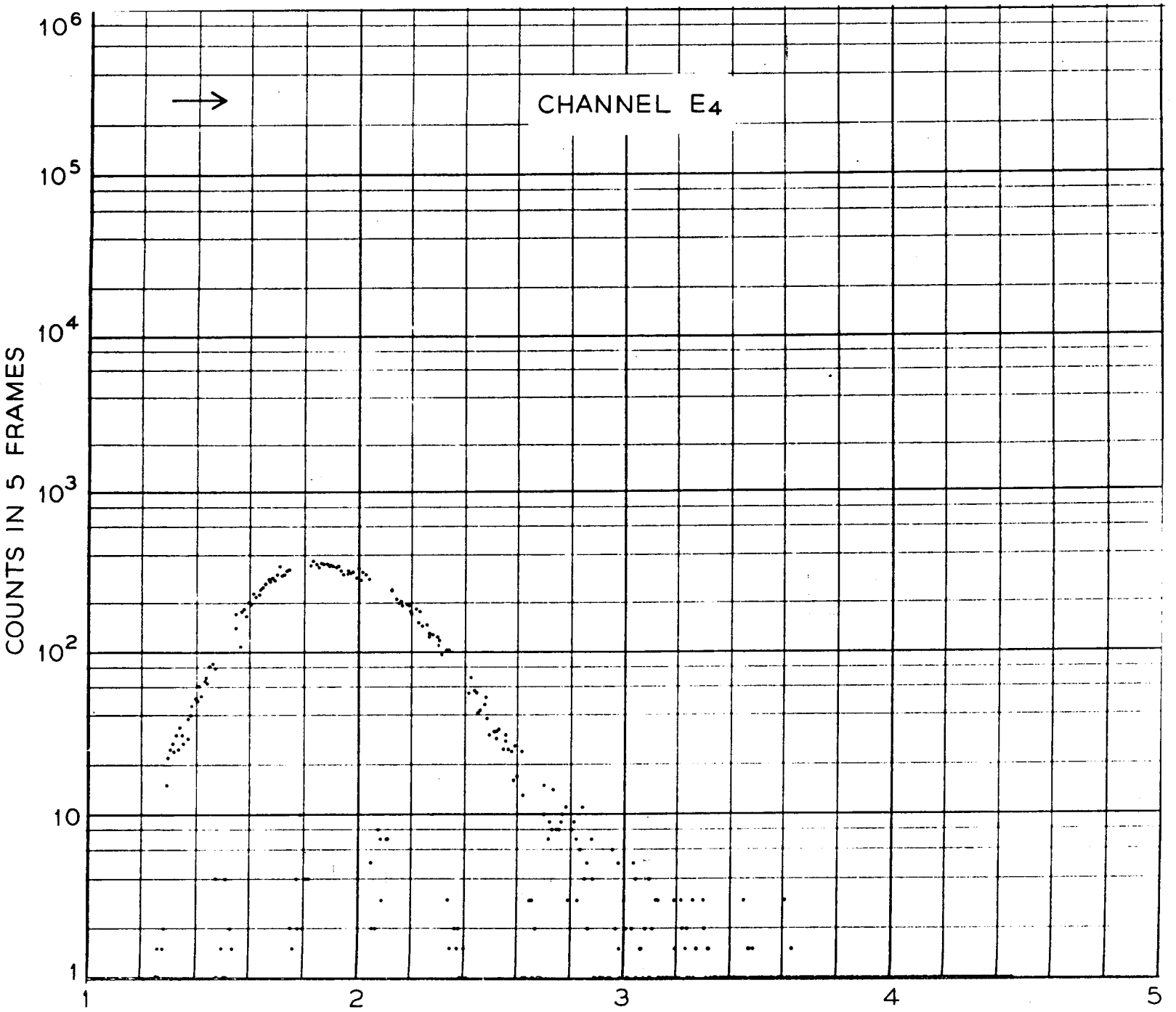

FIG. 2-25

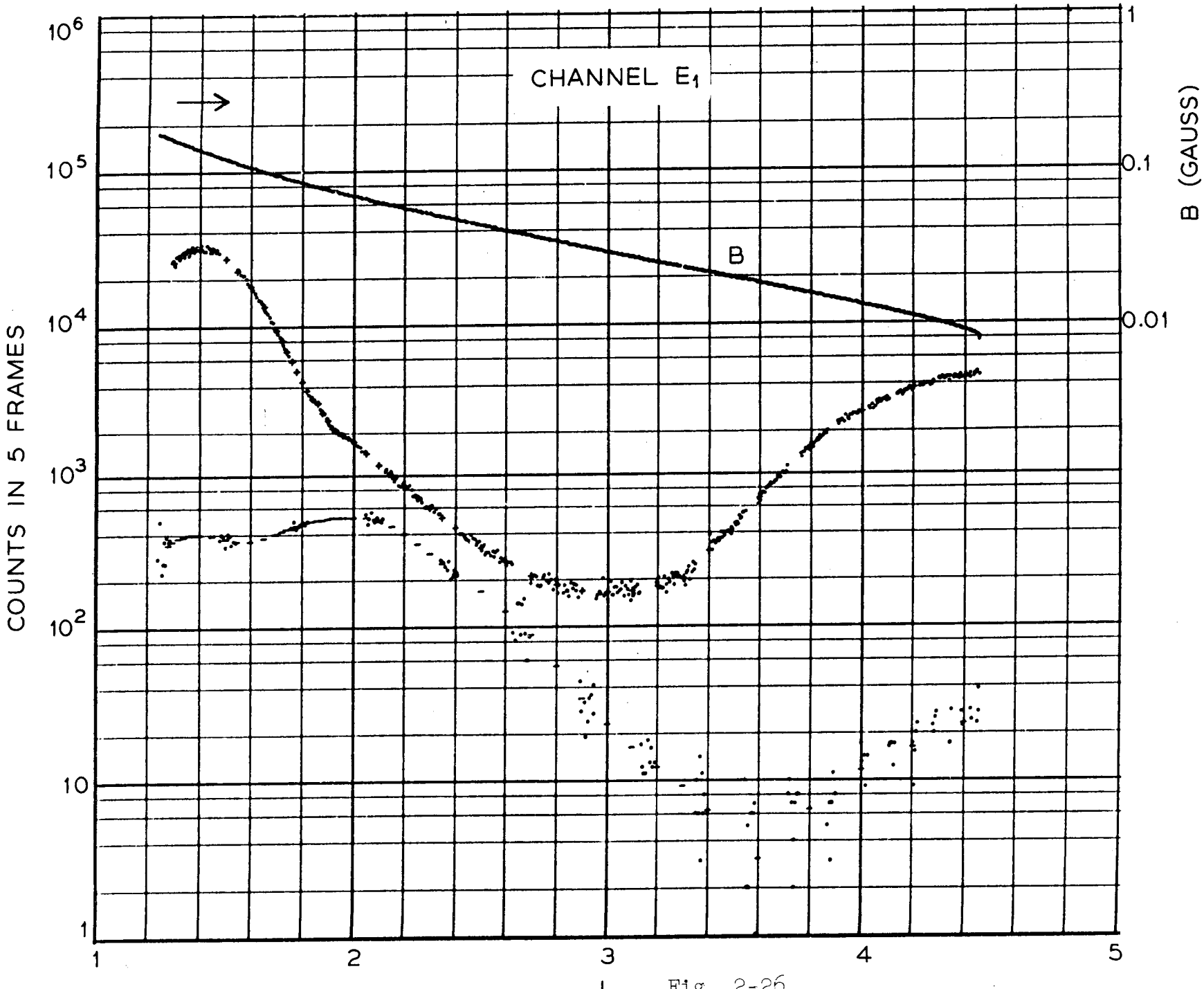
CHANNEL E1
B
COUNTS IN 5 FRAMES
B (GAUSS)
L
10^6
10^5
10^4
10^3
10^2
10
1
1
0.1
0.01
1
2
3
4
5

Fig. 2-26

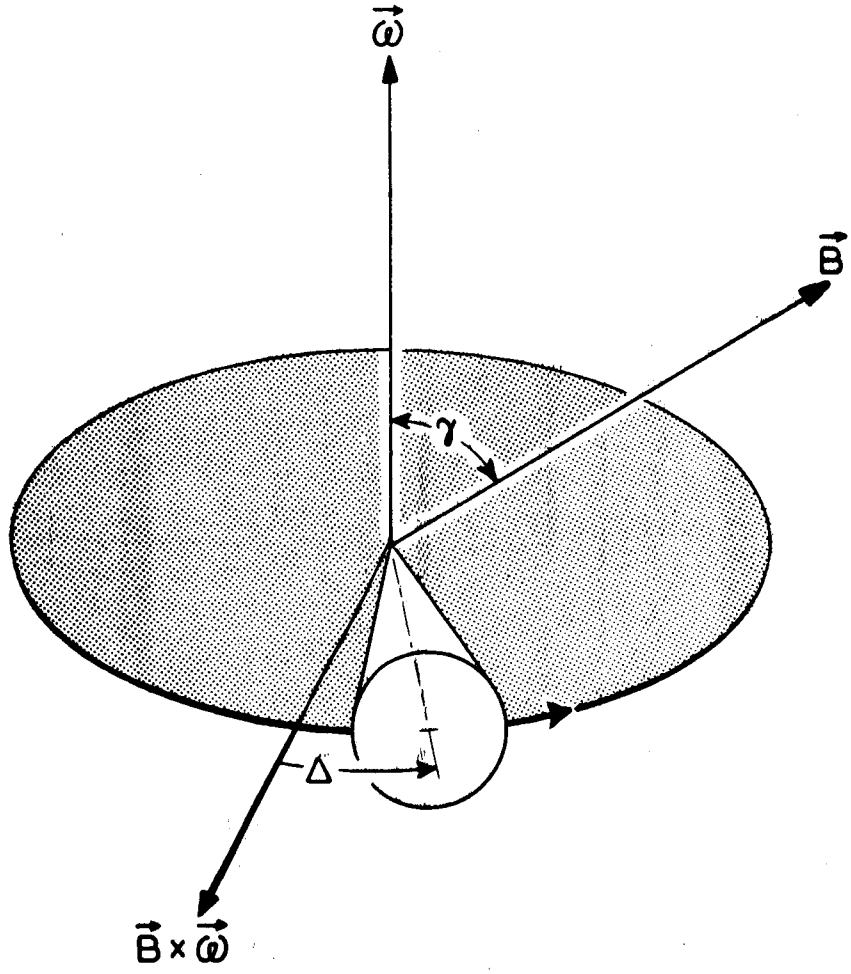

Fig. 2-27

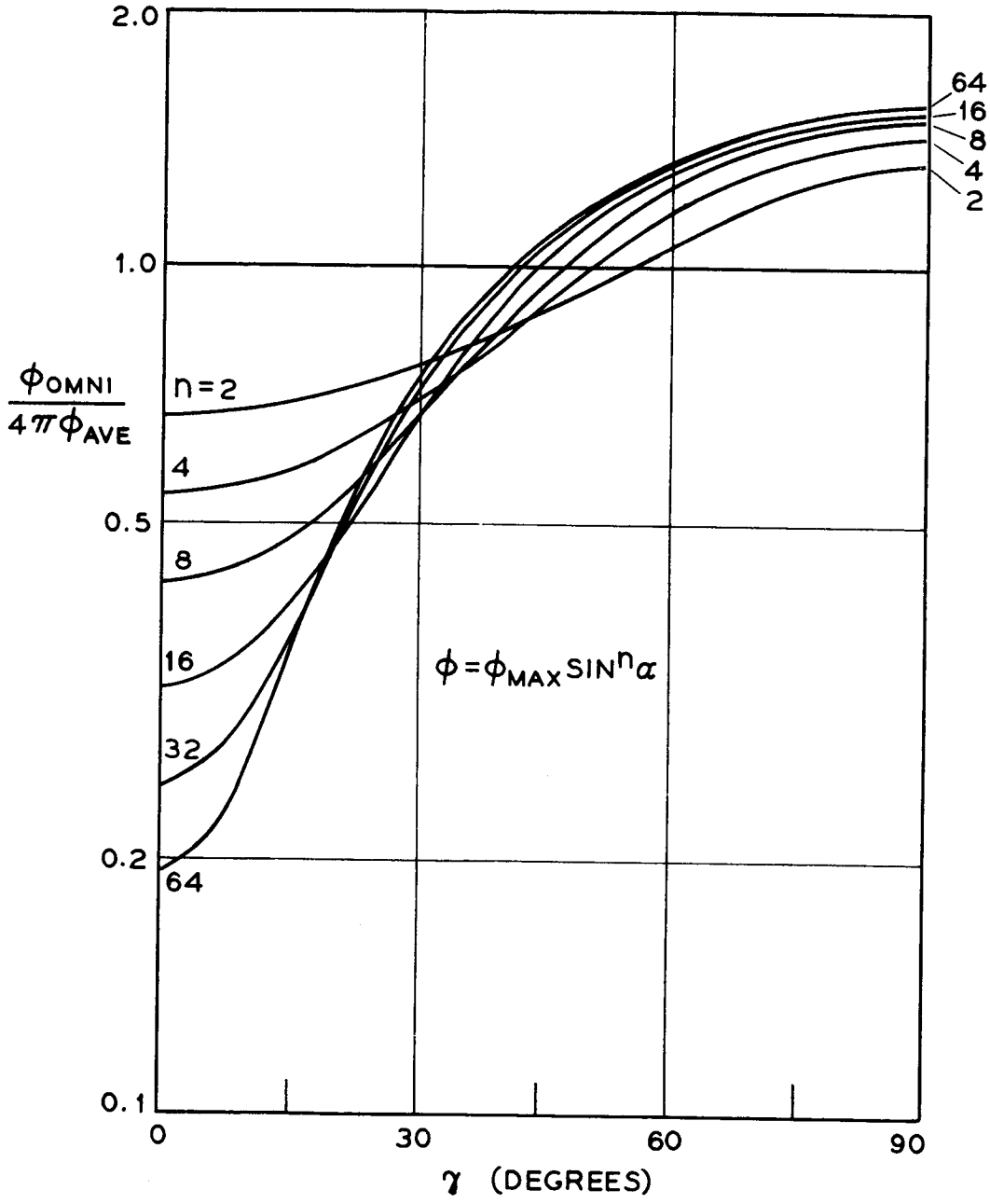

Fig. 2-28

OGILVIE PRESS, INC. PI 125
PRINTED IN U.S.A. E-7544 (8-60)

			ENGR
			DRAWN
		DATE	CASE

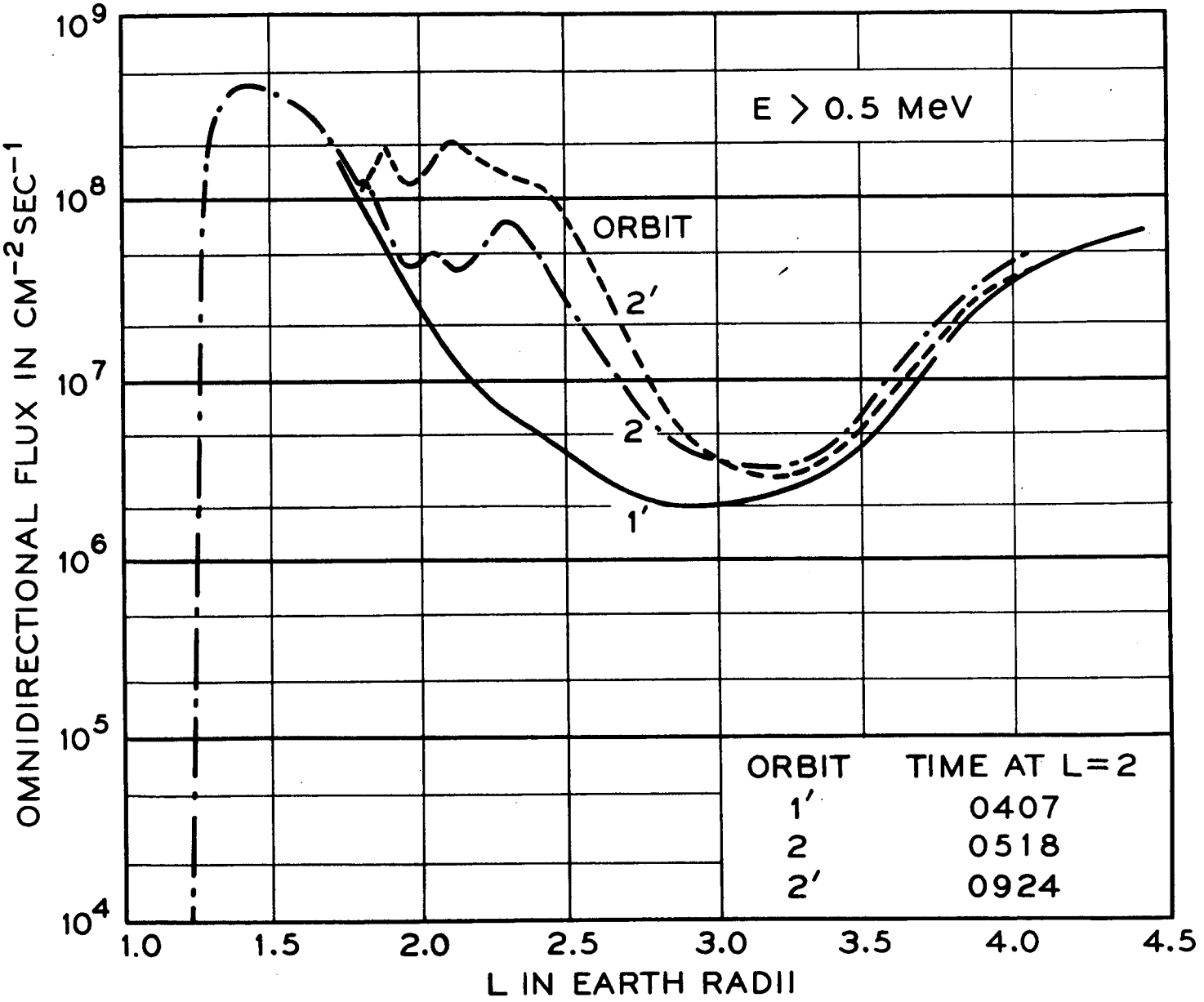
E > 0.5 MeV
ORBIT
2′
2
1′
ORBIT TIME AT L=2
1′ 0407
2 0518
2′ 0924
OMNIDIRECTIONAL FLUX IN CM^{-2}SEC^{-1}
10^9
10^8
10^7
10^6
10^5
10^4
1.0
1.5
2.0
2.5
3.0
3.5
4.0
4.5
L IN EARTH RADII

Fig. 2-~~30~~ 29

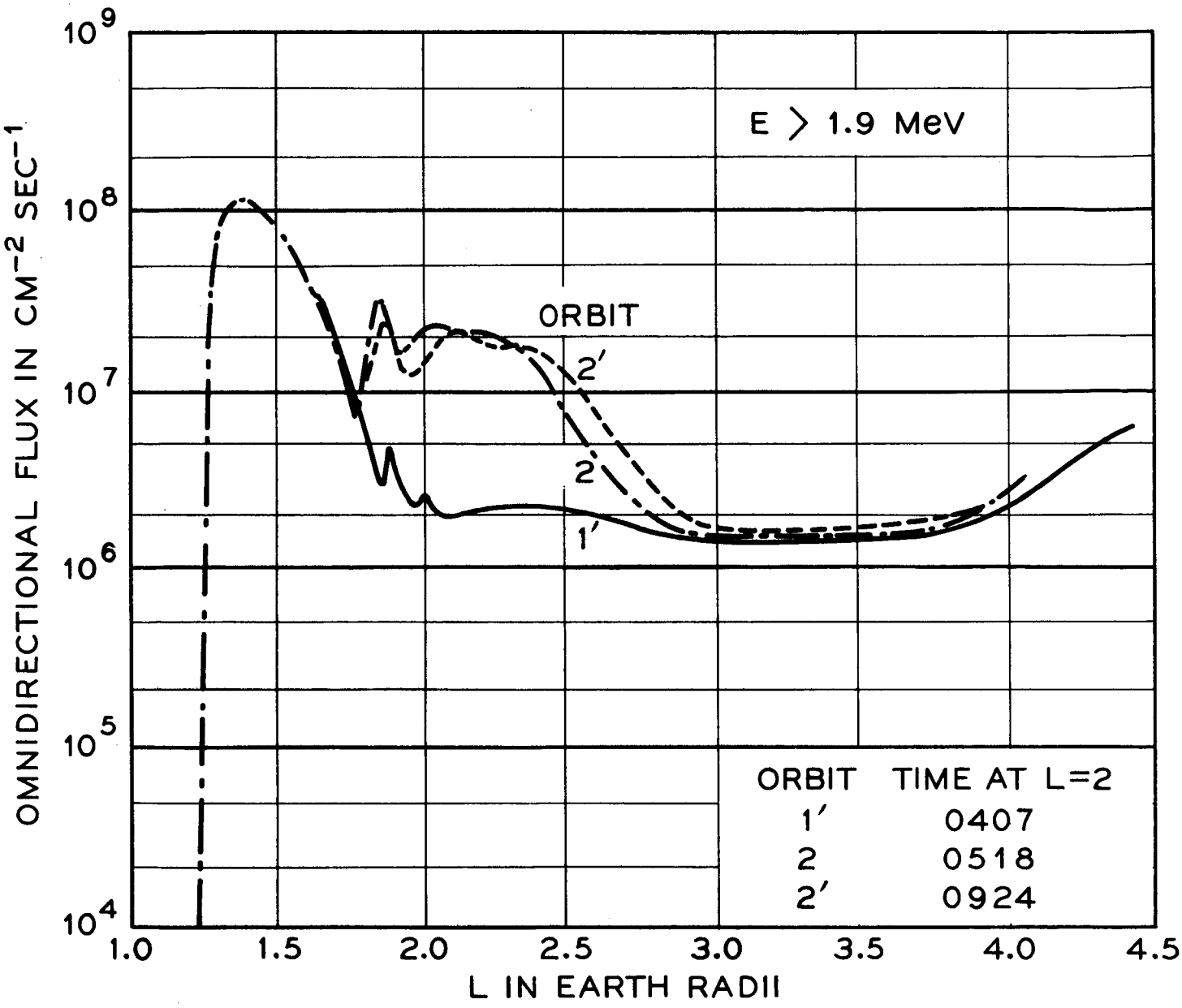
E > 1.9 MeV
ORBIT
2′
2
1′
ORBIT TIME AT L=2
1′ 0407
2 0518
2′ 0924
OMNIDIRECTIONAL FLUX IN CM^{-2} SEC^{-1}
10^9
10^8
10^7
10^6
10^5
10^4
1.0
1.5
2.0
2.5
3.0
3.5
4.0
4.5
L IN EARTH RADII

Fig. 2-~~31~~ 40

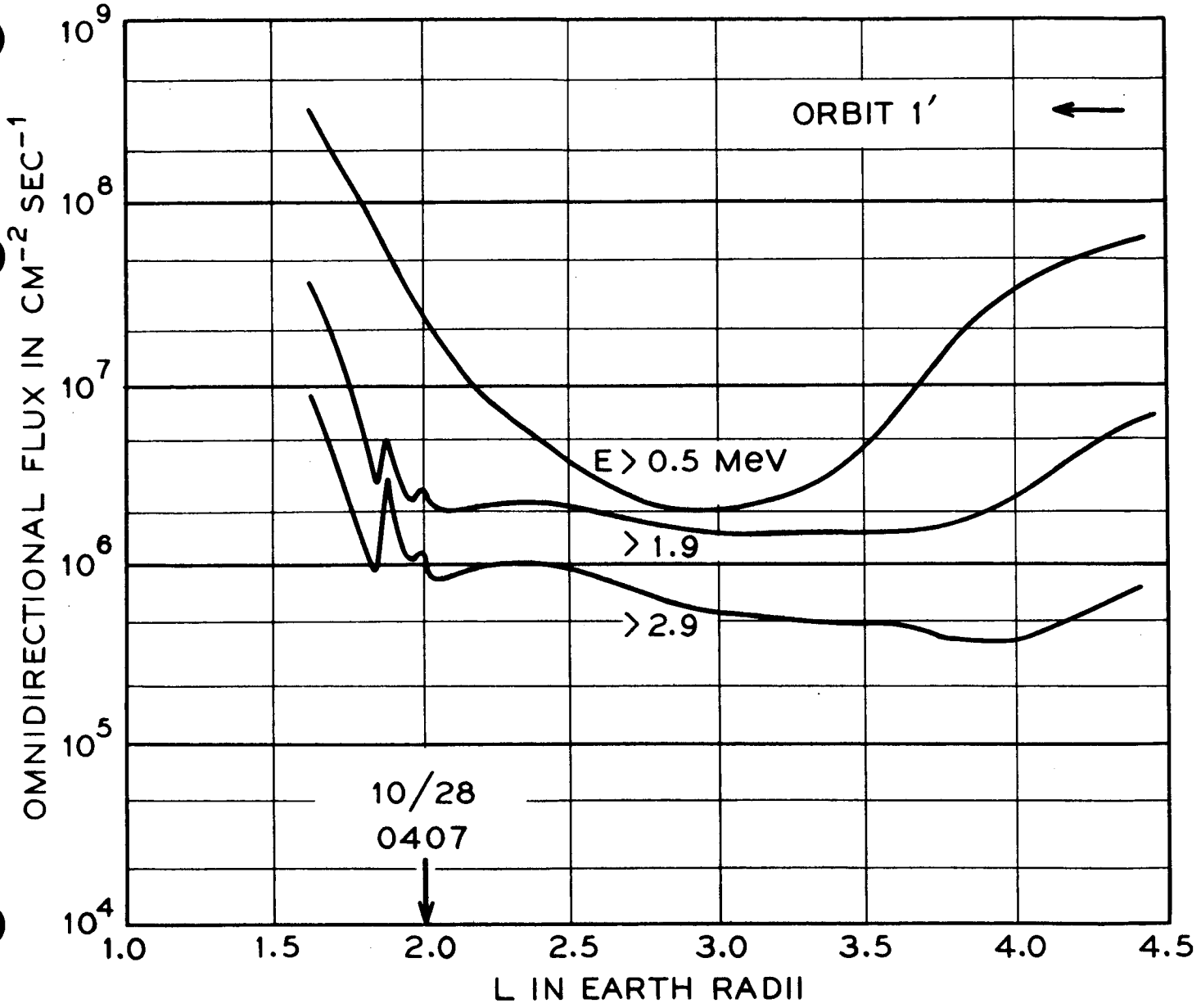
ORBIT 1′
E > 0.5 MeV
> 1.9
> 2.9
10/28
0407
OMNIDIRECTIONAL FLUX IN CM^{-2} SEC^{-1}
10^9
10^8
10^7
10^6
10^5
10^4
1.0
1.5
2.0
2.5
3.0
3.5
4.0
4.5
L IN EARTH RADII

Fig. 2-~~32~~ 31

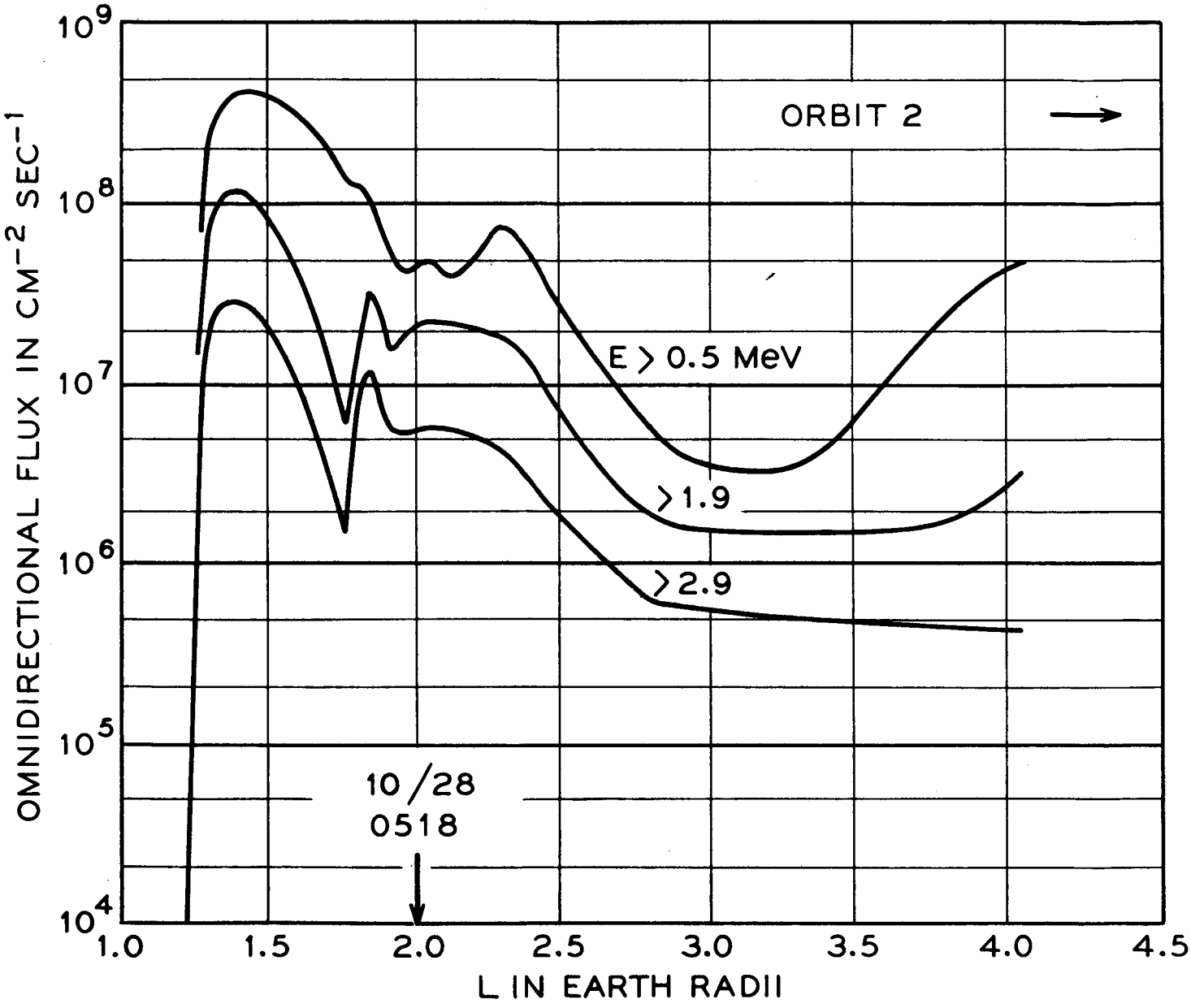
ORBIT 2
E > 0.5 MeV
> 1.9
> 2.9
10/28
0518
OMNIDIRECTIONAL FLUX IN CM^{-2} SEC^{-1}
L IN EARTH RADII
10^9
10^8
10^7
10^6
10^5
10^4
1.0
1.5
2.0
2.5
3.0
3.5
4.0
4.5

Fig. 2 ~~33~~ 32

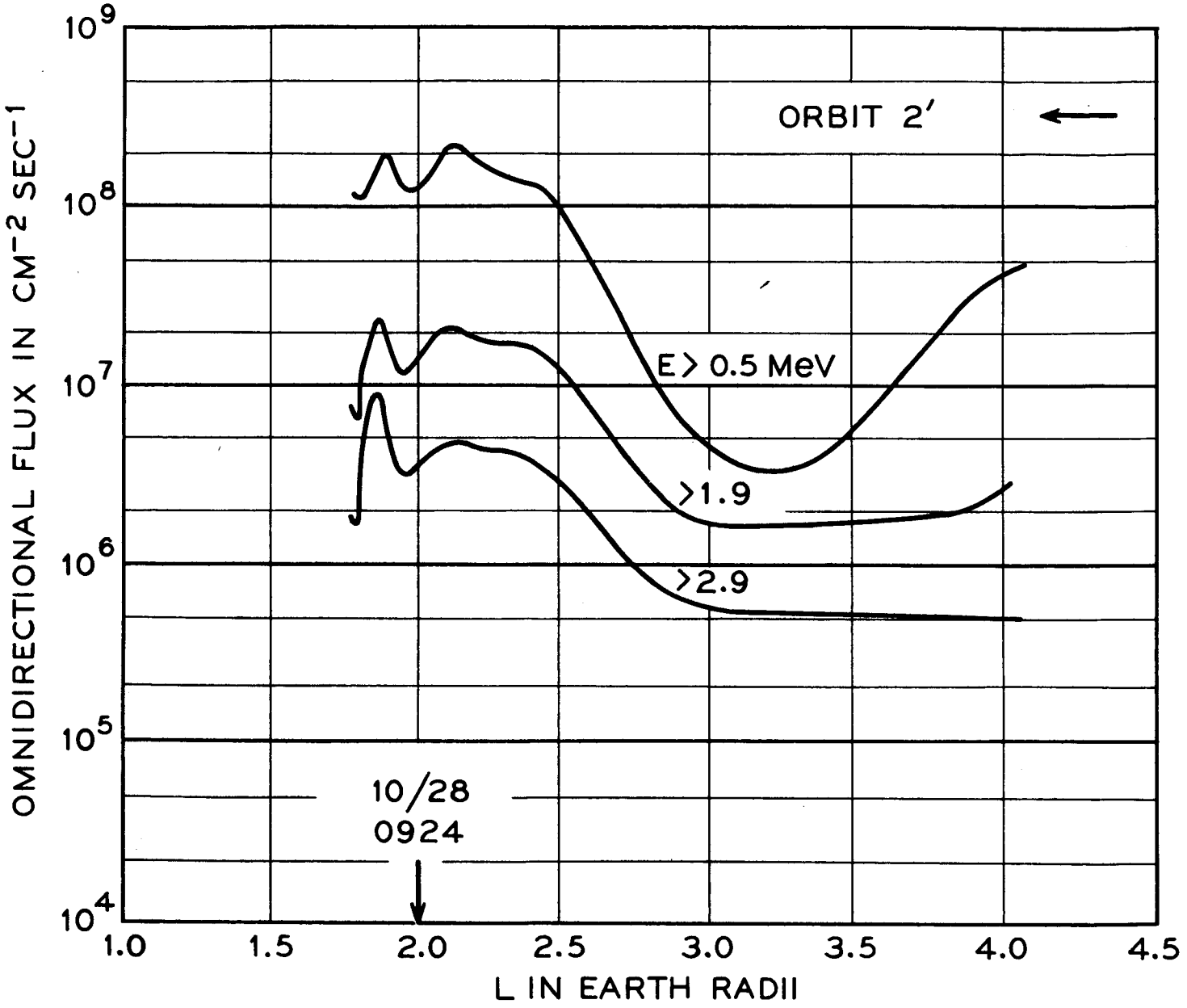
ORBIT 2′
E > 0.5 MeV
>1.9
>2.9
10/28
0924
OMNIDIRECTIONAL FLUX IN CM^{-2} SEC^{-1}
10^9
10^8
10^7
10^6
10^5
10^4
1.0
1.5
2.0
2.5
3.0
3.5
4.0
4.5
L IN EARTH RADII

Fig. 2-~~34~~ 33

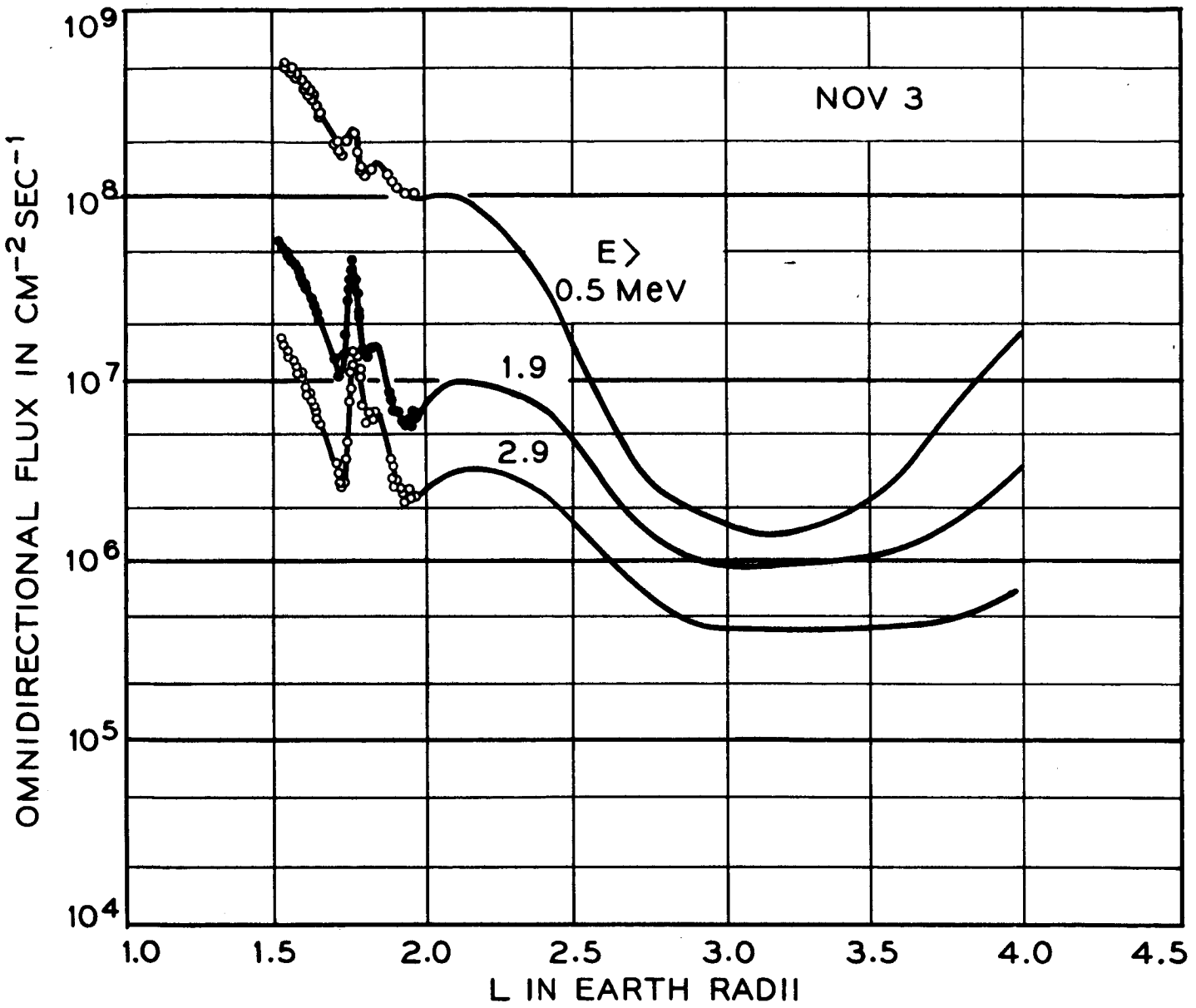
NOV 3
E>
0.5 MeV
1.9
2.9
OMNIDIRECTIONAL FLUX IN CM^{-2}SEC^{-1}
10^9
10^8
10^7
10^6
10^5
10^4
1.0
1.5
2.0
2.5
3.0
3.5
4.0
4.5
L IN EARTH RADII

Fig. 2-~~35~~ 34

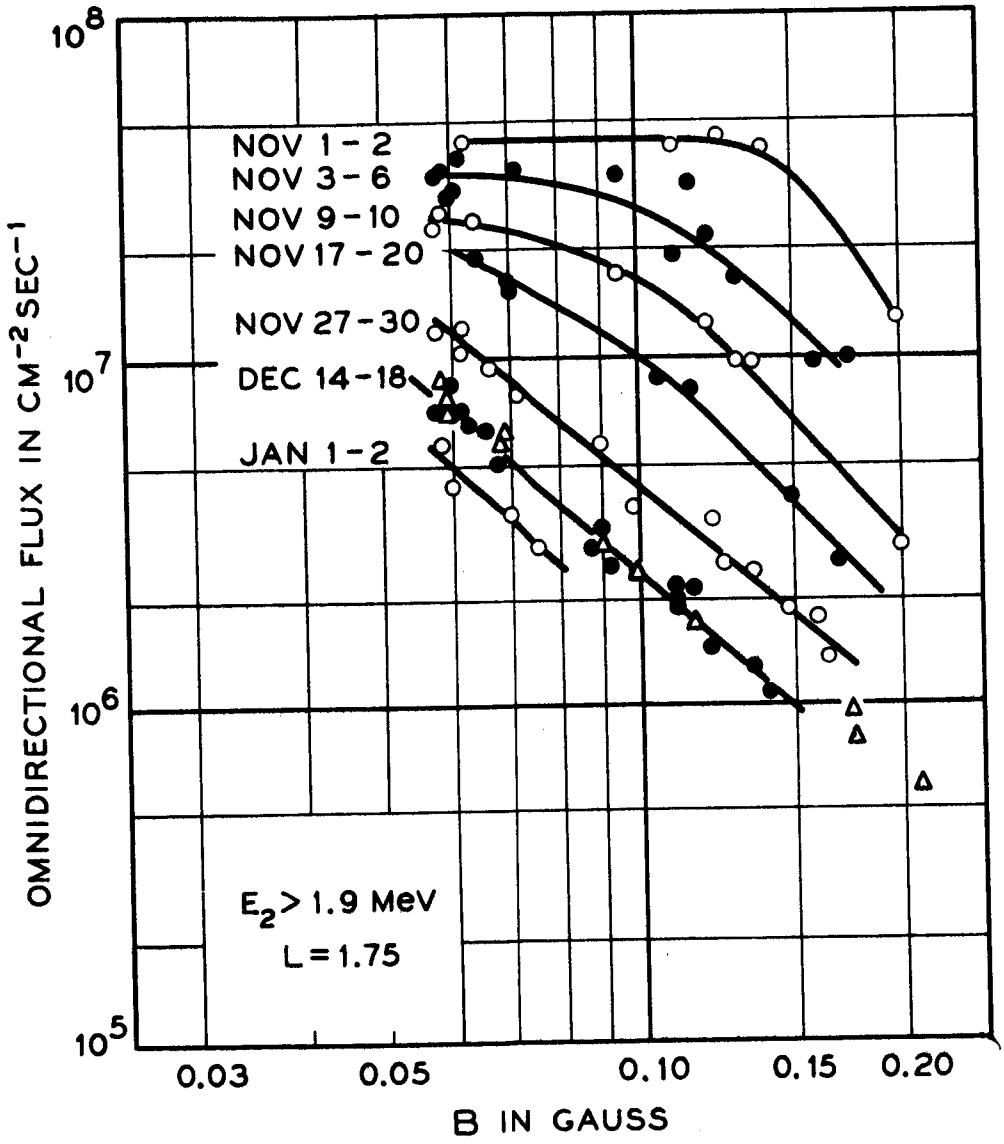
NOV 1 - 2
NOV 3 - 6
NOV 9 - 10
NOV 17 - 20
NOV 27 - 30
DEC 14 - 18
JAN 1 - 2
$E_2 > 1.9$ MeV
L = 1.75
OMNIDIRECTIONAL FLUX IN $CM^{-2}SEC^{-1}$
10^8
10^7
10^6
10^5
0.03
0.05
0.10
0.15
0.20
B IN GAUSS

Fig. 2-35

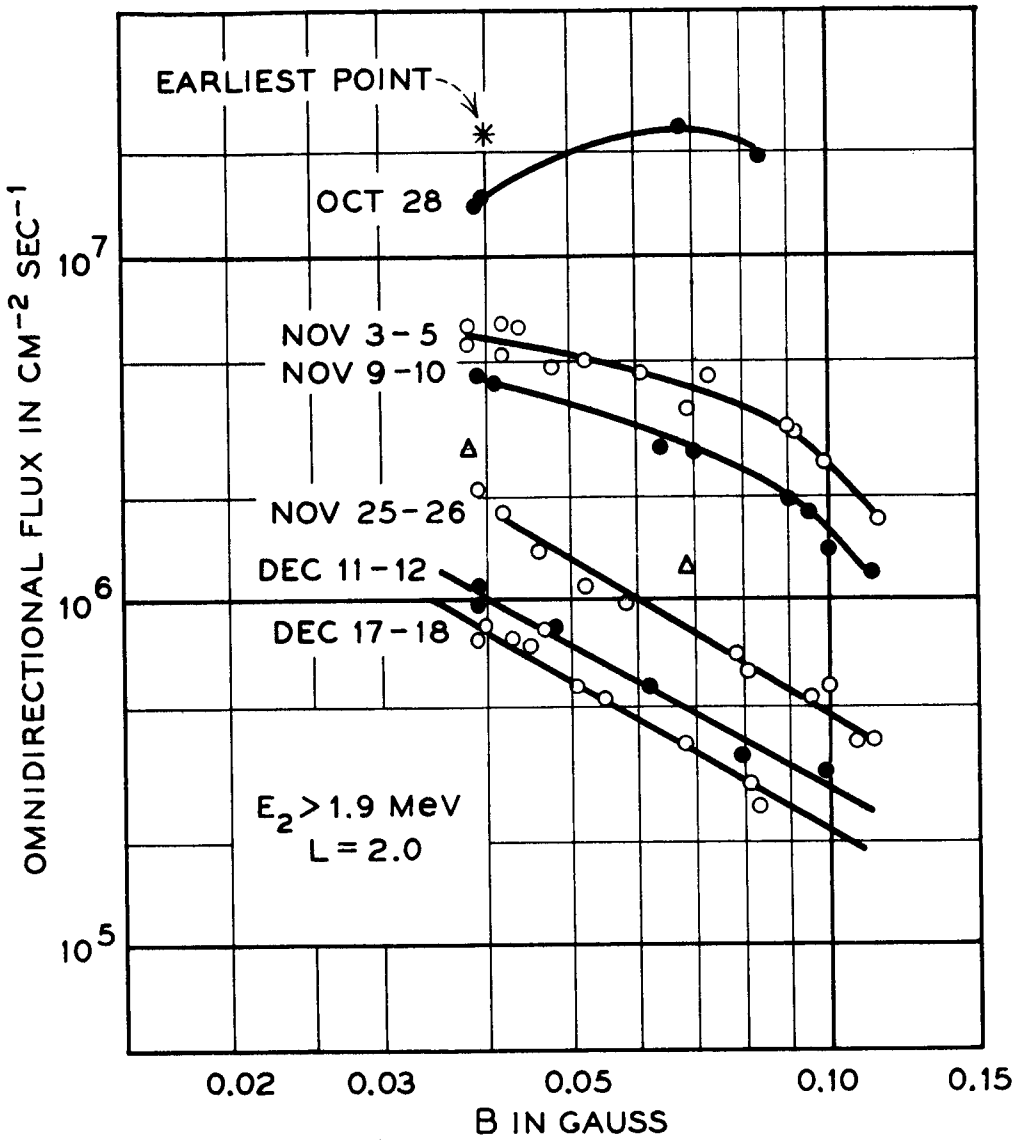
EARLIEST POINT
OCT 28
NOV 3-5
NOV 9-10
NOV 25-26
DEC 11-12
DEC 17-18
$E_2 > 1.9$ MeV
L = 2.0
OMNIDIRECTIONAL FLUX IN CM^{-2} SEC^{-1}
10^7
10^6
10^5
0.02
0.03
0.05
0.10
0.15
B IN GAUSS

Fig. 2-36

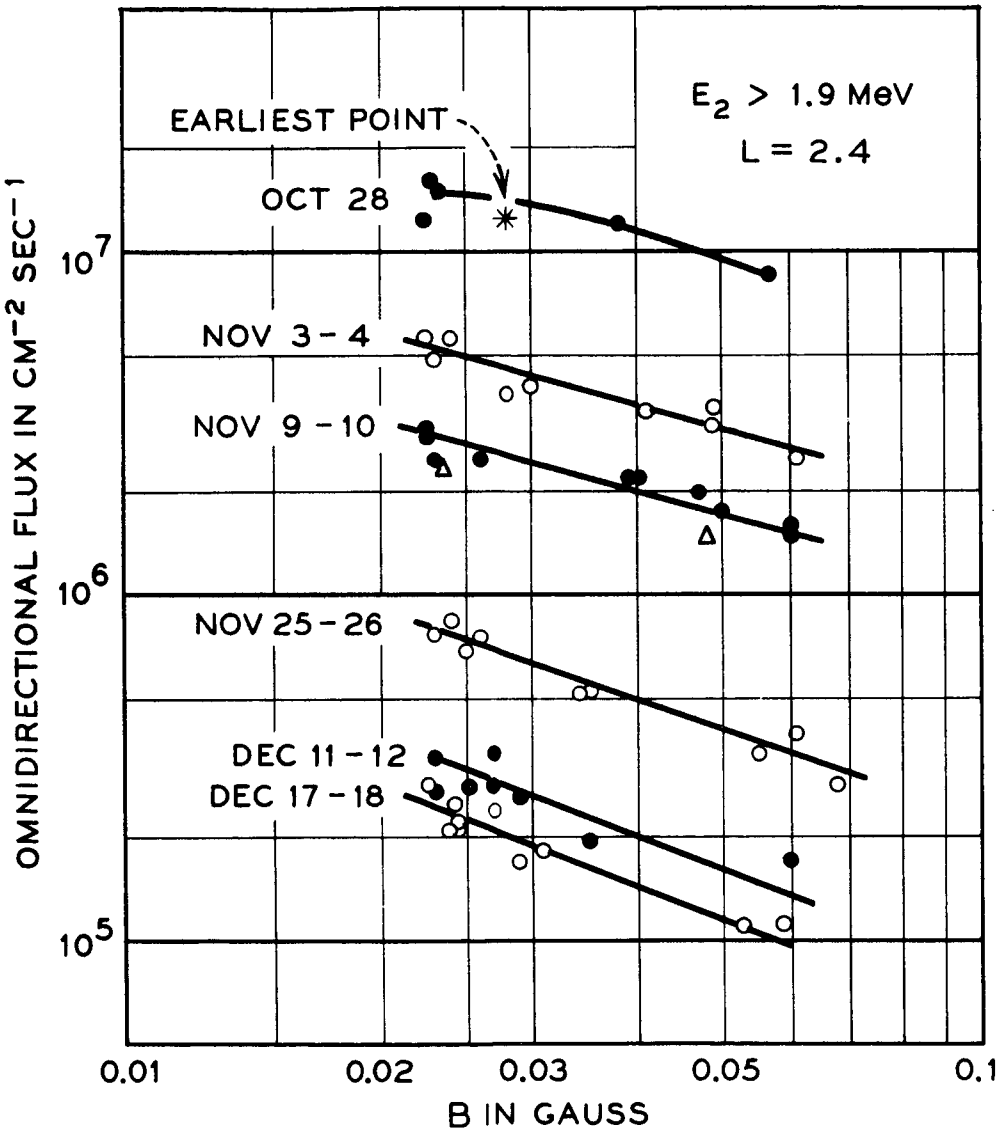
EARLIEST POINT
$E_2 > 1.9$ MeV
L = 2.4
OCT 28
NOV 3 - 4
NOV 9 - 10
NOV 25 - 26
DEC 11 - 12
DEC 17 - 18
10^7
10^6
10^5
OMNIDIRECTIONAL FLUX IN CM^{-2} SEC^{-1}
0.01
0.02
0.03
0.05
0.1
B IN GAUSS

Fig 2-37

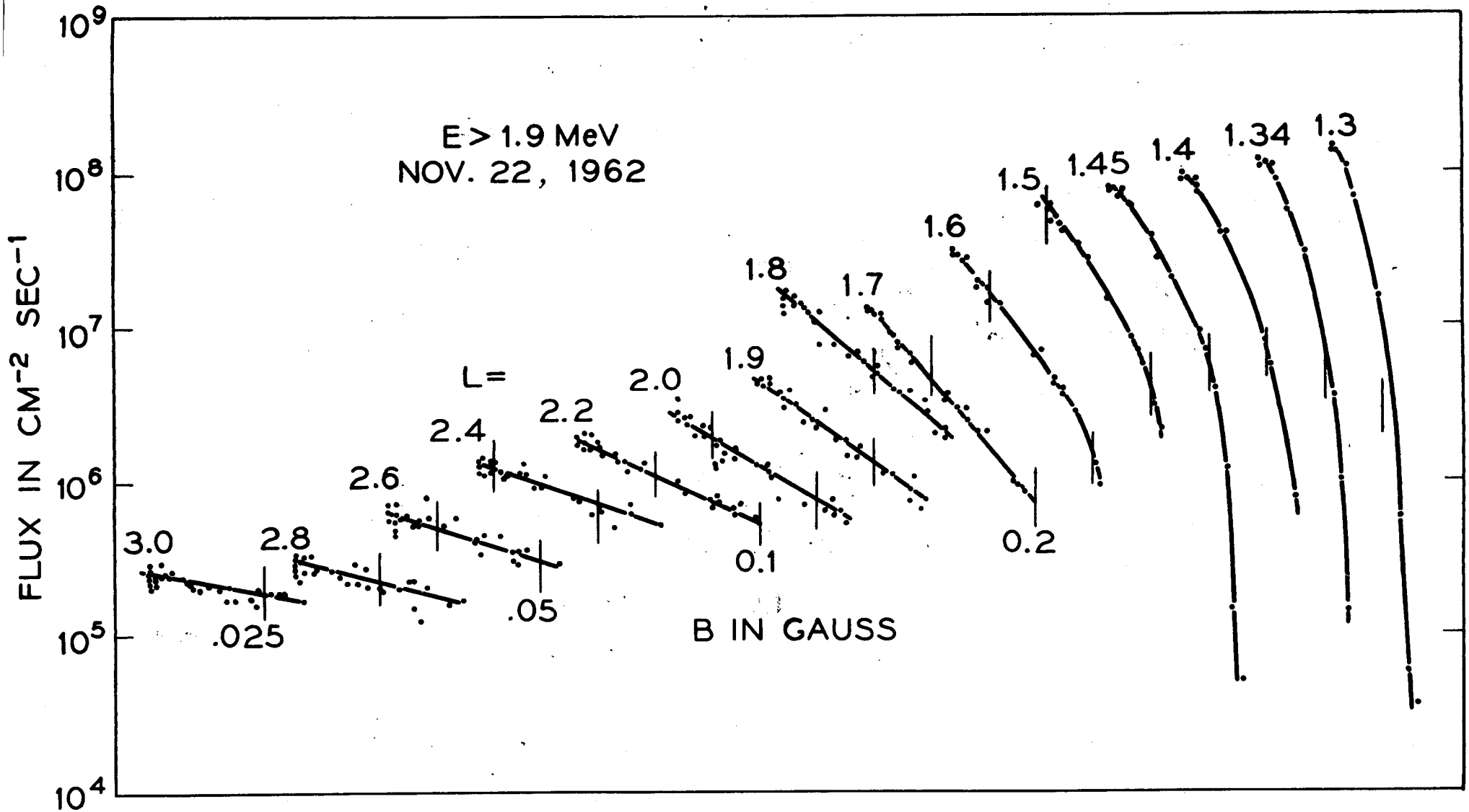
E > 1.9 MeV
NOV. 22, 1962
FLUX IN CM^{-2} SEC^{-1}
10^9
10^8
10^7
10^6
10^5
10^4
L=
3.0
2.8
2.6
2.4
2.2
2.0
1.9
1.8
1.7
1.6
1.5
1.45
1.4
1.34
1.3
.025
.05
0.1
0.2
B IN GAUSS

Fig. 2-38

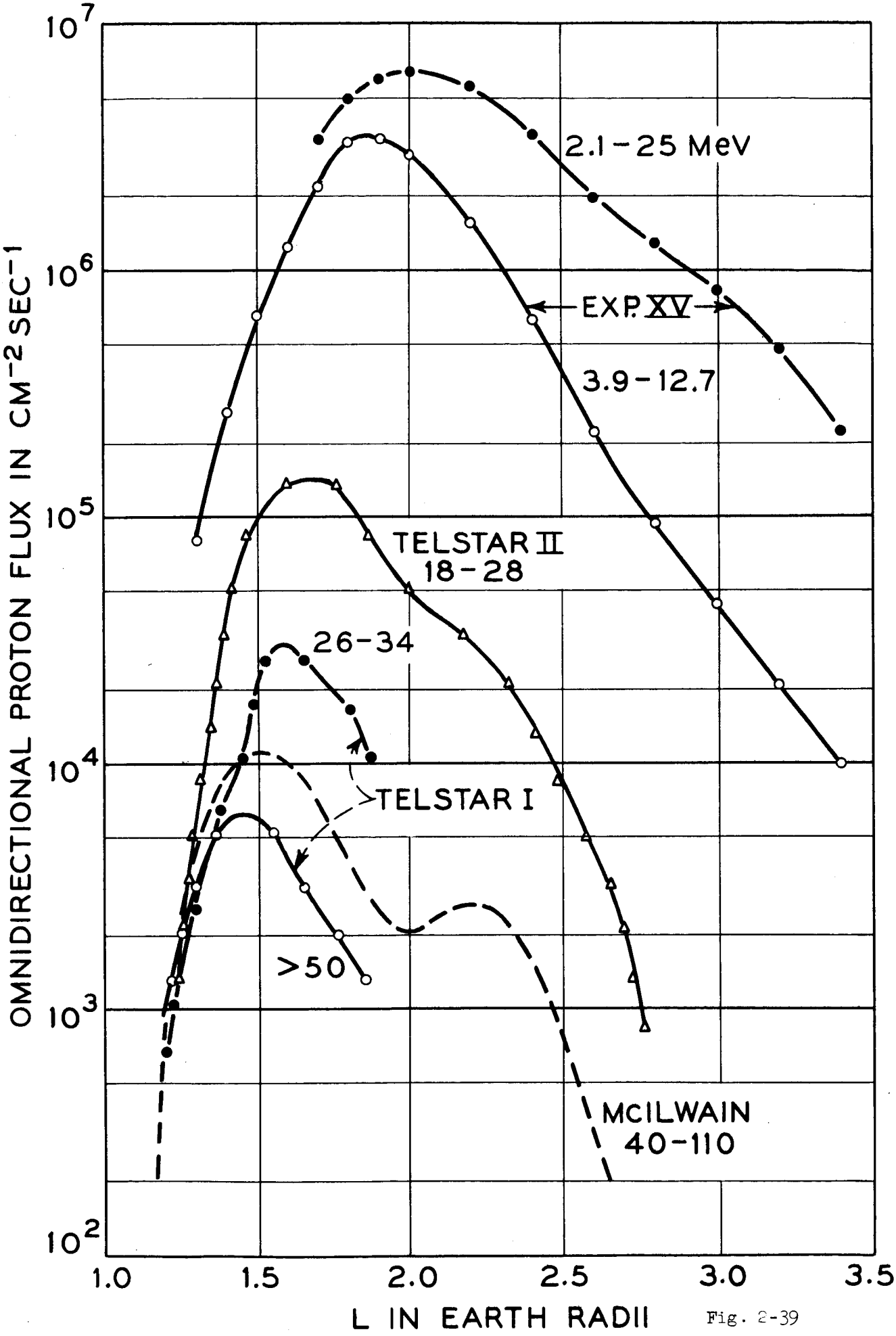
OMNIDIRECTIONAL PROTON FLUX IN CM^{-2} SEC^{-1}
10^7
10^6
10^5
10^4
10^3
10^2
2.1 – 25 MeV
EXP. XV
3.9 – 12.7
TELSTAR II
18 – 28
26 – 34
TELSTAR I
>50
McILWAIN
40 – 110
1.0
1.5
2.0
2.5
3.0
3.5
L IN EARTH RADII

Fig. 2-39

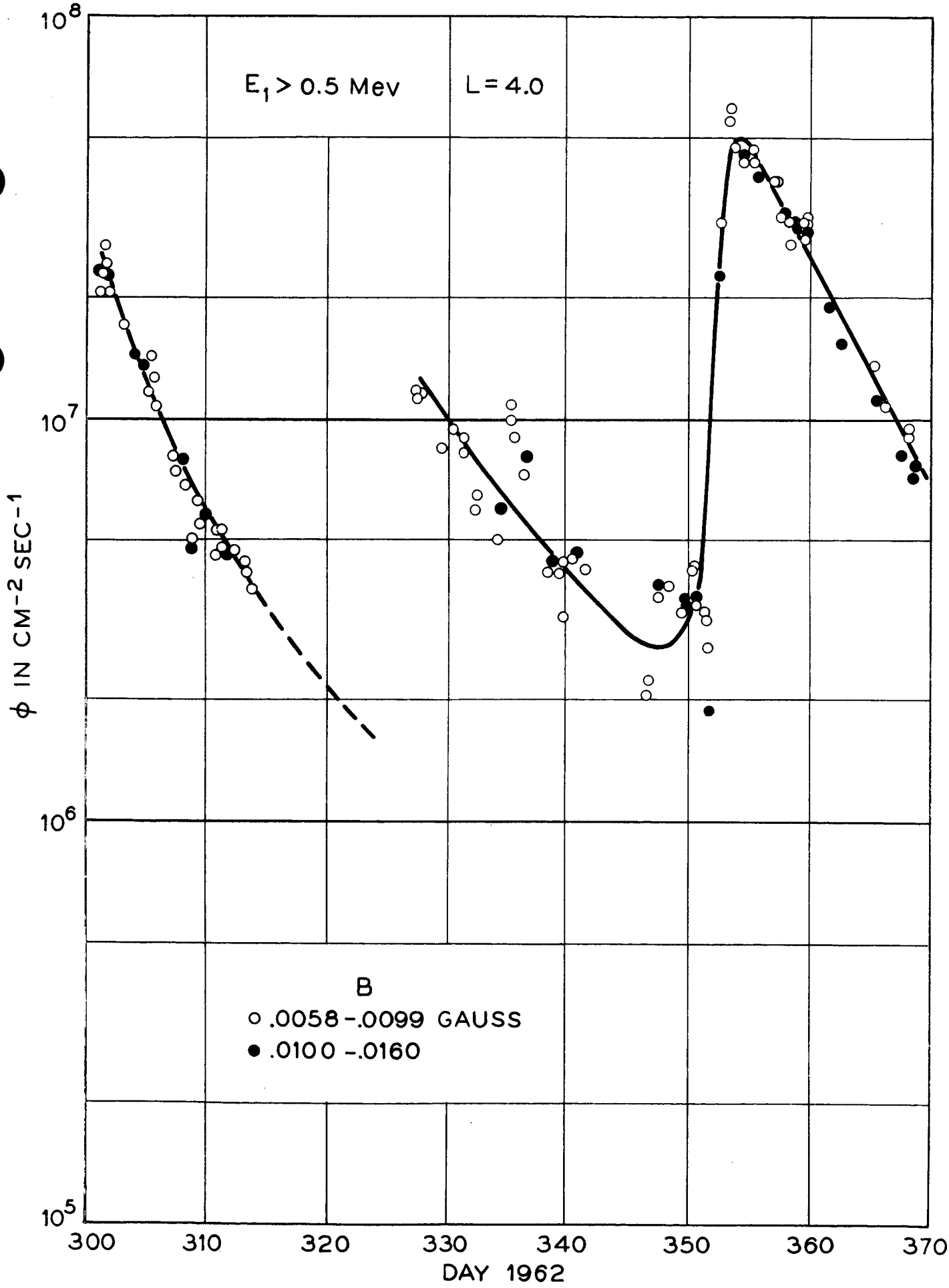
$E_1 > 0.5$ Mev
L = 4.0
10^8
10^7
10^6
10^5
ϕ IN CM^{-2} SEC^{-1}
B
○ .0058 -.0099 GAUSS
● .0100 -.0160
300
310
320
330
340
350
360
370
DAY 1962

Fig. 2-40

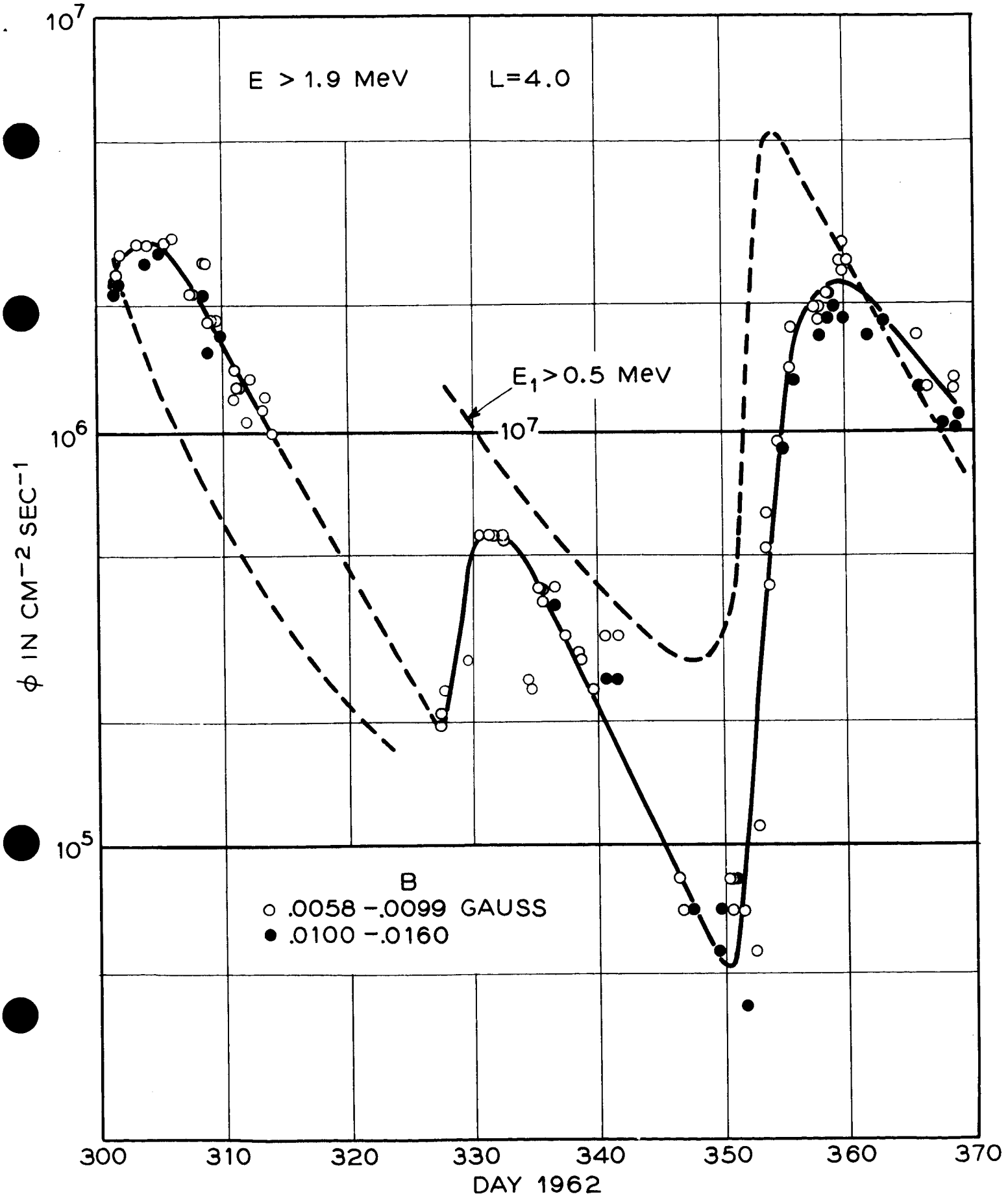
E > 1.9 MeV
L=4.0
E1 > 0.5 MeV
10^7
B
○ .0058 -.0099 GAUSS
● .0100 -.0160
φ IN CM^-2 SEC^-1
10^7
10^6
10^5
300
310
320
330
340
350
360
370
DAY 1962

Fig. 2-41

III. SOLAR CELL DAMAGE EXPERIMENT

3.1 Design of the Experiment

The solar cell damage experiment was designed to provide a measure of the integral radiation damage effects of the particles to which the satellite was exposed over a period of months in orbit. By use of different thicknesses of transparent shielding material over the solar cells, broad characteristics of the spectral composition of the incident flux can be determined. Damage experiments rarely provide a means of studying new phenomena because of the integral nature of their detection characteristics. However, they do provide an over-all check on a number of variables important to the solar cell power plant designer. It was with this intent that the damage experiment on Explorer XV was provided.

Because of extensive experience at Bell Laboratories with n-on-p type silicon solar cells as used in the Telstar solar power plant,[1] these were chosen for the Explorer XV experiment. Such cells had well-known spectral and electrical characteristics and could be provided in the limited time available for the design, construction and testing of the experiments for the SERB program. Furthermore, these cells had a well established absolute radiation damage sensitivity to electrons and protons of various energies and a demonstrated high uniformity among individual cells.[2,3] The characteristics of the devices are described in detail by Smith, et al.[1]

Radiation damage to solar cells can be measured through changes in the short circuit current of illuminated cells. Under short circuit conditions cell output is directly related to the incident light intensity and the effective collection depth (the diffusion length for hole-electron pairs created by the light). Such a measurement clearly does not provide a direct evaluation of deterioration of the complete junction V-I characteristic. However, except in cases where very heavy damage may be done just to the shallow junction region with a resultant extreme deterioration of the V-I characteristic,[4] the short circuit current measurement in space together with laboratory measurements of the associated changes in other characteristics of the cells provide the essential information. Extreme junction damage effects are only produced by low energy heavy charged particles, for example protons of about 1 Mev, and they cannot reach the cells under the shielding conditions of the present experiment.

It is convenient to measure the short circuit current in terms of a voltage developed across a load resistor. To stay in the short circuit region of the cell characteristic it is necessary in silicon solar cells at the temperatures under consideration to restrict this voltage to $<.2$ volts. The telemetry encoder of Explorer XV provided for 0-5 volt input signals with a resolution approximately one per cent of full scale. To provide a voltage high enough to take advantage of

the available accuracy, the experimental arrangement used 24 small solar cells in a series string. The use of a large number of cells has the additional advantage that it provides an average response which largely removes the effect of statistical differences in the damage sensitivity of individual cells. This arrangement must not be used with a single shunting resistor across the whole series string. In that case only the cell having the lowest short circuit current will operate in the short circuit range. The others will operate at higher voltages corresponding to points in the region of the knee of the V-I characteristics of the cells. Thus instead of measuring an average over the cells, one measures the short circuit current of only the poorest. Furthermore, this arrangement is sensitive to failure of a single cell in the string. Ideally each individual cell should be shunted by its own resistor, but due to limitations in the weight of the experiment the cells were shunted in pairs by 12 identical resistors in the string as shown in Fig. 3-1.

The size of the small solar cell elements was determined by mechanical considerations and by the availability of an adequate number of identical, well aged and highly reliable resistors.[5] The active area of the individual cells was a rectangle approximately 40 by 130 mils. Four strings of cells such as in Fig. 3-1, covered with different thicknesses of synthetic sapphire shielding, make up the damage experiment.

A thermistor provides an essential measurement of the temperature; this is needed for referring all data to a standard temperature. The total output of the experiment thus consists of five measurements, four solar cell short circuit currents, measured as voltages across 12-178 ohm (= 2136 ohms) resistors and one thermistor voltage. An important additional piece of information is provided by the solar aspect monitor which determines the orientation of the sun with respect to the satellite and thus to the solar cell damage experiment.

The sapphire shielding thicknesses for the cells were selected at 10, 30, 50, and 80 mils to span a very wide range, from the thinnest that could be handled reliably in the mechanical construction to one thicker than that of any shield yet seriously proposed for practical solar cell power plant design. These shields have mass thicknesses of .10, .30, .50, and .80 g/cm^2, and exclude protons below 7.4, 14, 19 and 25 Mev respectively. The solar cell string under the heaviest shield was expected to show little or no change due to radiation damage and thus to provide a measure of the illumination conditions of the whole experiment.

3.2 Construction and Testing

3.2.1 Mechanical Design and Construction

From the point of view of the solar power plant it was desired to launch Explorer XV so that the sun was originally about 150° from the spin axis of the satellite. The zero of

this angle, in the notation of the solar aspect measurement, is at the magnetometer end of the satellite. The solar aspect angle was expected to increase with time, initially by about one degree per day, until the sun was at 180° (on the negative spin axis) and then to decrease again in an approximately symmetrical manner. Thus the solar cell radiation damage experiment could not be located as on Explorer XII and XIV on the side of the octagonal base of the satellite looking perpendicular to the spin axis. It was instead mounted in two sections (each carrying two of the differently-shielded cell groups) 180° apart around the circular section of the satellite's lower structure with the solar cells facing nominally along the negative spin axis. One of the mounted sections is visible in the photograph of Fig. 3-2. For solar aspect angles of less than 140° the cone structure housing the satellite telemetry transmitter provides shadowing of the experiment during part of the rotation of the satellite. A close-up of the pair of experimental assemblies is shown in the photograph of Fig. 3-3. The elements of this assembly will be discussed in more detail in the sections to follow.

3.2.1.1 Solar cell Module

The 24 small solar cells in each part of the damage experiment are assembled in three modules. Each module consists of a Coor's AD-94 ceramic plate, eight solar cells and four resistors, Fig. 3-4. The ceramic plate provides the

mounting surface for the other components. Coor's AD-94 ceramic is used because of its high electrical resistance, mechanical strength and good thermal conductivity and relatively good match to silicon in thermal expansion coefficient. The solar cells are soldered together in pairs with two nilvar ribbons providing the electrical connections. These assemblies are then aligned and bonded to the ceramic plate which has previously had the four resistors and preformed leads bonded to the lower surface. The bonding of all componenets to the plate is achieved with epoxy resin. After the epoxy is cured in an air oven at 60°C the electrical connections between the solar cells and resistors are soldered. Epoxy is then applied over the resistor leads and contact ribbons. One module in the group of three is equipped for temperature monitoring and has a thermistor bonded between the middle two resistors. In order to provide good thermal conduction between the ceramic plate and the aluminum housing which holds it, the ceramic is metallized on its edges with Hanovia Silver prior to assembly of the solar cells and resistors. The metallizing is gold plated to reduce any oxide formation prior to final assembly.

3.2.1.2 The Base Housing

The structural design of this detail is determined by two main considerations. First it is the mechanical support, back radiation shield and heat conductor for the solar cell

modules and second, it is a structural element when fastened to the satellite skin. In order to satisfy the conditions thus imposed, the support base is machined from aluminum stock with provisions for two groups of modules as shown in the mechanical drawing of the assembly, Fig. 3-5. To distribute the loading on the satellite skin during the rocket launch, extension legs are machined as an integral part of the base. A total of eight screws are used to fasten the detector to the satellite. Electrical connections between each module and to the satellite are provided by channels machined between each section and terminals staked into the bottom of the base.

To prevent the detectors from operating at too high a temperature (above 60°C) all external surfaces of the aluminum housing block and of the cover to be described in the next section are coated with white aluminum oxide. This coating is applied with a plasma spray gun. The high emissivity of this coating lowers the operating temperature very significantly as will be seen in Section 3.2.4.

3.2.1.3 The Cover Assembly and Springs

The cover assembly consists of an aluminum frame in which sapphire plates are supported by platinum channels, Fig. 3-6. Two of these assemblies fit on each of the housing structures of Section 3.2.1.2. The covers are designed so that only one detail is changed to accept the four different sets of sapphire plates (10,30,50,80 mils thick). Besides

providing mechanical support for the platinum channels, the aluminum frame acts as a retainer for the solar cell modules when fastened with screws to the base housing. To insure uniform loading on the modules, flat molybdenum springs are placed between the aluminum housing and cover assembly. The springs hold the modules in position and allow for thermal expansion. Figure 3-7 is an enlarged cross section through the assembly to show the details. The sapphire plates are bonded to the platinum channels with epoxy resin. Platinum is used in conjunction with the sapphire to match the thermal expansion characteristics. This method of support of the covers avoids the problem of glue in the optical path and thus the potential problem of discoloration and optical loss due to radiation in space.

3.2.2 Acceptance Angle of Illumination

With the desired launch aspect of the satellite placing the sun 30° off the normal to the solar cell damage experiment, the detectors were designed to have minimum illumination angles of 40° uncorrected for refraction. These angles are illustrated in Fig. 3-8 as seen in the same plane as Fig. 3-7 which cuts across the smaller dimension of a mounted module. The angles are determined by limiting lines touching the edges of the platinum channel and the outer edges of the two small solar cells at points A. When these angles are corrected for the refraction which takes place as light

passes through the thickness of the sapphire plates the limiting angles change to the values shown in the table below.

TABLE 3-1

Sapphire Thickness	Acceptance Angle	
	Uncorrected for Refraction	Corrected for Refraction
10 mils	57°	58°
30	55°	65°
50	47°	62°
80	38°	55°

Limiting angles in a plane at right angles to the plane of Fig. 3-9 arise in the end pair of cells in the array of eight on a module. The smallest of these limiting angles is 47° for the 10 mil sapphire case. Thus as long as the angle of illumination is no more than 47° from the normal to the array (the solar aspect angle is >133°) there will be no shadowing of the solar cells by their own mounting structure.

3.2.3 Vibration Tests

In order to prove the mechanical design and fabrication scheme of the detectors, sinusoidal vibration tests were performed on the prototype model at BTL, Murray Hill. The acceleration levels of these tests were more severe than those required for qualification but the vibration machine was limited to frequencies below 2 kc. Figure 3-9 compares a typical test data run with NASA qualification specifications. The detectors

for the satellites S3B and S3C were tested at acceptance levels by NASA at Goddard Space Flight Center. The prototype detector showed no evidence of any mechanical or electrical failure after the vibration tests at the qualification levels and the detectors tested by NASA as flight units also successfully passed all vibration tests.

3.2.4 Thermal Tests

Two radiation damage detectors were tested on the prototype satellite at Goddard Space Flight Center. The tests were performed in a thermal vacuum chamber using arc lamps calibrated for one solar constant. The two detectors were the same except that one was not coated with aluminum oxide. Thermistors were bonded to the aluminum housing and to a solar cell module in each detector. Figure 3-10 shows the temperature of the detectors as a function of time. The temperature variation during the test was caused by fluctuation of the light intensity. The average temperature of the aluminum oxide coated unit was about 12° less than the average temperature of the uncoated assembly. It is interesting to note that the thermal coupling of the solar cell module to the aluminum housing is very good, the temperature difference being only one to two degrees throughout the test. Careful inspection and electrical testing before and after the thermal test showed that there was no mechanical failure of any part and that the voltage output of the modules did not change.

3.3 Solar Cell Selection and Testing

The solar cells used in the construction of the radiation damage detectors were selected from a group of 800 1 cm×2 cm n on p-type cells from a single fabrication run. They had nominal base resistivity of one ohm centimeter and an n-type diffusion depth of approximately 0.5 micron.[1] The devices were first screened to remove occasional cells showing nonlinear effects. This was done by comparing the measured response (the short circuit current) of each cell under white light illumination (a tungsten spectrum with heat absorbing glass) with the response computed from measurements of the short circuit current under illumination through optical bandpass filters. This method is discussed by Gummel and Smits.[6] The cells were then selected for uniformity in predicted outer space short circuit current. The group of cells used were within ±5%. The cells were then grouped within this range into classes which were uniform to ±2% or better.

The small cells mounted in modules (Section 3.2.1.1) were cut from the cells of this doubly selected and ordered group above. Four small cells were cut from the contact stripe edge of each 1×2 cell. Thus each small cell has a full width contact stripe along one of its long edges. The eight small cells needed for a module were obtained from a chosen pair of 1×2 cells. After module fabrication the cell response was measured again under illumination through bandpass filters.

The voltage across the modules now indicates the short circuit current in a string of eight cells with their associated resistors. It varied by as much as 5% from that expected from the measurements of the 1x2 cells. This is probably due partly to variability over the area of the original cells. It is more importantly due to inaccuracy in cutting (severe in this small size) and to variations in the width of the contact stripe which now is more than half the width of the small cell. From the final measurements on the assembled modules, four groups of three modules were selected to make up the detectors in the two assemblies of a complete experiment. Figure 3-11 and 3-12 give the module designation and layout of the assemblies which flew on Explorer XV.

Table 3-2 gives the predicted voltages expected in outer space at mean solar distance, at 30°C, and under normal incidence on the basis of the bandpass filter measurements of the spectral characteristics of the individual modules in each set.

TABLE 3-2

Shield Thickness	10 mil	30 mil	50 mil	80 mil
Module	A12,B8,A5	A8,B12,A2	A1,B9,A10	A3,B4,A11
(1) Vos (no sapphire)	2.98	2.95	2.94	2.99
(2) Vos (with sapphire)	2.60	2.58	2.58	2.62
(3) Vobserved (30°C ⊥, $\overline{\odot}$)	2.59	2.64	2.43	2.57

The module measurements were made with no sapphire covers over the cells and line 1 in Table 3-2 is the prediction for bare cells in space. Line 2 will be discussed in the paragraph to follow, and line 3 in Section 3.6.1.

The optical losses introduced by sapphire shielding covers are substantial. Figure 3-13 shows these for the four shielding thicknesses. The 80 mil shield is actually formed of two 40 mil pieces cemented together with epoxy cement since it was not possible to obtain thick enough material of satisfactory quality in time. The losses are seen to be essentially independent of sapphire thickness. They are reflection losses at the two sapphire-air interfaces. The primary spectral contributions to the solar cell response are in the .5 to .8 micron wavelength region. The approximate weighted average of the losses from Fig. 3-13 is 12.5%. Line 2 of Table 3-2 is the result of correcting line 1 by this amount.

Properly prepared sapphire shows less than 2% absorption loss as a result of radiation by ultraviolet light or ionizing particle radiation in doses to be expected after years in space. Not all sapphire has this property, however. Some material procured for thick shields on Explorer XV did not have a final annealing step by the manufacturer. It showed color center formation with absorption of as much as 15 to 20% in important regions of the solar spectrum after relatively modest radiation doses. The only solution in the available time was to epoxy thinner pieces together to get the requisite optical clarity in the 80 mil absorber. The epoxy was radiation tested and showed no measurable discoloration.

3.4 Results form Space

3.4.1 Data from the First Days in Orbit

Figure 3-14 shows data for the 10 mil sapphire covered cells on October 28, 1962, the first day in orbit. The ordinate is the comb filter number which specifies the frequency number of the voltage controlled oscillator reading the voltage of this set of cells. (The four cell groups occupy PP3, 4, 5 and 6 of the 16 channal performance parameter subcommutator.) A high reading corresponds to a low output from the cells. The abscissa of the figure is time measured in units of 48 telemetry frame periods. A measurement of PP3 is made once each 16 frames, approximately once each 4.66 seconds. Successive readings of PP3 vary widely, because the frame time of the telemetry encoder and the period of satellite spin are not synchronous. The readings of PP3 occur at different rotational positions of the satellite. There will always be some number of spin periods which comes arbitrarily close to matching a whole number of frame times and on such a time scale the successive readings will shift slowly (or in the limit, not at all). This correspondence occurs fortuitously in the case of Explorer XV at three 16 frame periods and 17 satellite rotations. In Fig. 3-14 just these points are plotted, that is, every third reading of PP3. The pattern produced shows that this choice is not quite synchronous by a very convenient amount. Between readings the phase advances about 5.6° so that in 64 readings the measurements have scanned completely through the satellite rotation.

The shape of Fig. 3-14 arises from two main factors. The large peaks at the beginning and end of the time record are caused by shadowing of the experiment by the mounting ring on the end of the transmitter housing. The initial solar aspect was approximately 130°, and as indicated in Section 3.2.1 shadowing will occur unless the angle is greater than 140°. The remainder of the variation in Fig. 3-14 is due to the shingled mounting of the small solar cells in their modules (Fig. 3-7). If the cells were mounted flat, the sun would always see them at the same angle, independent of the rotation of the satellite. (The angle of incidence of sunlight on the sapphire covers <u>is</u> independent of rotation.) However the shingling introduces an asymmetry. Define the effective angle of shingling as δ, the angle between the negative spin axis and the normal to the cells, the solar aspect angle as α, and the rotational angle of the experiment with respect to a plane through the satellite spin axis and the satellite sun line as ψ, Fig. 3-15. As the satellite rotates and ψ goes from 0 to 2π the sun is incident at a changing angle α' with respect to the normal of the <u>cells</u>. The relationship is given by Eq. 3.1.

$$\cos \alpha' = \cos(\pi-\alpha)\cos \delta - \sin(\pi-\alpha)\sin \delta \sin \Psi \qquad (3.1)$$

where Ψ is measured clockwise from the defining plane as viewed from the telemetry transmitter end of the satellite and the signs are correct for the actual mounting with δ a positive angle (approximately 10°).

At $\Psi = 0, \pi$

$$\cos \alpha' = \cos(\pi-\alpha)\cos \delta$$

At $\Psi = \pi/2$

$$\cos \alpha' = \cos(\pi-\alpha)\cos \delta - \sin(\pi-\alpha)\sin \delta$$
$$= \cos[(\pi-\alpha) + \delta]$$

At $\Psi = 3\pi/2$

$$\cos \alpha' = \cos(\pi-\alpha)\cos \delta + \sin(\pi-\alpha)\sin$$
$$= \cos[(\pi-\alpha) - \delta]$$

The cell output response is a monotonic function of $\cos \alpha'$ and as a result the maximum response is seen from Eq. 3.1 to occur for $\Psi = 3\pi/2$, the minimum for $\Psi = \pi/2$ and intermediate values for $\Psi = 0$, and π. In Fig. 3-14 $\Psi = \pi$ is in shadow. At $\Psi = \pi/2$ the reading is approximately 82 (a high comb filter reading corresponds to a low output voltage) and at $\Psi = 3\pi/2$, approximately 70. The value at $\Psi = 0$ is not directly identifiable but it must lie almost at the average of the two extreme values for $\Psi = \pi/2$ and $3\pi/2$. In the region of the extreme values, between 15 and 35 and 44 and 57 on the time scale of Fig. 3-14 there are variations of one comb filter number on what is expected to be a constant response. This "noise" occurs at the limit of resolution of the encoder system.

Knowing the values of α and δ, the angle α' of incidence of direct sunlight on the cell array can be determined for both extreme regions of Fig. 3-14. Knowing the functional dependence of cell output on α', the value for the cell output under conditions of normal incidence can be deduced from either or both of the observed extreme values. Such derived values of normal incidence output, further corrected for temperature and mean solar distance, as will be discussed in Section 3.5, form the basis for evaluating damage effects to the solar cells in space.

The strobing effect of the telemetry measurements through the rotation of the satellite provides a way of deducing the spin rate to a very high degree of accuracy if it is even crudely known from other measurements. Such information is incidental to the main purpose of the solar cell damage experiment and will be mentioned only briefly here. First note that since three 16-frame periods are almost synchronous with the satellite, in one 16-frame period the satellite must rotate a whole number of rotations $\pm \frac{1}{3}$. From the nominal 73 revolution per minute spin rate, the satellite is computed to rotate $5\frac{2}{3}$ revolutions in 16 telemetry frame times. The accuracy of the nominal value of the spin rate only needs to be sufficient to distinguish $5\frac{2}{3}$ revolutions from $6\frac{1}{3}$. Now in 48 frames (three 16-frame groups) the satellite will rotate approximately 17 times. It fails to do this by

1/64 of a revolution since in 64 of the 48-frame intervals the strobing effect goes through one full rotation. Because of the asymmetry produced by the shadowing, the direction of rotation in the strobing can be deduced to be the same as the direction of the rotation of the satellite itself. Thus in the 64 time groups the satellite has rotated a total of $17 \times 64 + 1 = 1089$ times. The accuracy of this determination is better than $\pm 1/64$ of a revolution. The total time span for these rotations is 895.31 seconds according to the ground station time record and thus the spin rate is found to be $1.21633 \pm .00002$ revolution per second. This determination is capable of about another factor of 5 increase in accuracy by proper evaluation of the fraction of a 48-frame interval in which the rotation observed in the strobing is complete.

Figure 3-16 shows a set of results for the sixth day in orbit, on November 2. The pattern is very much the same as for the first day in Fig. 3-14. The minimum comb filter number has dropped by about one and the maximum, aside from the shadow peak, by two or three. These observations assert that the solar cells of PP3 (10 mil sapphire covers) are producing a larger output than before. This is associated with an increase in the solar aspect angle and thus a decrease in the angle α' to the normal of the cells. The length of the shadow interval has dropped very substantially, again as a result of the solar aspect angle change. The period of

strobing around the satellite with the 48-frame intervals has dropped from 64 in Fig. 3-14 to 48 in Fig. 3-16. This can be due to a decrease in the rotational period of the satellite (an increase in spin rate) or to a decrease in the telemetry frame time. The shift from the results of Fig. 3-14 amounts to a change in one or the other or a combination of about 30 parts in 10^5.

The values of the solar aspect angle of Explorer XV as determined by EMR are plotted in the upper part of Fig. 3-17. The solar aspect angle slowly increases from the beginning and exceeds 140° at about day 10. It does not quite reach 180° at its extreme which is attained in mid-December after about 45 to 50 days in orbit. The temperature of the solar cell damage experiment is plotted in the lower half of the figure, also as extracted and converted from the data by EMR.

3.4.2 Data for Later Times

The upper part of Fig. 3-18 is a sample of the data for the 14th day in orbit. The spike of shading is now gone as expected because α exceeds 140°. The curve is essentially symmetric as the angle of illumination α' of the individual cells approaches toward or recedes from one of the extrema. The voltage output of the cell group is higher than in Fig. 3-14 or 3-16 because the illumination is more nearly normal to the cells.

The lower part of Fig. 3-18 is data for the 41st day in orbit. According to Fig. 3-17, α is nearly 180°. At 180° the cells would have no way of recognizing that the satellite is rotating and the time variation of the cell output must go to zero. This is almost the case on the 41st day, and the angle of illumination of the shingled cells is now nearly the angle δ. The fact that periodic variations still exist however, demonstrates that α is not quite 180°.

3.5 Treatment of the Data

3.5.1 Statistical Distribution of Solar Cell Outputs

In Figs. 3-14,-16,-18 typical sets of data for the output of the 10 mil sapphire shielded cells have been shown. These represent a very small fraction of the total data that exists. There are similar sets of data for the other three shielding thicknesses. In addition, in the plot only every third data point was displayed to illustrate the shape of the response as directly as possible. Finally, each plot spans a time of about 1000 seconds, or about 1% of a day. There are altogether about 5×10^6 pieces of solar cell damage data from the approximately 90 days of telemetry reception from Explorer XV in space. There is no point in carrying out an analysis of all this data because of the slow variation of solar cell output with time. However, to include a much larger sample in the analysis than is possible by examining thousands of plots, a statistical approach has been devised. Of greatest

interest is the solar cell output for angle ψ near $\pi/2$ and $3\pi/2$ (Eq. 3.1) because these are most directly determined. Since these occur as extrema in cos α' they will be visible in a statistical distribution of a group of comb filter readings. The first four columns of Table 3-3 show such a distribution for the first day in orbit. The fractional occurrence of each comb filter number is displayed for a pass containing several thousand data points. The distributions for all four of the sets of cells with different shielding covers are shown as obtained from data of PP3, 4, 5 and 6. In the PP3 column the data of the distribution include that shown in Fig. 3-14. There is a peak in the distribution at comb filter number 70, 24.5% of the measured points falling at that value. This is the value of the minimum seen in Fig. 3-14 and corresponds to $\psi \simeq 3\pi/2$. A second maximum in probability-of-occurrence is seen at comb filter number 82, corresponding to $\psi \simeq \pi/2$. There is a third peak at comb filter number 105 for the points measured in the shadow. Similar features are apparent in the distributions of PP4, 5 and 6. The second group of four columns in Table 3-3 shows the distribution of the probability-of-occurrence for the 14th day in orbit. The shape of this distribution is that to be expected from results such as are plotted in Figs. 3-18 from PP3 on that day. The shadow peak of comb filter number 105 is gone. Some 26% of the data fall in comb filter number 65, 13% in number 74. The third group of four columns in Table 3-3

show the very restricted distribution observed on the 50th day in orbit. The sun is nearly on the negative spin axis and the modulation of the cell output due to the shingling has almost disappeared.

Values of maximum and minimum readings of the damage experiment outputs have been determined from distributions like those of Table 3-3. These are then corrected for angle of incidence, temperature and mean solar distance as discussed in the three sections to follow.

3.5.2 Angle Corrections

Figure 3-19 shows the angular variation in the output of a cell covered with 30 mils of sapphire as a function of the angle of incidence with respect to the normal.[8] For small angles the variation goes nearly as the cosine of the angle of incidence, but for larger angles the output falls more rapidly because of increasing reflection losses at the sapphire surfaces. This curve has been used to convert the outputs of the cells as measured at various angles α' (Eq. 3.1) to the equivalent output to be expected at normal incidence.

3.5.3 Temperature Correction

It was shown in Fig. 3-17 that the temperature varied over the period of the experiment between about 40 and 62°C. All solar cell output results have been corrected to a standard temperature of 30°C. In the undamaged cells the temperature dependence as shown in Curve A of

Fig. 3-20 is essentially linear over a wide range and has a slope of approximately .07%/°C. At the highest temperature the correction amounts to approximately 2.5%.

Figure 3-20 also shows in curve B the temperature dependence of very heavily damaged solar cells. The steeper slope is attributable to the characteristics of deep lying radiation-produced recombination centers which now limit the carrier diffusion length. The transition from an undamaged to a damaged temperature coefficient depends in a complex way on the extent of the damage (and probably on the details of the defects radiation is creating in the material). Since the extent of the damage in these experiments is quite small the undamaged temperature coefficient has been used exclusively.

3.5.4 Mean Solar Distance

Figure 3-21 shows the annual variation in the solar intensity at the earth as a result of changes in the earth-sun distance. The intensity is an a maximum in early January and a minimum in July with a peak deviation from the mean of 3.3%.

3.6 Final Results

3.6.1 Absolute Initial Output of the Cells in Space

Obtaining a value for the absolute output from the solar cells in space under standard conditions requires making the three corrections of Section 3.5 in addition to carrying out conversions of the telemetry comb filter readings to voltages for the solar cells and to temperatures for the

thermistor on the experiment. It is interesting to compare the absolute values observed just after launch with the predicted values discussed in Section 3.3. The third line of Table 3-1 gives the values for corrected observations during the first day in orbit. The comparison is quite good with line 2 of the table, although the 6% difference in the 50 mil shielded case is a larger difference than can be accounted for by the uncertainty of the measurements. A loss of 8% would be expected if one cell in the 24 cell string developed an open circuit during launch. This may be the explanation.

3.6.2 Variation of Output with Time in Orbit

Figure 3-22 summarizes the results over 80 days in orbit. The output voltage, corrected to normal incidence, 30°C and mean solar distance is plotted against time for each of the four shielding thicknesses. The influence of one unit change in the comb filter number is shown by the small vertical bar. The last portion of the figure is a replot of the curve of illumination angle from Fig. 3-17, shown in the present case as $\pi - \alpha$.

All four cell groups show a decrease with time. The greatest change is about 20% in 80 days in the 20 mil sapphire case, the smallest about 13% in the 30 mil sapphire case. The most surprising thing about these results is the small difference there is among them and the lack of correlation there is with the shielding thickness. There is a substantial amount of scatter in the plotted points and the over-all effects are

not very large. Nevertheless the changes are quite significant. An order of magnitude difference is expected between the 10 mil and 80 mil covered sets as will be discussed in more detail in Section 3.6.3. The pronounced departure of the results in the 10 mil sapphire case in the region between 35 and 60 days in orbit is due to reflections from the platinum support pieces for the sapphire windows, see Figs. 3-7 and 3-8. As the angle of illumination becomes small, light is reflected from the sloping edges of the platinum supports as shown in Fig. 3-23. For the thicker sapphire windows the length of the sloping platinum surface decreases and the length of the horizontal surface increases so that the reflected light has a decreasing possibility of reaching the cells. In the 80 mil sapphire case there is no sloping surface, the top platinum support is flat and thus cannot give rise to such an effect. The data of Fig. 3-22 are in agreement with these geometric differences. There is no departure of the 80 mil sapphire points from the smooth decrease with time and if there is a departure for the 50 and 30 mil cases it is hardly discernible. The effect is restricted to illumination angles of approximately 15° or less. It is in just this region that the 10 mil sapphire-covered cells show their anomalous response.

The treatment of the data and the corrections made to it, and possible experimental antifacts that could produce the results of Fig. 3-22 have been examined in detail.

Some of these are discussed below. The results however say there has been a loss of output of the solar cells, showing no simple correlation with the shielding thickness of sapphire covers. This loss may be due to a change in the cells and it may also be due to a change in the amount of light reaching the cells.

Data processing involved in producing the distribution-of-occurrence of particular comb filter numbers is very straightforward, and the distributions appear to reproduce the response vs time curves such as Figs. 3-14, 16 and 18 faithfully.

The conversion from comb filter number to voltage involves the calibration of the voltage controlled oscillator in the satellite. If this oscillator drifted it could give the major changes observed. However, the same oscillator which was attached to PP3, 4, 5 and 6 of the solar cell damage experiment for four out of sixteen frames during word 15 of the telemetry was attached to other channels as well at other times in the telemetry sequency and showed no signs of a drift in characteristics.

Temperature corrections applied to the data are relatively small and are the same for all cells under the very good assumption that the cell temperatures are nearly alike. After 10 days in orbit the temperature corrections applied are constant to within 1% because temperature changes beyond that time are less than 13°. If a larger temperature coefficient is needed for the cells being damaged (Section 3.5.2) it would increase the apparent rate of damage slightly for all the cells.

The angle corrections for much of the data are the order of 10% and it is unlikely that they introduce errors of as much as a few per cent. The comparison of the initial value of cell outputs in space with the laboratory predictions has required an angular correction of about 30% for the large initial angles of illumination. The good correspondence obtained adds confidence to the other smaller angular corrections. Even more important, there is a very substantial overlap of data from times before and after the time of minimum illumination angle. Such measurements cannot be in relative error because of poor angular corrections. In Fig. 3-22 the straight lines have been drawn through those parts of the data most widely separated in time and having the same range of illumination angle. There is no question but that the results show a definite decrease with time in all cases.

A decay of all solar cell outputs could be produced by a downward drift in the value of the resistors that are shunting cell pairs on the modules (Fig. 3-1 and 3-4). The resistors used in the fabrication have been carefully screened with overload, aging and high temperature tests. Over a period of months in vacuum they tend to shift upward in resistance by the order of 0.5%. If the present results are to be explained by resistance instability, the resistors all drift downward in resistance by about 15%. Such an explanation does not seem possible.

The results could be explained if the sapphire cover glass degraded in transparency due to color center formation under ultraviolet and ionizing particle radiation is space. However, as mentioned in Section 3.3 the sapphire used was preirradiated with gamma rays to check for this potential difficulty.

A light absorbing deposit might build up on the under side of the sapphire or on the cell surface from decomposition of evaporation products from the epoxy used as cement in a number of places in the fabrication. There is no evidence for this in tests carried out to check this specific point under extended ultraviolet illumination of a completed unit in vacuum and at temperatures well above 60°C.

Reflection contributions to the light striking the solar cell cannot produce the differences between late and early times at the same primary angle of illumination.

None of these possibilities seem at all likely to account for the results observed.

3.6.2 Discussion

The results of Fig. 3-22 can be examined both for the damage dependence on shielding thickness and for the absolute amount of damage in comparison with the particle exposure of the satellite. In Fig. 3-24 the rates of decrease of short circuit current for the 10, 50, and 80 mil shielded experiments are plotted relative to the rate for the 30 mil shielded case. These points are compared in the figure with the thickness variation of damage due to an exponential electron

spectrum with an e-folding energy of 1.2 Mev. The curve is computed from laboratory measurements with monoenergetic electrons.[9] The average electron exposure of Explorer XV is to a spectrum no harder than this exponential spectrum, which approximates the beta spectrum of electrons from fission for the first few Mev and is richer in higher energy electrons than the fission spectrum.[10] The electron curve in Fig. 3-24 is thus as slowly decreasing with shielding thickness as damage due to electrons in the Explorer XV orbit can reasonably be.

A curve of the expected damage dependence on shield thickness for protons is also included in Fig. 3-24. This is computed on the basis of laboratory measurements of diffusion length degradation due to monoenergetic protons of energies between 1.35 and 130 Mev.[3] The spectrum chosen is somewhat harder than that observed by Telstar I[9] and II[11] for equatorial protons in the 18 to 50 Mev range. Since the 10 mil shielded cells are damaged by protons with energies as low as 7.5 Mev, the extrapolation of the measured spectrum to compute the damage under 10 mils of sapphire is somewhat uncertain. The number of protons in the extrapolated spectrum is not unreasonable, however, in comparison with still lower energy protons observed on Explorer XV. The computed curves of damage vs. shielding due to electrons and protons show at least an order of magnitude variation over the 10 to 80 mil shielding range. The observations from the experiment are

no more than a factor of 1.5. The results seem to be essentially unrelated to particle damage on the basis of this comparison.

The observed decrease in short circuit current for the 30 mil shielded cells is at a rate of approximately 8.5% in 50 days. This decrease is equivalent to the decrease that could have been produced by approximately 1.5×10^{14} 1 Mev electrons/cm^2 striking a bare cell at normal incidence. Thus the daily equivalent flux[9] is approximately $3 \times 10^{12}/cm^2$ day.

An equivalent flux can be computed from the particle exposure of the satellite and the damaging properties of the particles. The most severely damaging particles for the 30 mil shielded cells are protons with energies above 15 Mev. Using results for 18-28 Mev protons from Telstar II[11] and the spectrum assumed above (differential power law with exponent -4), the equivalent flux is between 1.5 and $2 \times 10^{12}/cm^2$ day. This takes account of the less than 2π exposure geometry because of the mounting of the cells in the detector blocks (see Fig. 3-8). The equivalent flux due to electrons is approximately $5 \times 10^{11}/cm^2$ day using the data of channel E2 and an exponential energy spectrum with a 1.2 Mev e-folding energy. Thus the total computed equivalent flux is between 2 and $2.5 \times 10^{12}/cm^2$ day. This is less than the observed damage although it is within the range of uncertainty of the measurements and the calculations.

One is in the peculiar position of having approximately enough particles to account for the damage at 30 mils shielding, not nearly enough to account for the damage at 50 and 80 mils, and too many to account for it at 10 mils. The damage equivalence

of protons has been established at room temperature and not between 50 and 60°C. It is quite possible that the computed figures are too high because of annealing and other rearrangement processes of the damage defects. It is also possibly high because of nonlinear effects.[3] It seems extremely unlikely that particles are producing the major share of the 30 mil damage observed.

An alternative explanation for the very weak dependence of the results on shielding thickness is surface roughening of the sapphire by micrometeorites. This would cause light scattering and a decrease in light intensity at the cells, independent of the sapphire thickness. Particles the order of 0.1 to to 1 μ in diameter would probably be most efficient in producing craters for light scattering in the 0.5 to 1 μ wavelength range. Smaller particles will produce craters too small and larger particles are probably too rare. Although no measurements of roughening of sapphire by high velocity dust particles have been made in connection with this work, it seems possible to estimate a very approximate flux of such particles which would have the observed effect. A 1 μ particle moving at orbital velocities will probably produce a crater several times the particle diameter (say 3μ) or having an area of $\sim 10^{-7}$ cm^2. If 50% of the incident light were diffusely scattered it would give approximately the current loss observed. This would require a number of impacts approaching $10^7/cm^2$ or $\sim 10^5/cm^2$ day. This exceeds

the conservative values of Whipple[12] by approximately a factor of a hundred. To avoid the contribution such particles would make to apparent damage in the Telstar power plant, they must be less numerous in the region of its orbit than in the orbit of Explorer XV. What seems to be required is an unusually high density of micrometeorite particles near the equator and possibly primarily above 3 earth radii. This hypothesis is not particularly attractive, but it competes rather favorably with the other alternatives.

TABLE 3-3

Comb Filter No.	Day 1 in Orbit				Day 14 in Orbit				Day 50 in Orbit			
	PP3	PP4	PP5	PP6	PP3	PP4	PP5	PP6	PP3	PP4	PP5	PP6
55	0	0	0	0	0	0	0	0	0	0	0	0
56	0	0	0	0	0	0	0	0	0	0	0	0
57	0	0	0	0	0	0	0	0	0	0	0	0
58	0	0	0	0	0	0	0	0	0	93.3	0	0
59	0	0	0	0	0	0	0	0	0	6.7	0	0
60	0	0	0	0	0	0	0	0	0	0	0	0
61	0	0	0	0	0	12.8	0	0	58.2	0	0	34.9
62	0	0	0	0	0	19.1	0	1.4	41.8	0	0	64.2
63	0	0	0	0	0	11.7	0	16.6	0	0	6.5	1.0
64	0	0	0	0	10.8	8.5	13.8	21.8	0	0	68.5	0
65	0	0	0	0	28.7	5.5	19.2	7.6	0	0	25.0	0
66	0	0	0	0	8.5	3.2	7.6	4.9	0	0	0	0
67	0	0	0	0	8.9	5.9	8.4	7.2	0	0	0	0
68	0	0	0	0	2.6	2.3	3.1	4.5	0	0	0	0
69	2.0	14.6	0	0	6.2	8.8	9.8	10.2	0	0	0	0
70	24.5	18.9	0	11.8	2.6	4.5	3.0	5.4	0	0	0	0
71	9.8	2.6	0	10.1	3.5	4.8	3.6	3.9	0	0	0	0
72	3.3	4.5	9.1	15.4	9.8	12.9	9.8	16.4	0	0	0	0
73	1.0	1.2	9.3	1.5	3.5	0	2.4	0.1	0	0	0	0
74	3.4	3.2	17.3	4.5	13.5	0	11.7	0	0	0	0	0
75	1.8	2.0	2.6	2.6	1.4	0	7.5	0	0	0	0	0
76	2.4	2.6	2.9	2.6	0	0	0.1	0	0	0	0	0
77	2.4	2.6	3.2	3.2	0	0	0	0	0	0	0	0
78	1.9	2.5	2.6	2.6	0	0	0	0	0	0	0	0
79	3.4	2.9	2.9	3.2	0	0	0	0	0	0	0	0
80	2.5	2.1	1.9	1.8	0	0	0	0	0	0	0	0
81	7.3	9.0	2.9	8.0	0	0	0	0	0	0	0	0
82	9.7	10.7	5.7	12.3	0	0	0	0	0	0	0	0
83	7 7	6.5	7.7	5.9	0	0	0	0	0	0	0	0
84	0.7	0.5	5.6	0.2	0	0	0	0	0	0	0	0
85	1.6	0.1	6.8	0.1	0	0	0	0	0	0	0	0
86	1.5	0.5	5.2	0.7	0	0	0	0	0	0	0	0
87	0.3	0.5	1.5	0.4	0	0	0	0	0	0	0	0
88	0.2	0.4	0.4	0.2	0	0	0	0	0	0	0	0
89	0.4	0.6	0	0.4	0	0	0	0	0	0	0	0
90	0.1	0.2	0.1	0.2	0	0	0	0	0	0	0	0
91	0.5	0.3	0.3	0.2	0	0	0	0	0	0	0	0
92	0.2	0.1	0.1	0.2	0	0	0	0	0	0	0	0
93	0.1	0	0.1	0.1	0	0	0	0	0	0	0	0
94	0	0	0.5	0	0	0	0	0	0	0	0	0
95	0.1	0	0.5	0.2	0	0	0	0	0	0	0	0
96	0.1	0.1	0.4	0.2	0	0	0	0	0	0	0	0
97	0.1	0.4	0.2	0.7	0	0	0	0	0	0	0	0
98	1.0	1.3	0.4	0.7	0	0	0	0	0	0	0	0
99	0.9	0.2	0.4	0.5	0	0	0	0	0	0	0	0
100	0	0	0	0	0	0	0	0	0	0	0	0
101	0.2	0.1	0.2	0.1	0	0	0	0	0	0	0	0
102	0.1	0.1	0.1	0.2	0	0	0	0	0	0	0	0
103	0.1	0	0.1	0.1	0	0	0	0	0	0	0	0
104	0.1	0	0.1	0.1	0	0	0	0	0	0	0	0
105	8.6	8.6	7.8	8.4	0	0	0	0	0	0	0	0
106	0.1	0.1	1.2	0.4	0	0	0	0	0	0	0	0
107	0.1	0	0	0	0	0	0	0	0	0	0	0
108	0	0	0	0	0	0	0	0	0	0	0	0
109	0	0	0	0	0	0	0	0	0	0	0	0

REFERENCES
Section 3

1. K. D. Smith, H. K. Gummel, J. D. Bode, D. B. Cuttriss, R. J. Nielson, and W. Rosenzweig, B.S.T.J. 42 1765 (1963).
2. W. Rosenzweig, H. K. Gummel, F. M. Smits, B.S.T.J. 42, 399 (1963).
3. W. Rosenzweig, F. M. Smits, W. L. Brown, J. Appl. Phys., to be published.
4. E. A. Lodi and D. L. Crowther, Appl. Phys. Letters 2 22 (1963).
5. D. S. Peck and M. C. Wooley, B.S.T.J. 42 1665 (1963).
6. H. K. Gummel and F. M. Smits, B.S.T.J. 43 1103 (1964).
7. Electromechanical Research Corp., College Park, Md.
8. W. L. Brown, T. M. Buck, L. V. Medford, E. W. Thomas, H. K. Gummel, G. L. Miller, and F. M. Smits, B.S.T.J. 42 899 (1963).
9. W. L. Brown, J. D. Gabbe, and W. Rosenzweig, B.S.T.J. 42 1505 (1963).
10. R. E. Carter, F. Reines, J. V. Wagner and M. E. Wyman, Phys. Rev. 113 280 (1959).
11. The Telstar II Experiment, Report in press.
12. F. L. Whipple, J. Geophys. Res. 68 4929 (1963).

FIGURE CAPTIONS

SECTION 3

Fig. 3-1 The solar cell and resistor arrangement in the radiation damage detectors.

Fig. 3-2 A photograph of the assembled spacecraft. The solar cell damage detector block is visible just below the octagonal section of the satellite structure.

Fig. 3-3 A closeup of the solar cell damage detector.

Fig. 3-4 The solar cell module assembly.

Fig. 3-5 The assembly of the complete solar cell damage detector.

Fig. 3-6 The cover assembly.

Fig. 3-7 The details of the mounting assembly.

Fig. 3-8 The optical angular acceptance of the solar cell damage experiment for assemblies with different sapphire shield thicknesses uncorrected for refraction.

Fig. 3-9 A typical test run of thrust vibration.

Fig. 3-10 Results of the temperature test at GSFC for bare and aluminum oxide coated solar cell damage detector assemblies.

Fig. 3-11 The module layout for detector no. 52.

Fig. 3-12 The module layout for detector no. 53.

Fig. 3-13 Wavelength dependence of the optical loss due to sapphire covers.

Fig. 3-14 Data of Channel PP3 for the 10 mil sapphire shielded detectors for the first day in orbit. The ordinate is the comb filter number of the decommutated data.

Fig. 3-15 The geometry of the cell illumination in space.

Fig. 3-16 Data for day 6 from Channel PP3.

Fig. 3-17 The solar aspect angle and damage experiment temperature as a function of time in orbit.

Fig. 3-18 Data for Days 14 and 41 from Channel PP3.

Fig. 3-19 The angular dependence of solar cell output on angle of illumination.

Fig. 3-20 The temperature dependence of the solar cell short circuit current for unbombarded and heavily bombarded cells.

Fig. 3-21 The annual variation of the solar intensity at the earth.

Fig. 3-22 The results of the four radiation damage detector assemblies corrected for temperature, mean solar distance, and angle of illumination versus time in orbit.

Fig. 3-23 The problem of reflection on the 10 mil shielded solar cells near normal incidence.

Fig. 3-24 The relative damage rates observed in the experiment compared with the expected damage dependence on shield thickness for electrons and protons as seen by Explorer XV in space.

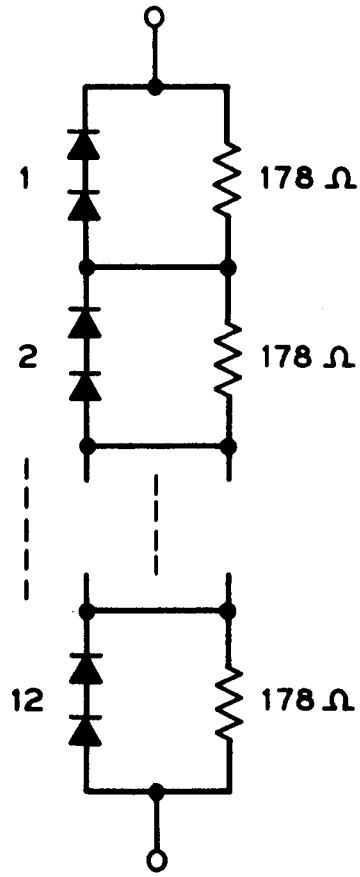

Fig. 3-1

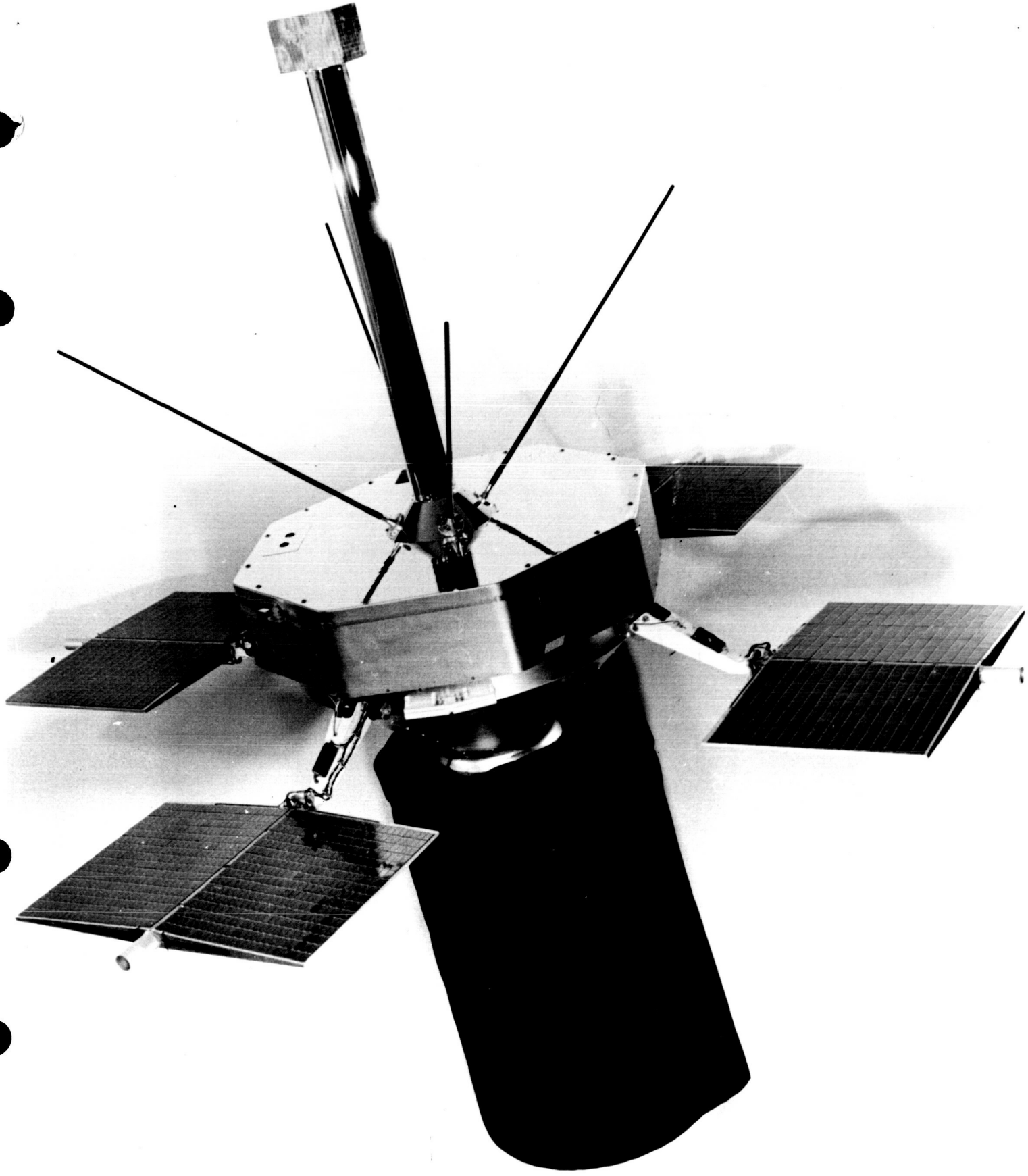

Fig. 3-2

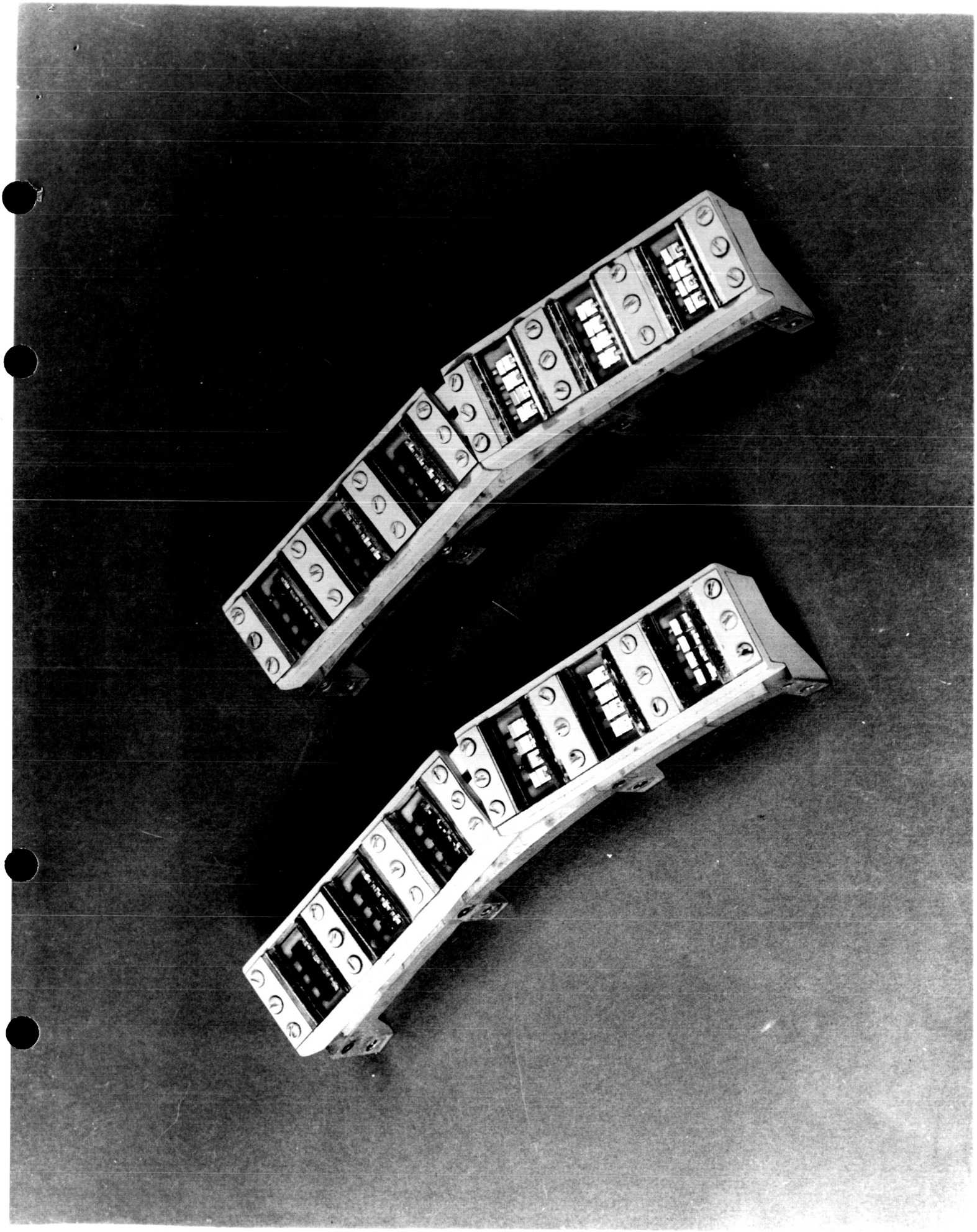

Fig. 3-3

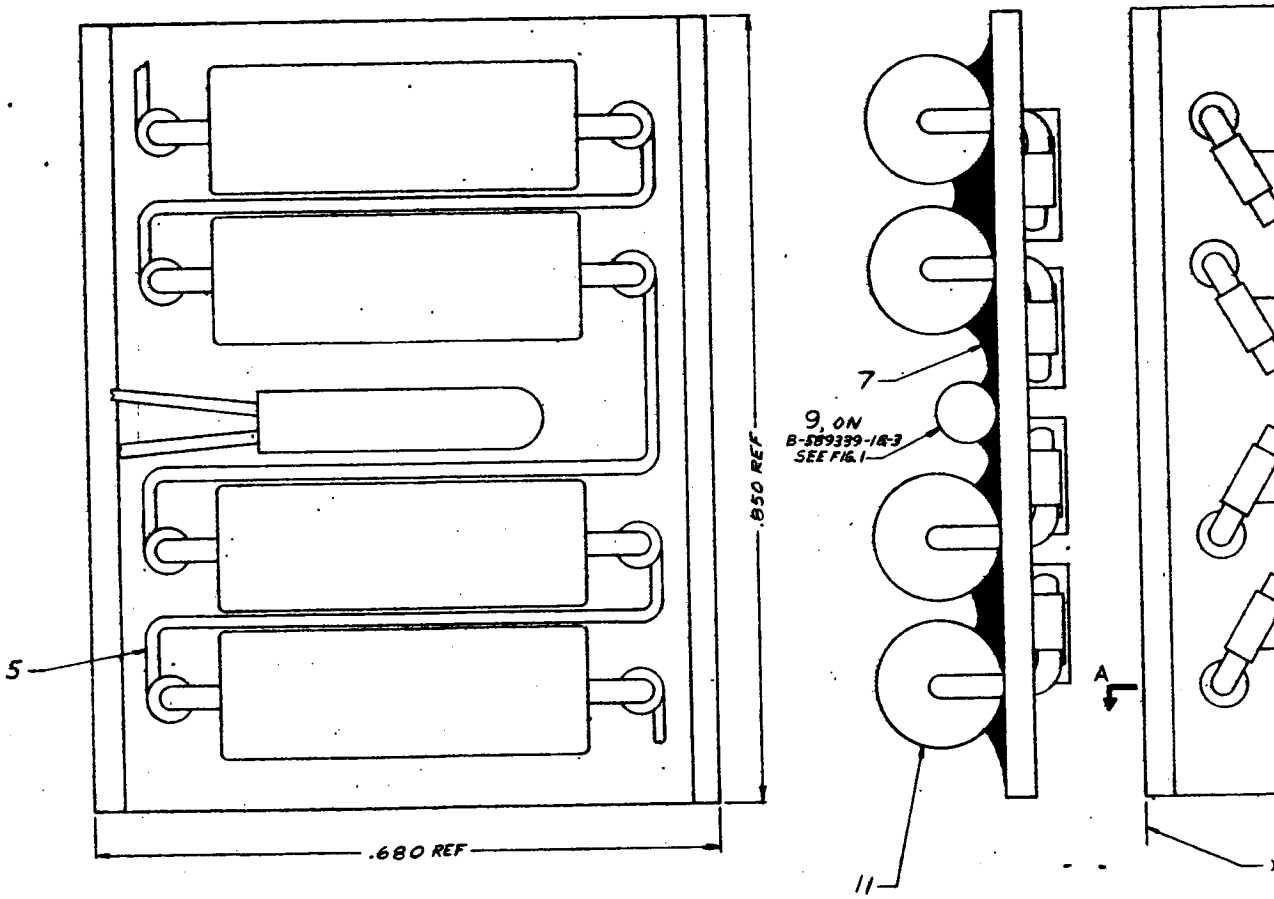

Fig. 3-4

NOTES:

1. SURFACES X AND Y SHALL BE PARALLEL WITHIN ±.005.
2. AFTER INSPECTION OF ASSEMBLY, CELL TABS AND RESISTOR LEADS SHALL BE COVERED WITH EPOXY.

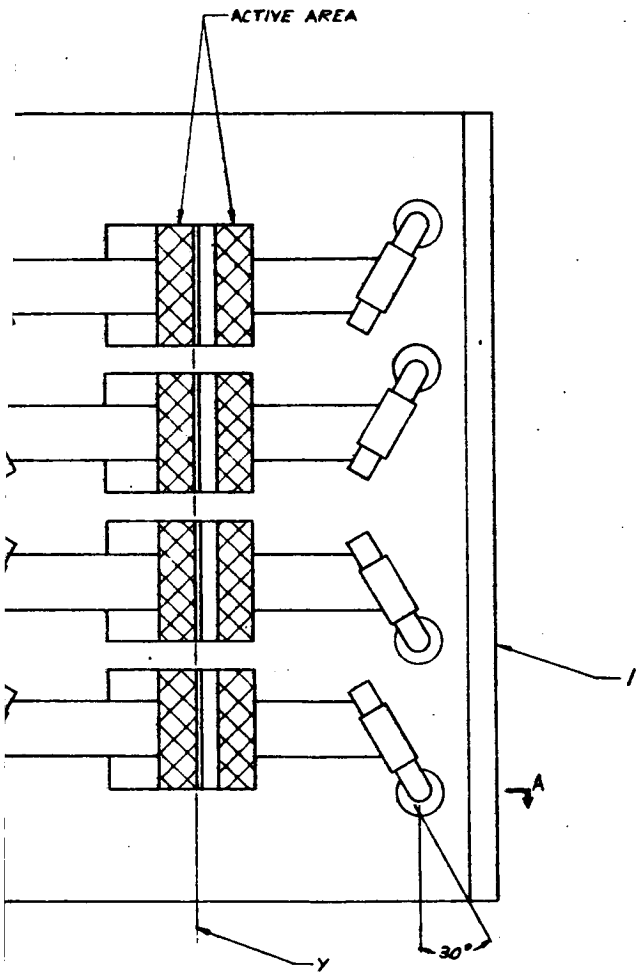

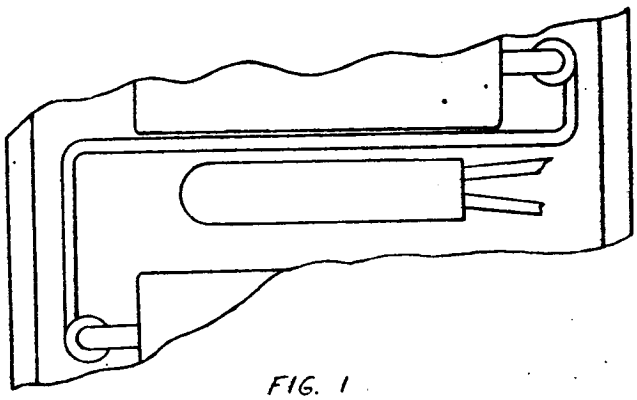

FIG. 1

B-589339-3
OTHERWISE SAME AS -1

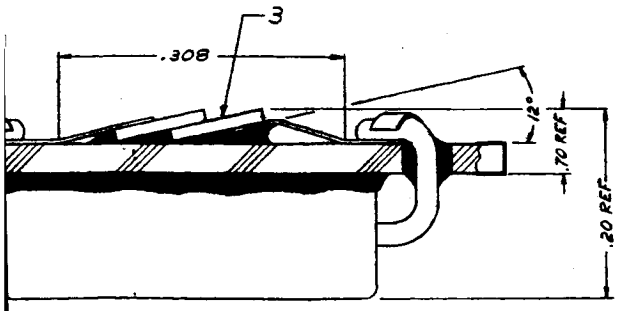

SECT A-A

ITEM	PIECE	NAME	B-589339-2 REQ	B-589339-1&2 REQ
11		RESISTOR	4	4
10				
9		THERMISTER VECO VACTORY ENG. CO.		1
8				
7		EPOXY	✓	✓
6				
5		WIRE COPPER TIN PLATED .025 DIA	✓	✓
4				
3		CELL, SOLAR ASSEMBLY	4	4
2				
1		PLATE	1	1

STOCK LIST

UNLESS OTHERWISE SPECIFIED, ALL DIMENSIONS ARE IN INCHES. NONLIMITED DIMENSIONS OTHER THAN SIZE OF RAW MATERIAL SHALL BE HELD AS FOLLOWS WHEN EXPRESSED:
TO 2 DECIMAL PLACES ± AS ANGLES ±
TO 3 DECIMAL PLACES ± .005

DWG SIZE 6S

USED ON DWG

SOLAR MT6 PLATE ASSEMBLY

SCALE 10/1

BELL TELEPHONE LABORATORIES INCORPORATED

B-

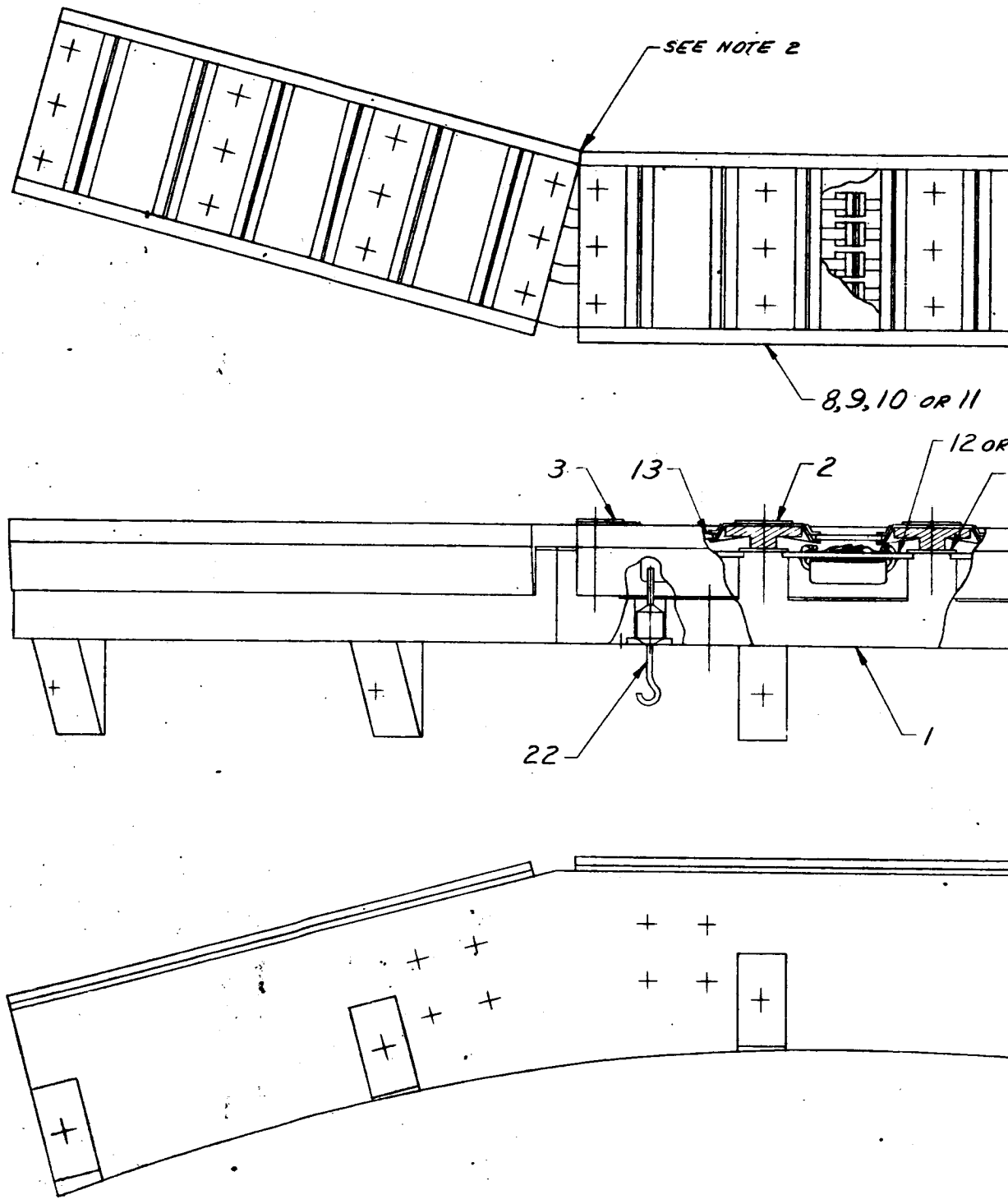
SEE NOTE 2
8,9,10 OR 11
12 OR
3
13
2
22
1

NOTES:

1. SCREW HEADS SHALL BE CHEMICALLY STRIPPED AND SPRAYED WITH ALUMINUM OXIDE .005 THK.
2. CUT CORNERS ON COVERS TO FIT SHAPE OF HOUSING.

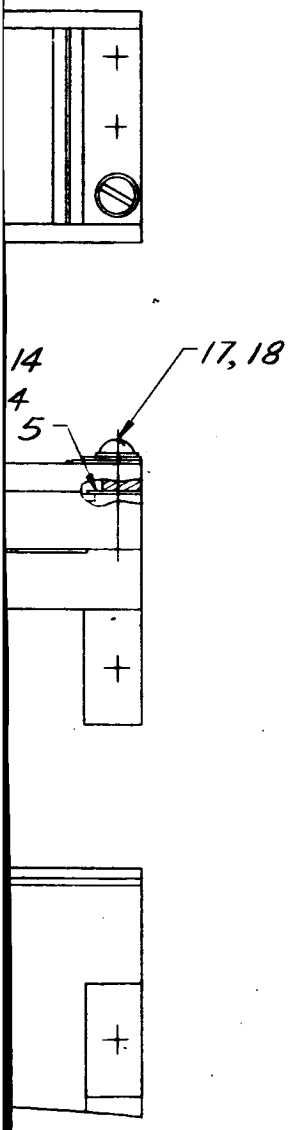

REQ				IDENTIFICATION NO.	DESCRIPTION	REF DESIG	NOTE	ITEM
8	8	8	8		TERMINAL, FEEDTHRU, 3/4			22
								21
								20
24	24	24	24		WASHER, SHAKEPROOF, INT TOOTH LOCK, NO. 2 (.086)			18
24	24	24	24		SCR, RHM, .086-56 X 3/8		1	17
								16
								15
1	1	1	1	B-589337-3	SOLAR MTG PLATE ASSY			14
4	4	4	4	B-589337-2				13
1	1	1	1	B-589337-1				12
2				B-589335-4	COVER ASSEMBLY			11
	2			B-589335-3				10
		2		B-589335-2				9
			2	B-589335-1				8
								7
								6
4	4	4	4	B-589347	SPRING			5
4	4	4	4	B-589346				4
4	4	4	4	B-589943-2	PLATE			3
4	4	4	4	B-589943-1				2
1	1	1	1	B-589941	HOUSING			1

STOCK LIST

✓	✓	✓	✓	B-590963 WIRING DIAGRAM, CELL MTG PLATE

SUPPLEMENTARY DRAWINGS

B-590962-4
B-590962-3
B-590962-2
B-590962-1

SIGNIFICANCE OF SYMBOLS AND ITEM NUMBER SUFFIXES

B—PARTIAL ASSEMBLIES ON OTHER DRAWINGS WITH STOCK LISTS
D—PARTS SHIPPED LOOSE
} ITEMS NOT SPECIFIED AS "B" OR "D" PARTS IN ITEM COLUMN ARE INDIVIDUAL ("A") PARTS

WHERE ITEMS HAVE REFERENCE DESIGNATIONS, THEY MAY BE USED IN LIEU OF ITEM NUMBERS ON THE DELINEATION.
✓ IN "REQ" COLUMN OF STOCK LIST—QUANTITY AS REQUIRED
✓ IN "REQ" COLUMN OF SUPPLEMENTARY DWG LIST DRAWING REQUIRED
● DENOTES MANUFACTURE DISCONTINUED
■ DENOTES MANUFACTURE LIMITED
AB—DENOTES APPARATUS BOOK DRAWINGS

UNLESS OTHERWISE SPECIFIED, ALL DIMENSIONS ARE IN INCHES. NONLIMITED DIMENSIONS OTHER THAN SIZE OF RAW MATERIAL SHALL BE HELD AS FOLLOWS WHEN EXPRESSED:
TO 2 DECIMAL PLACES ±
TO 3 DECIMAL PLACES ±
AS ANGLES ±
FOR GENERAL INFORMATION ON SYMBOLS AND NOTES REFER TO MANUFACTURING STANDARD 16.003, PART 3, SECTION 227.

DWG SIZE 4 S

A-
SIGN R.A. McGinty
DRAWN M.M. Sannon
ISSUE 1

B-590962

USED ON | DWG
RADIATION DAMAGE DET FOR NASA SERB SATELLITE ASSEMBLY

SCALE 2/1

WESTERN ELECTRIC CO, INC
ENGINEER OF MANUFACTURE

BELL TELEPHONE LABORATORIES INCORPORATED

B-590962
A-

Fig. 3-5

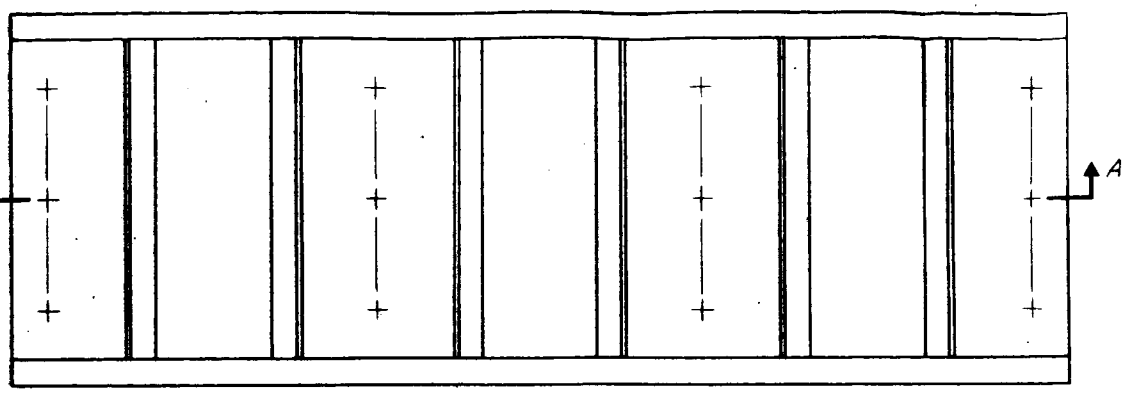

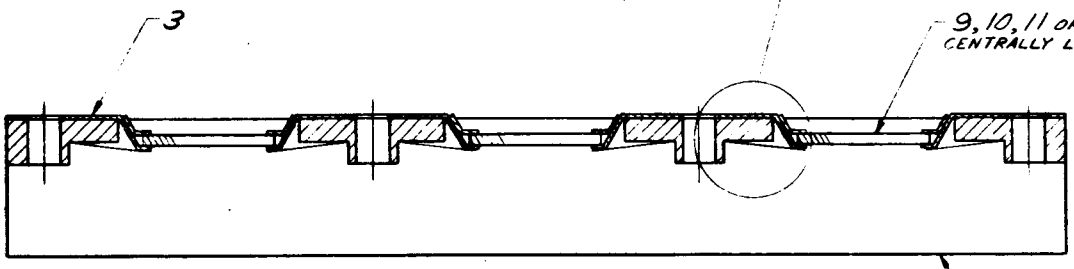

SECT. A-A

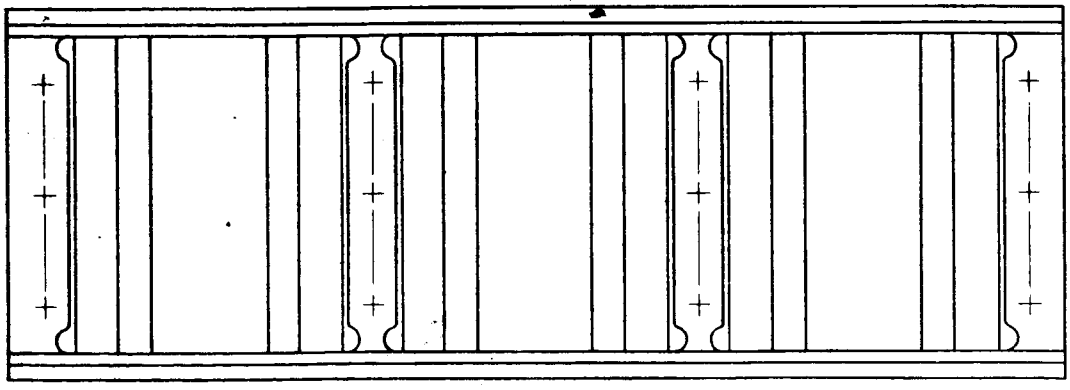

NOTES:

1. MICA, ITEM 4, SHALL BE LOCATED APPROXIMATELY AS SHOWN AND SHALL NOT EXTEND BEYOND END OF SUPPORT, ITEM 2 OR 3.

2. EPOXIDE PLASTIC, NO. ERL-2795, AND HARDENER, NO. 2807, SHALL BE APPLIED TO ALL CONTACT AREAS AND DESIGNATED DARKENED AREAS. ABOVE PLASTIC AND HARDENER MAY BE OBTAINED FROM UNION CARBIDE CORP, 270 PARK AVE, NEW YORK 17, N.Y.

3. SPOT WELD RETAINER, ITEM 5, 6, 7 OR 8, TO SUPPORT, ITEM 2 OR 3.

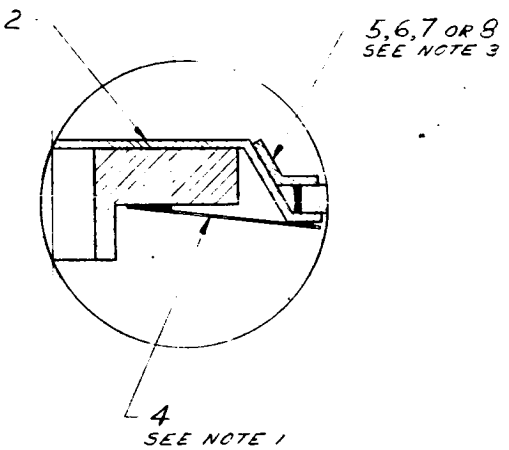

SCALE: 10/1

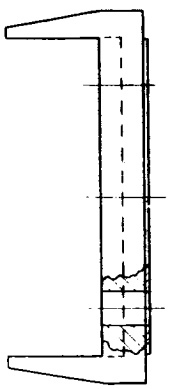

ITEM	PIECE	NAME	B-589335-4 REQ'D	B-589335-3 REQ'D	B-589335-2 REQ'D	B-589335-1 REQ'D
12	B-589342-4	PLATE	3			
11	B-589342-3	PLATE		3		
10	B-589342-2	PLATE			3	
9	B-589342-1	PLATE				3
8	B-589341	RETAINER	6			
7	B-589340-3	RETAINER		6		
6	B-589340-2	RETAINER			6	
5	B-589340-1	RETAINER				6
4	B-589345	MICA	6	6	6	6
3	B-589343	END SUPPORT	2	2	2	2
2	B-589344	SUPPORT	2	2	2	2
1	B-589349	COVER	1	1	1	1

STOCK LIST

UNLESS OTHERWISE SPECIFIED, ALL DIMENSIONS ARE IN INCHES. NONLIMITED DIMENSIONS OTHER THAN SIZE OF RAW MATERIAL SHALL BE HELD AS FOLLOWS WHEN EXPRESSED:
TO 2 DECIMAL PLACES ± AS ANGLES ±
TO 3 DECIMAL PLACES ±

FOR GENERAL INFORMATION ON SYMBOLS AND NOTES REFER TO MANUFACTURING STANDARD 16.003 PART 2 SECTION 227

DWG SIZE 6S

P-

DWN B.A. REGENT
DRAWN B.B. SAMMONS
ISSUE 1

ISSUE 1 B-589335

ASSY USED ON	DWG
	B-590962

COVER ASSEMBLY

SCALE 4/1 & AS SHOWN

WESTERN ELECTRIC CO. INC.
ENGINEER OF MANUFACTURE
CENTRAL OFFICE EQUIPMENT

BELL TELEPHONE LABORATORIES INCORPORATED

CAD B-589335 P-

Fig. 3-6

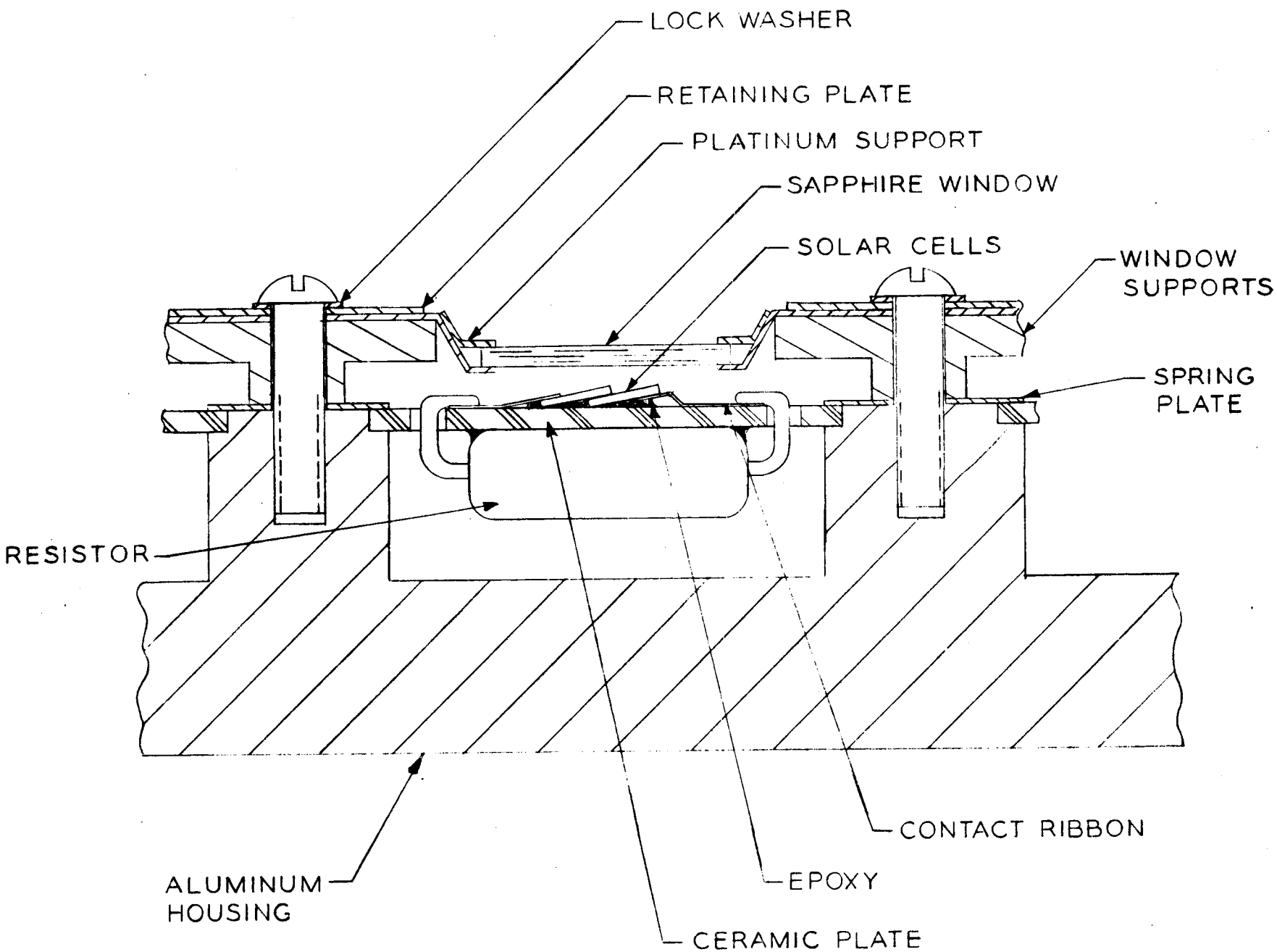
LOCK WASHER
RETAINING PLATE
PLATINUM SUPPORT
SAPPHIRE WINDOW
SOLAR CELLS
WINDOW SUPPORTS
SPRING PLATE
RESISTOR
CONTACT RIBBON
EPOXY
ALUMINUM HOUSING
CERAMIC PLATE

Fig. 3-7

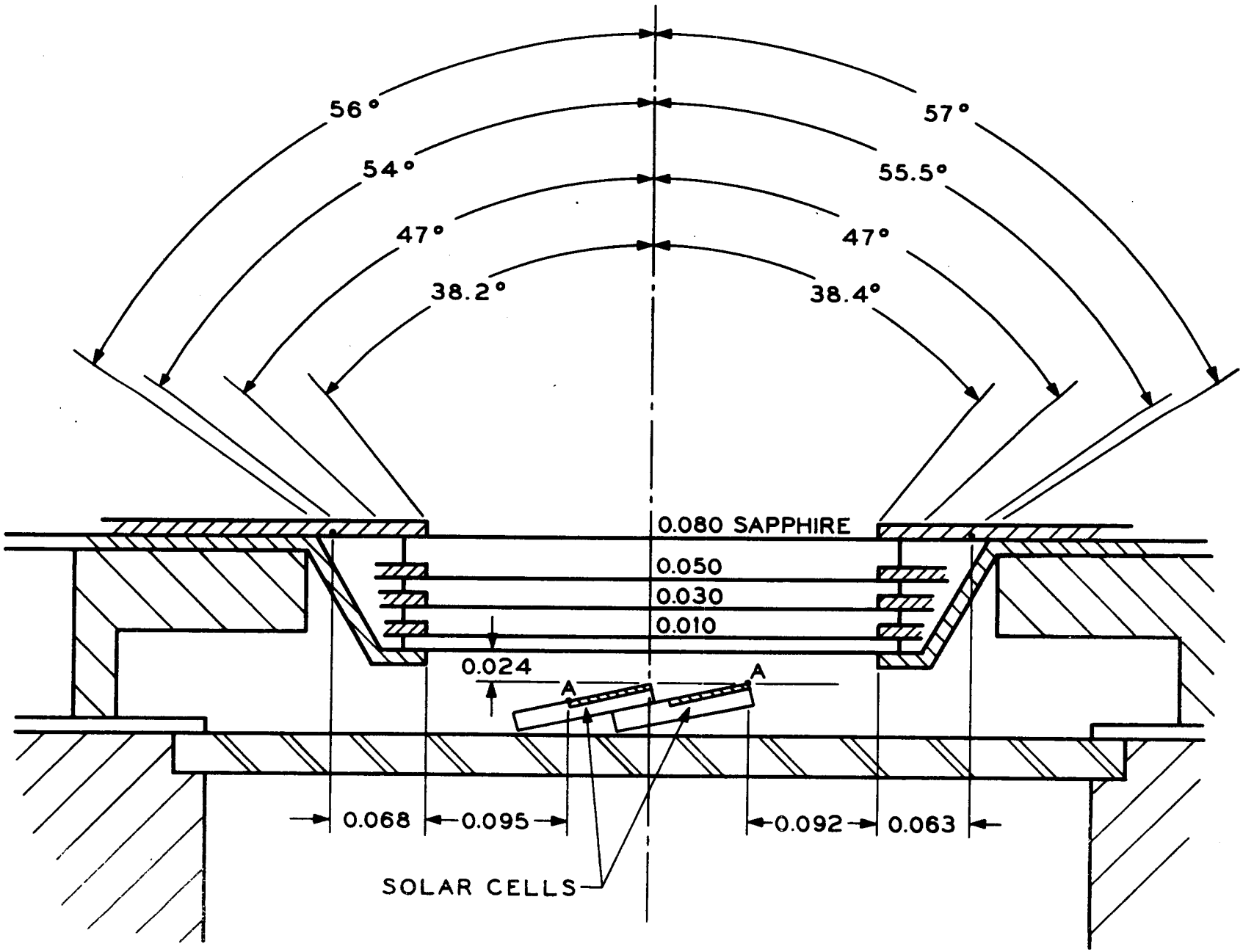
56°
54°
47°
38.2°
57°
55.5°
47°
38.4°
0.080 SAPPHIRE
0.050
0.030
0.010
0.024
A
A
0.068
0.095
0.092
0.063
SOLAR CELLS

Fig. 3-8

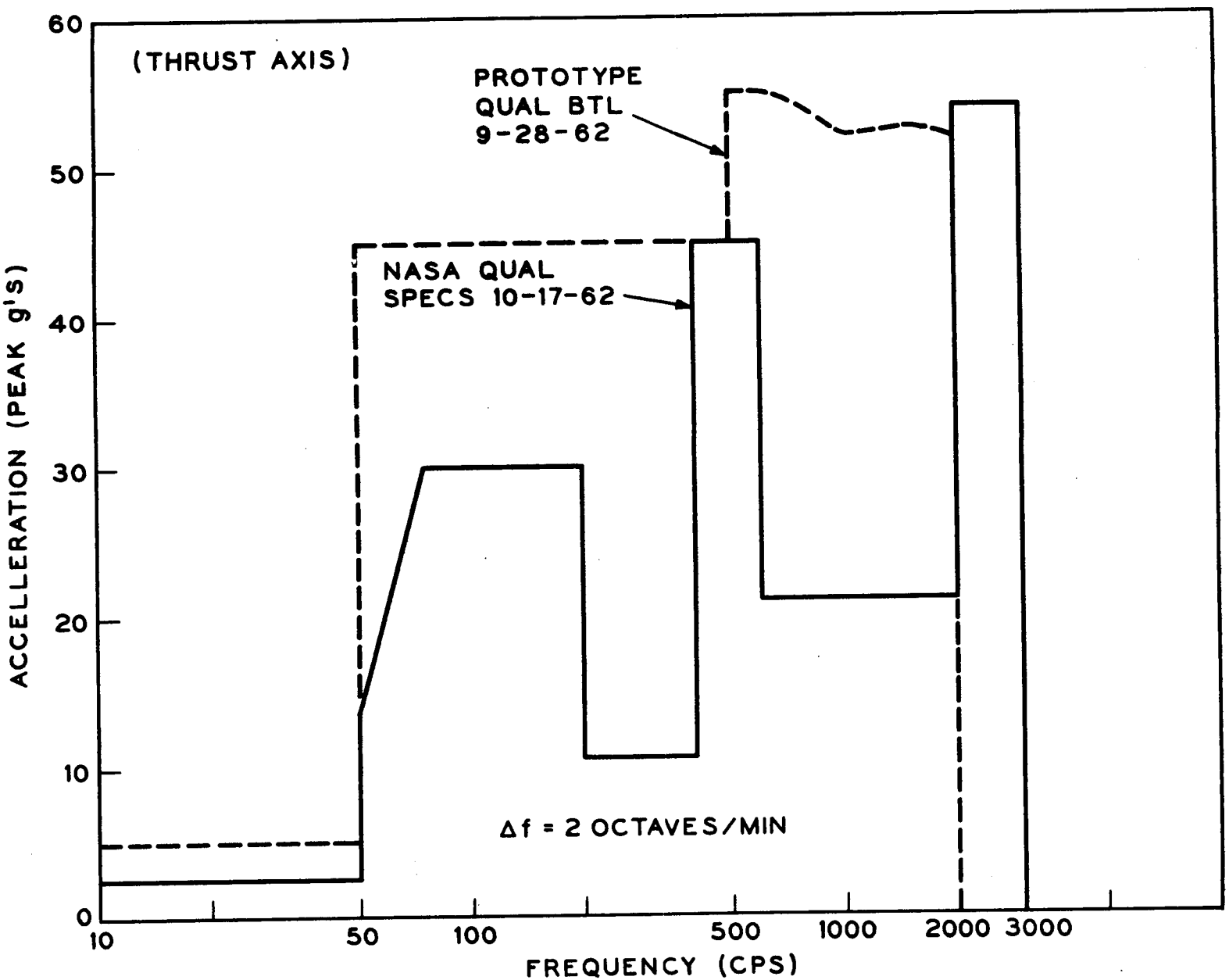
(THRUST AXIS)
PROTOTYPE
QUAL BTL
9-28-62
NASA QUAL
SPECS 10-17-62
Δf = 2 OCTAVES/MIN
ACCELLERATION (PEAK g's)
60
50
40
30
20
10
0
10
50
100
500
1000
2000
3000
FREQUENCY (CPS)

Fig. 3-9

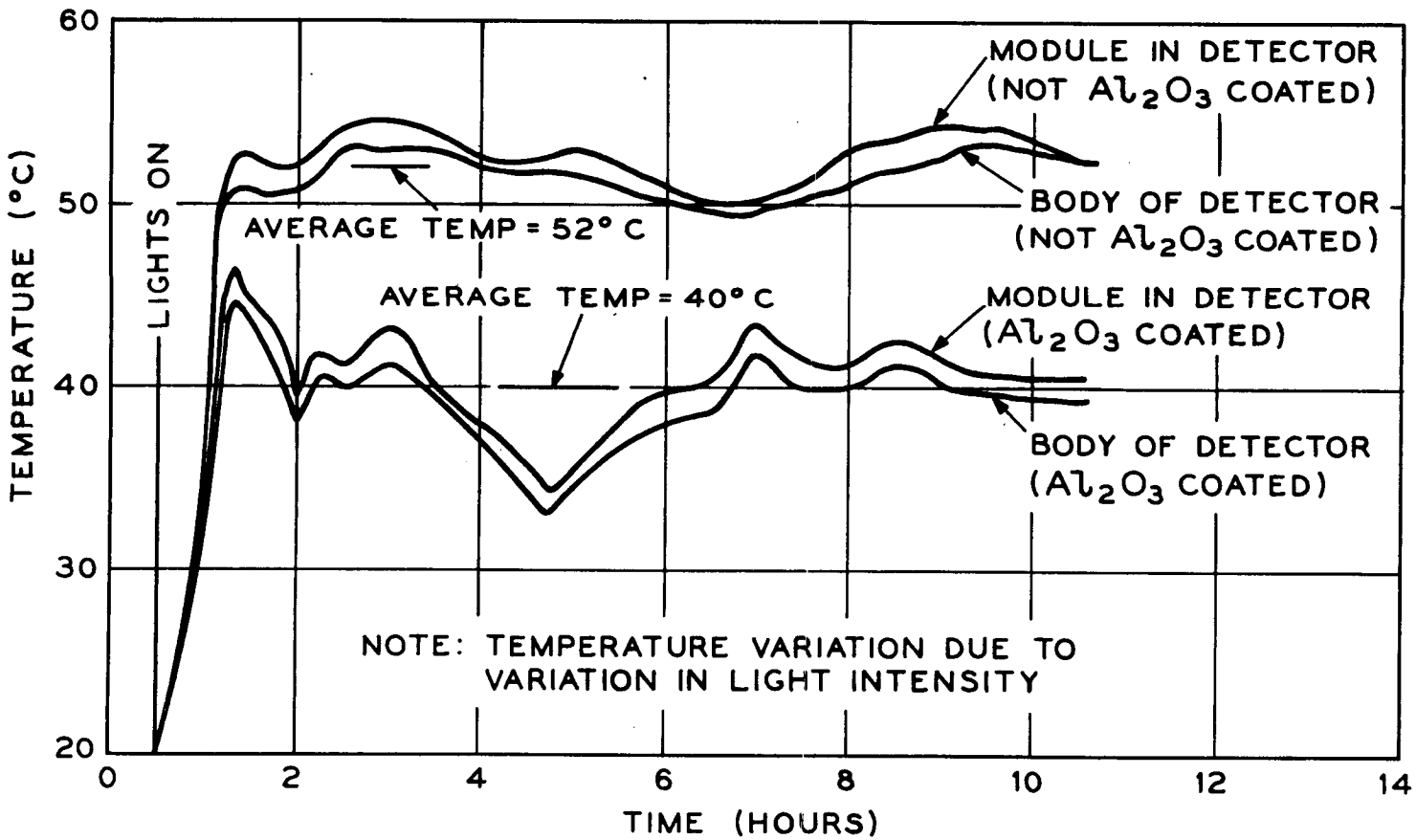
60
50
40
30
20
TEMPERATURE (°C)
LIGHTS ON
AVERAGE TEMP = 52° C
AVERAGE TEMP = 40° C
MODULE IN DETECTOR
(NOT Al_2O_3 COATED)
BODY OF DETECTOR
(NOT Al_2O_3 COATED)
MODULE IN DETECTOR
(Al_2O_3 COATED)
BODY OF DETECTOR
(Al_2O_3 COATED)
NOTE: TEMPERATURE VARIATION DUE TO
VARIATION IN LIGHT INTENSITY
0
2
4
6
8
10
12
14
TIME (HOURS)

Fig. 3-10

SERB - SATELLITE #S3B & S3C

DETECTOR #52

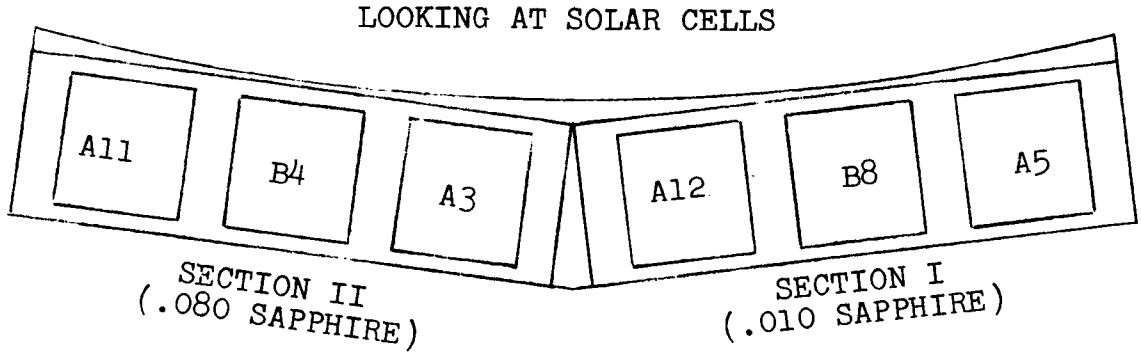

SECTION I

1. - .010 SAPPHIRE COVERS
2. MODULES #- A12, B8, A5
3. THERMISTOR #238

SECTION II

1. - .080 SAPPHIRE COVERS
2. MODULES #- A3, B4, A11
3. THERMISTOR #231

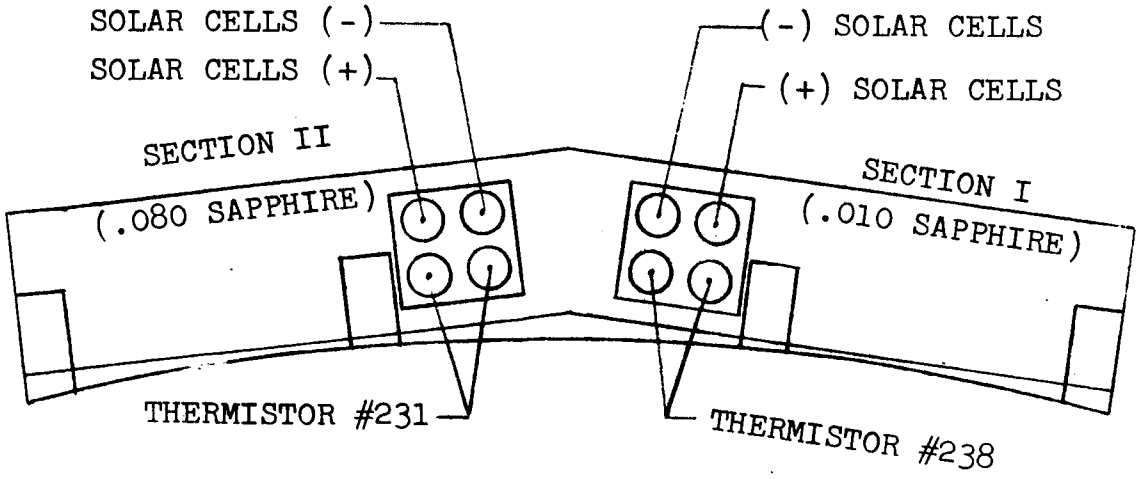

0°C - 104.820 KΩ
50°C - 10.964 KΩ

0°C - 99.500 KΩ
50°C - 10.472 KΩ

Fig. 3-11

SERB - SATELLITE #S3B & S3C

DETECTOR #53

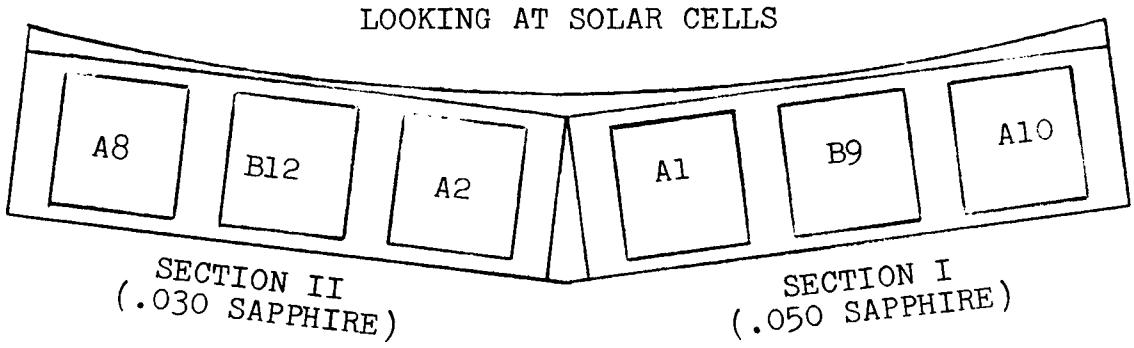

SECTION I

1. - .050 SAPPHIRE COVERS
2. MODULES #- A1, B9, A10
3. THERMISTOR #234

SECTION II

1. - .030 SAPPHIRE COVERS
2. MODULES #- A8, B12, A2
3. THERMISTOR #240

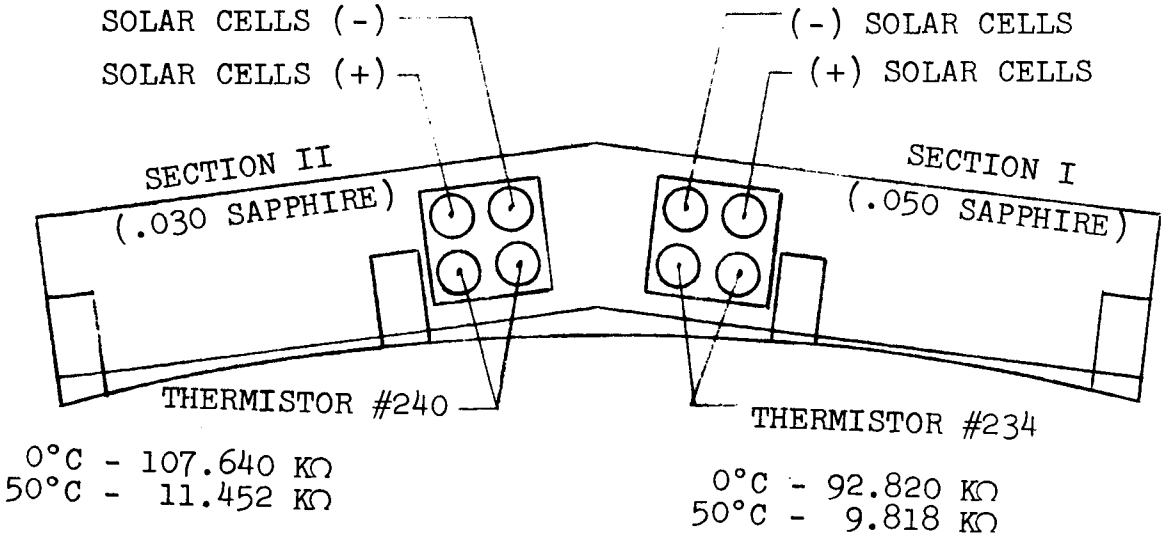

Fig. 3-12

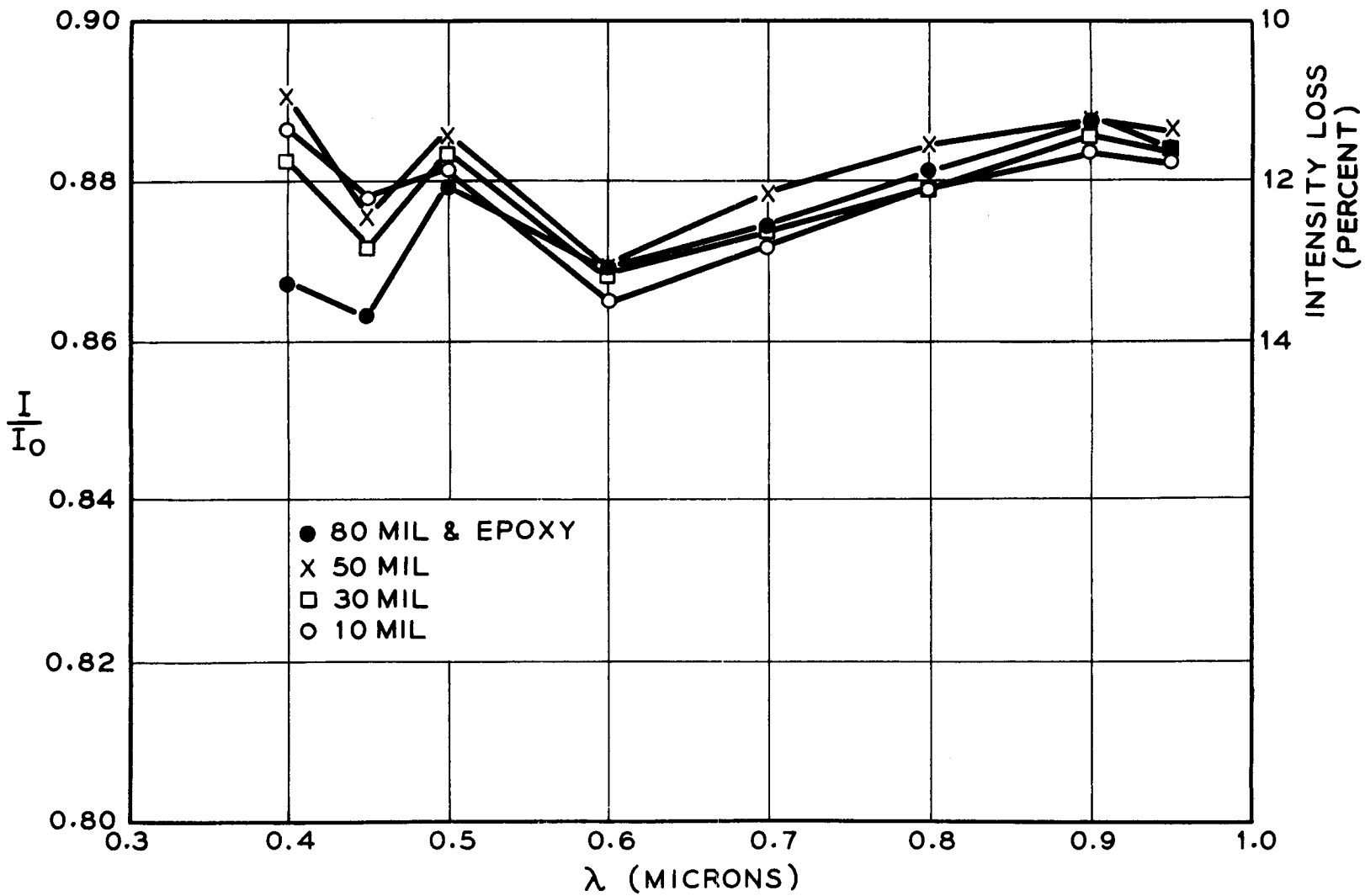
0.90
0.88
0.86
0.84
0.82
0.80
I/Io
10
12
14
INTENSITY LOSS (PERCENT)
0.3
0.4
0.5
0.6
0.7
0.8
0.9
1.0
λ (MICRONS)
● 80 MIL & EPOXY
X 50 MIL
□ 30 MIL
○ 10 MIL

Fig. 3-13

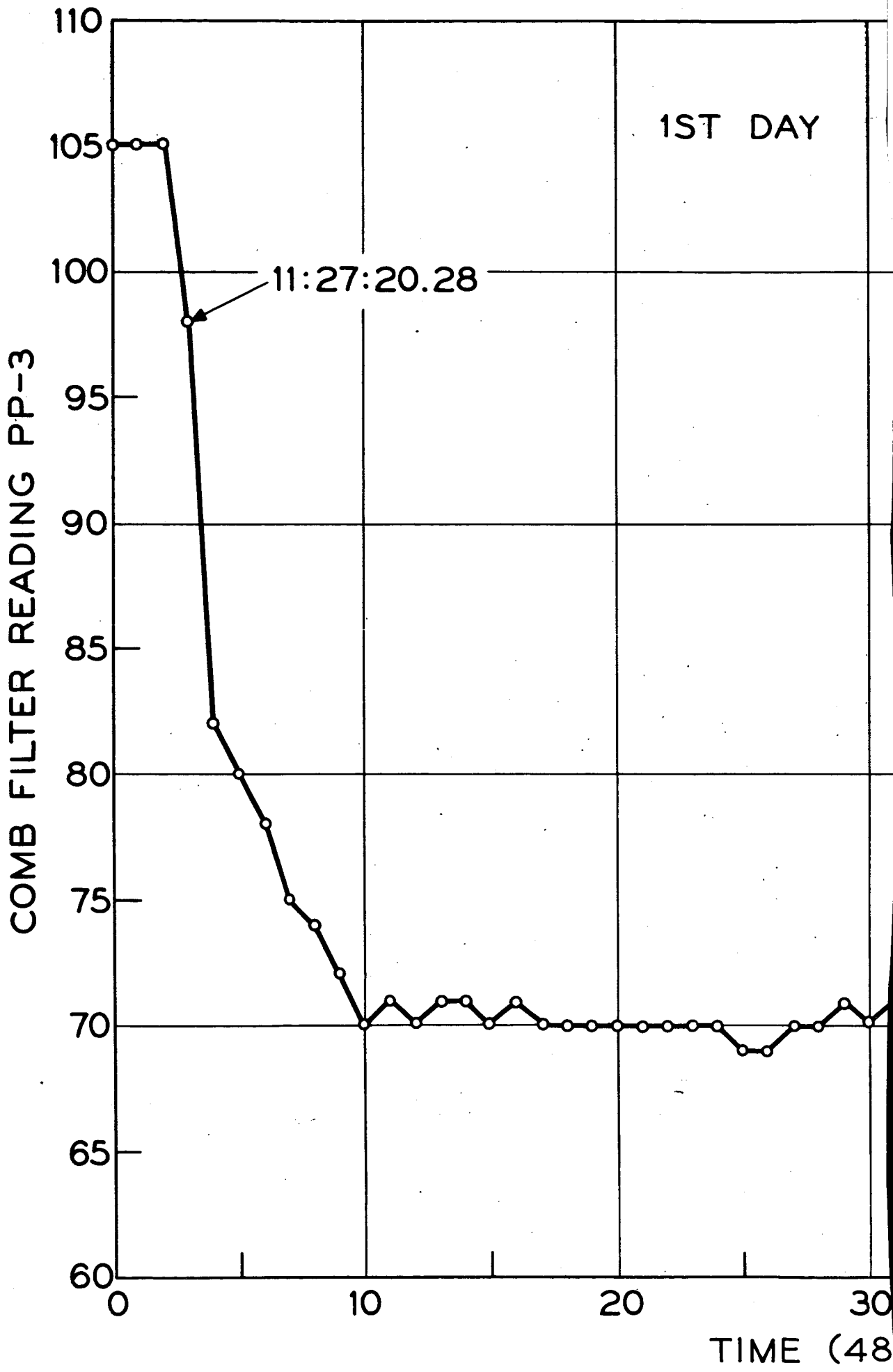
1ST DAY
11:27:20.28
COMB FILTER READING PP-3
110
105
100
95
90
85
80
75
70
65
60
0
10
20
30
TIME (48

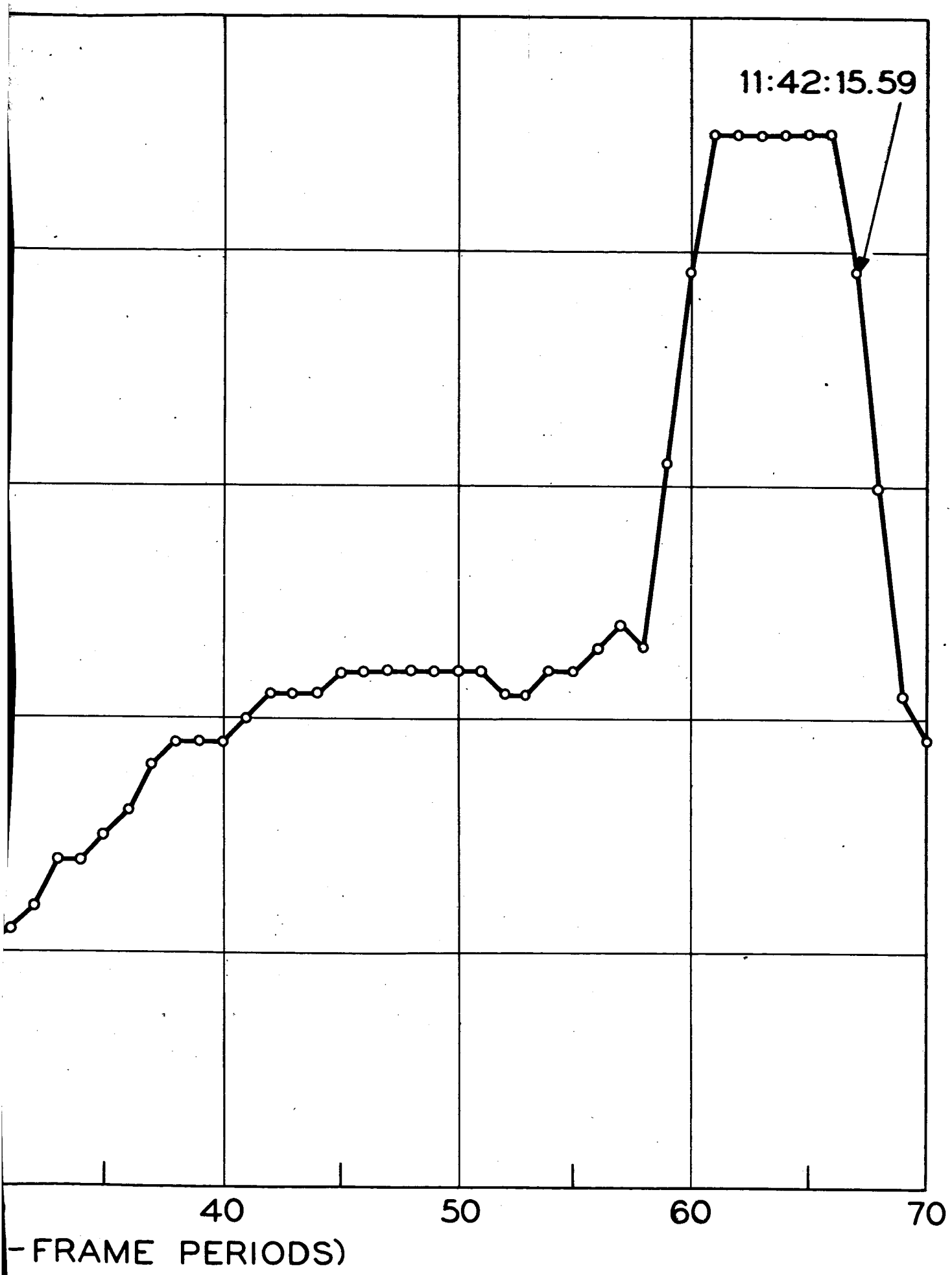

Fig. 3-14

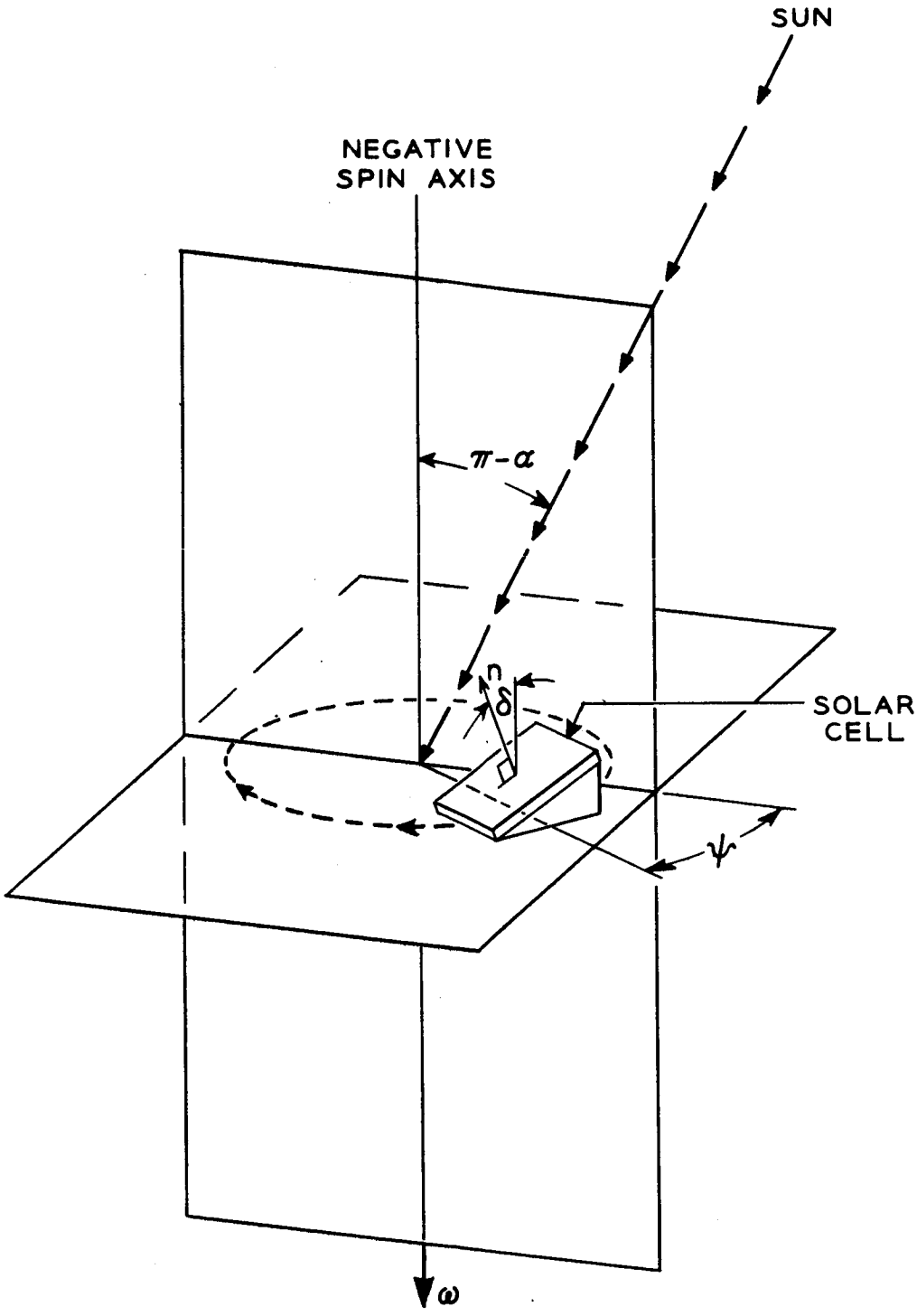

Fig. 3-15

			ENGR W L B
			DRAWN
		DATE	CASE

OGILVIE PRESS, INC. PI 129
PRINTED IN U.S.A. E-7544 (8-60)

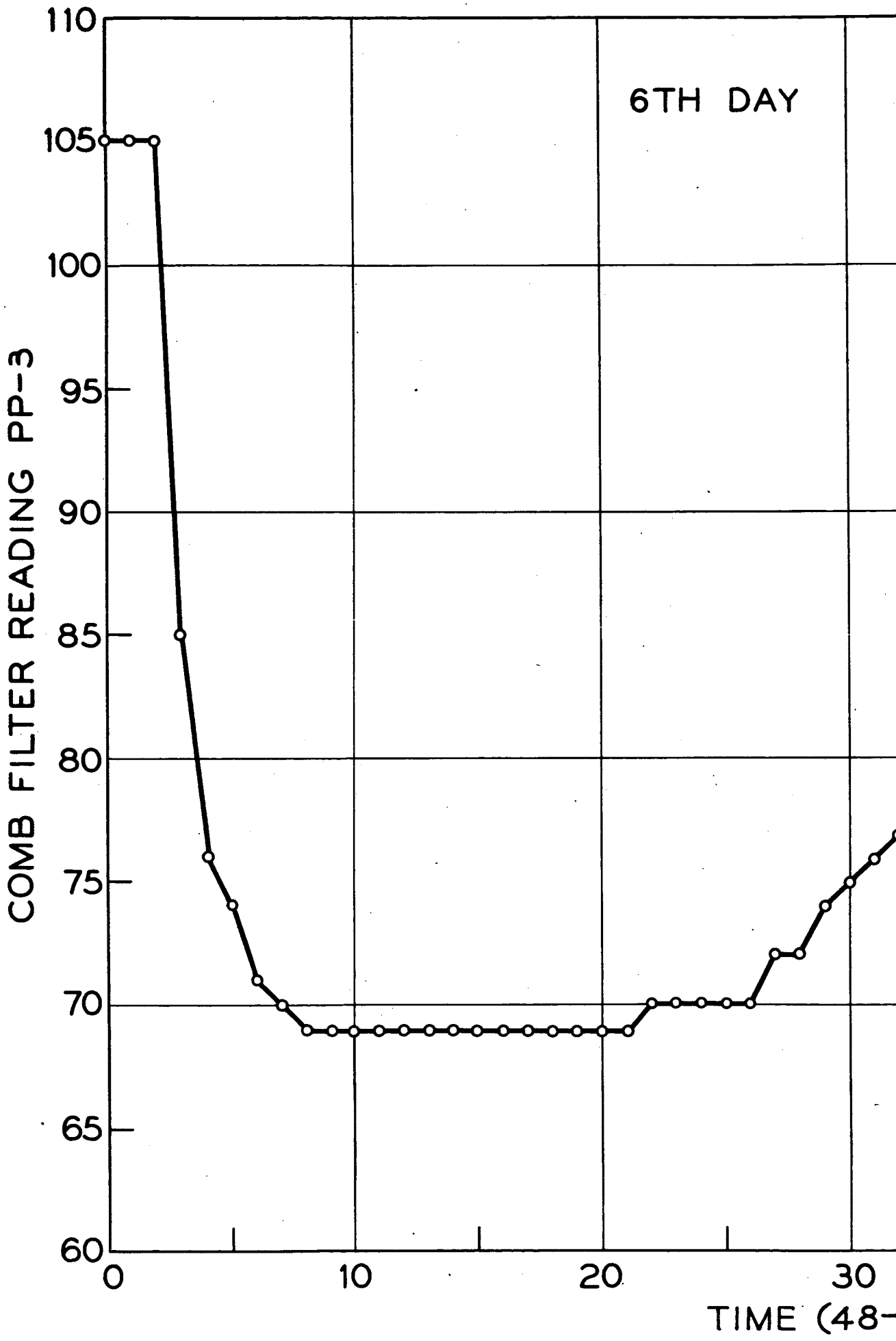
6TH DAY
COMB FILTER READING PP-3
110
105
100
95
90
85
80
75
70
65
60
0
10
20
30
TIME (48-

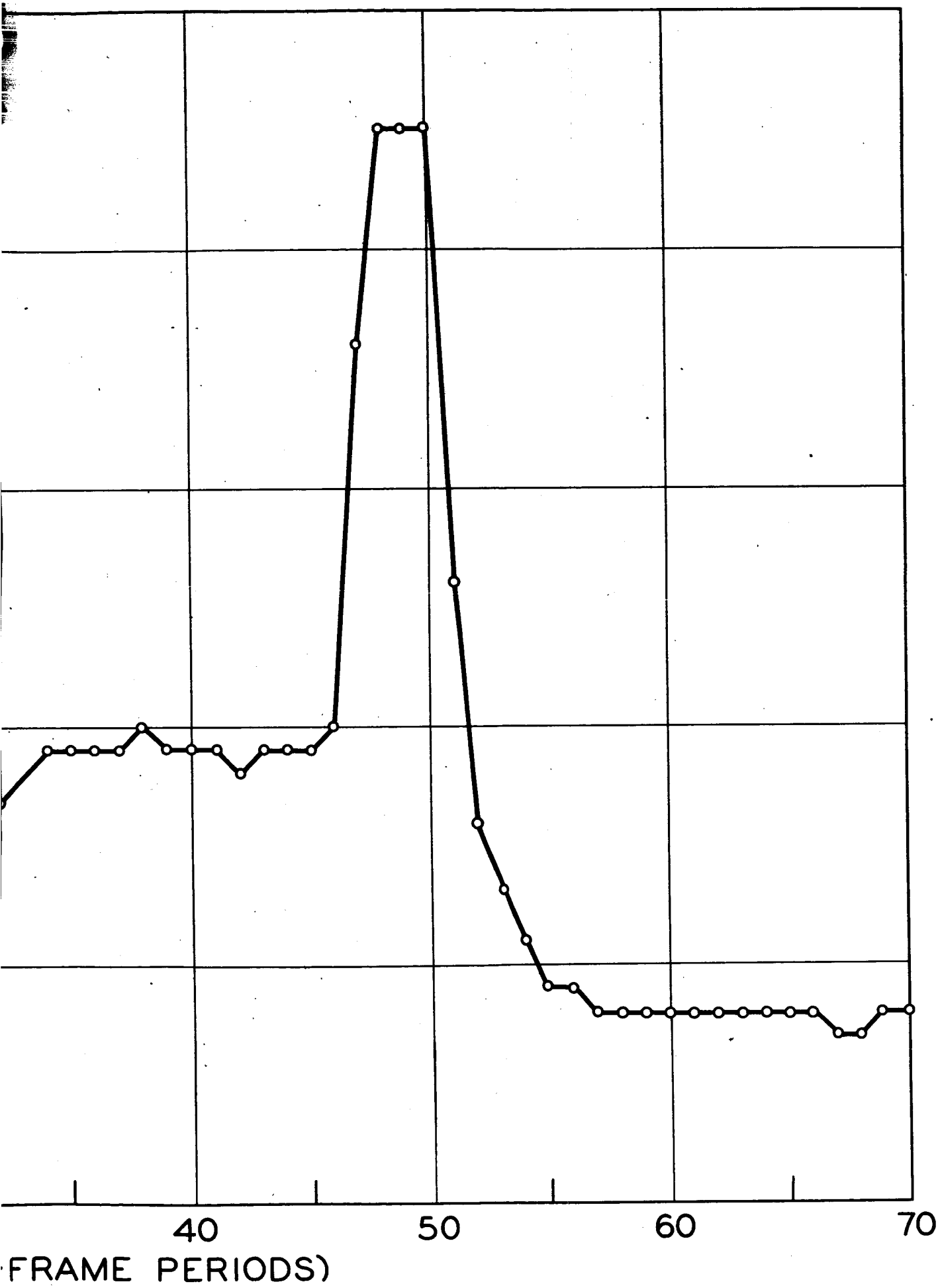

Fig. 3-16

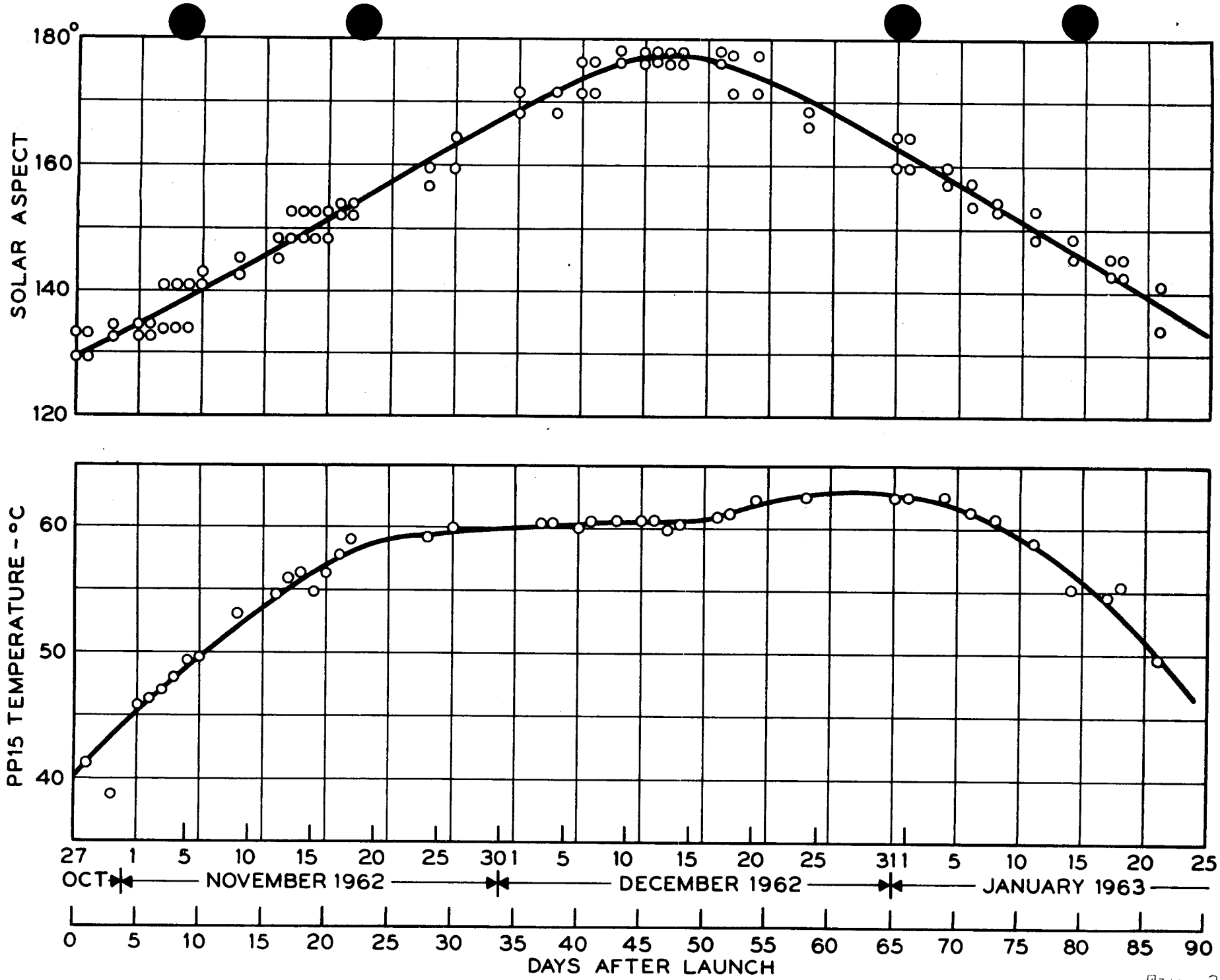
SOLAR ASPECT
180°
160
140
120
PP15 TEMPERATURE - °C
60
50
40
27 1 5 10 15 20 25 30 1 5 10 15 20 25 31 1 5 10 15 20 25
OCT
NOVEMBER 1962
DECEMBER 1962
JANUARY 1963
0 5 10 15 20 25 30 35 40 45 50 55 60 65 70 75 80 85 90
DAYS AFTER LAUNCH

Fig. 3-17

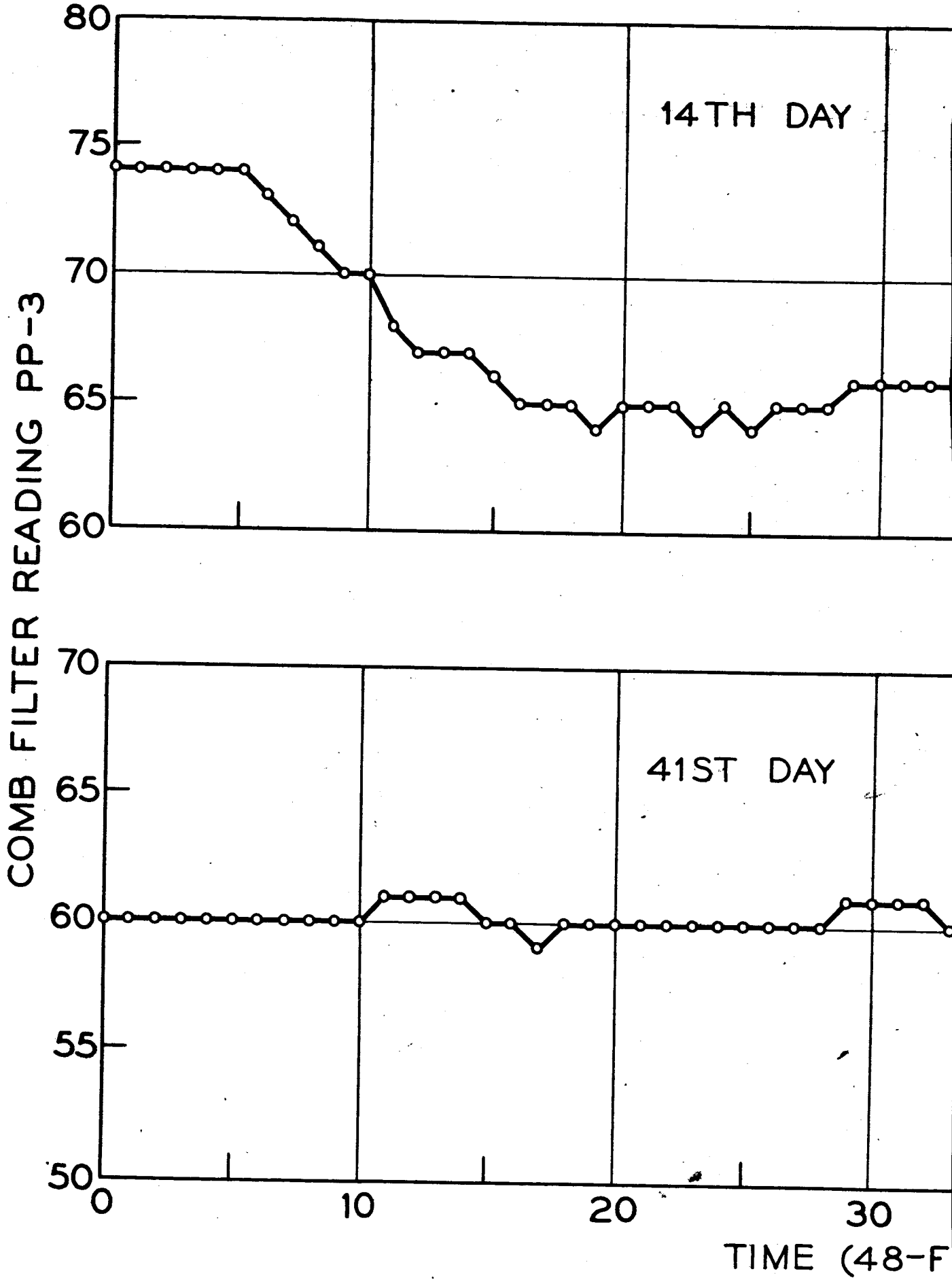
14TH DAY
41ST DAY
COMB FILTER READING PP-3
80
75
70
65
60
70
65
60
55
50
0
10
20
30
TIME (48-F

Fig

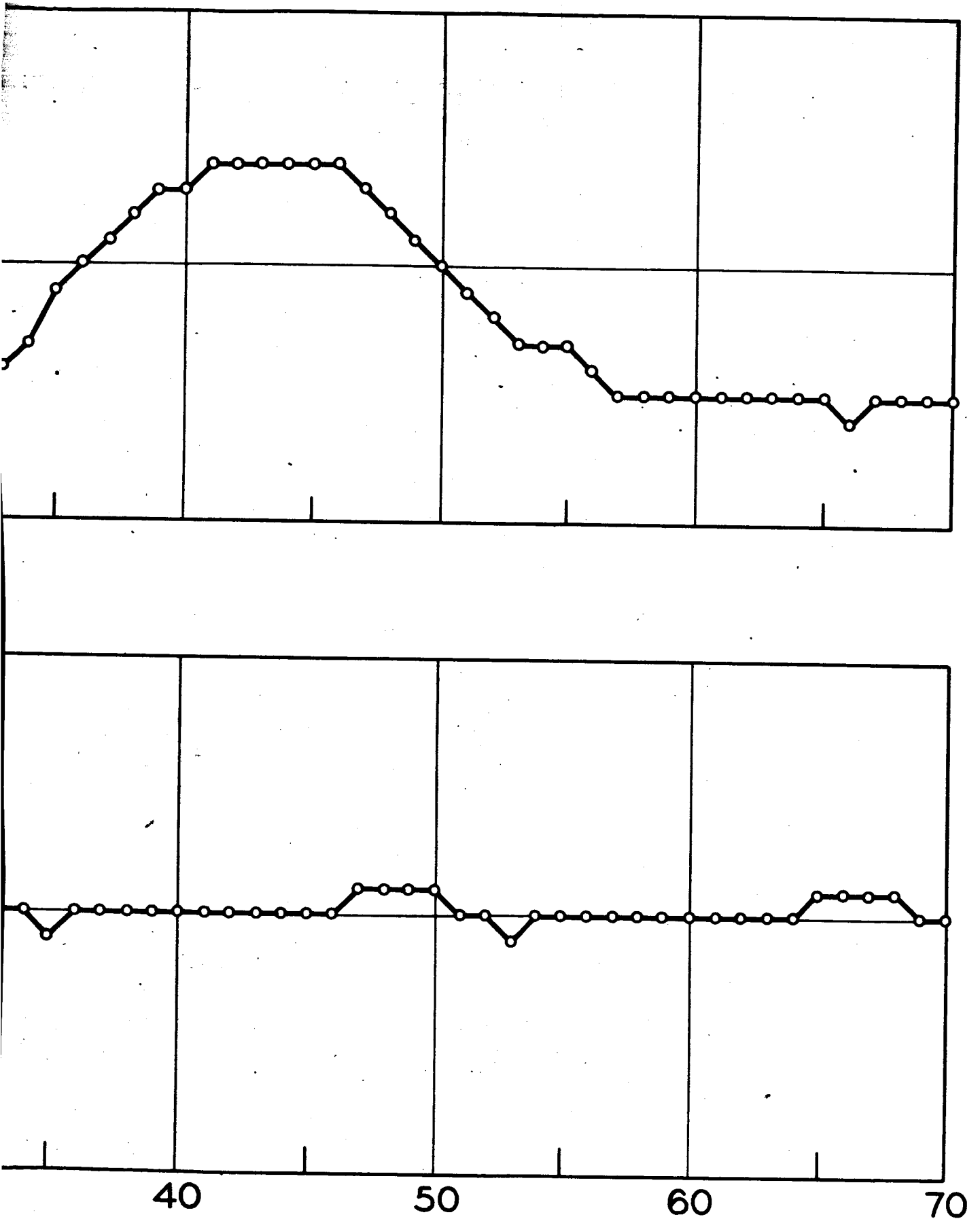

RAME PERIODS)

. 3-18

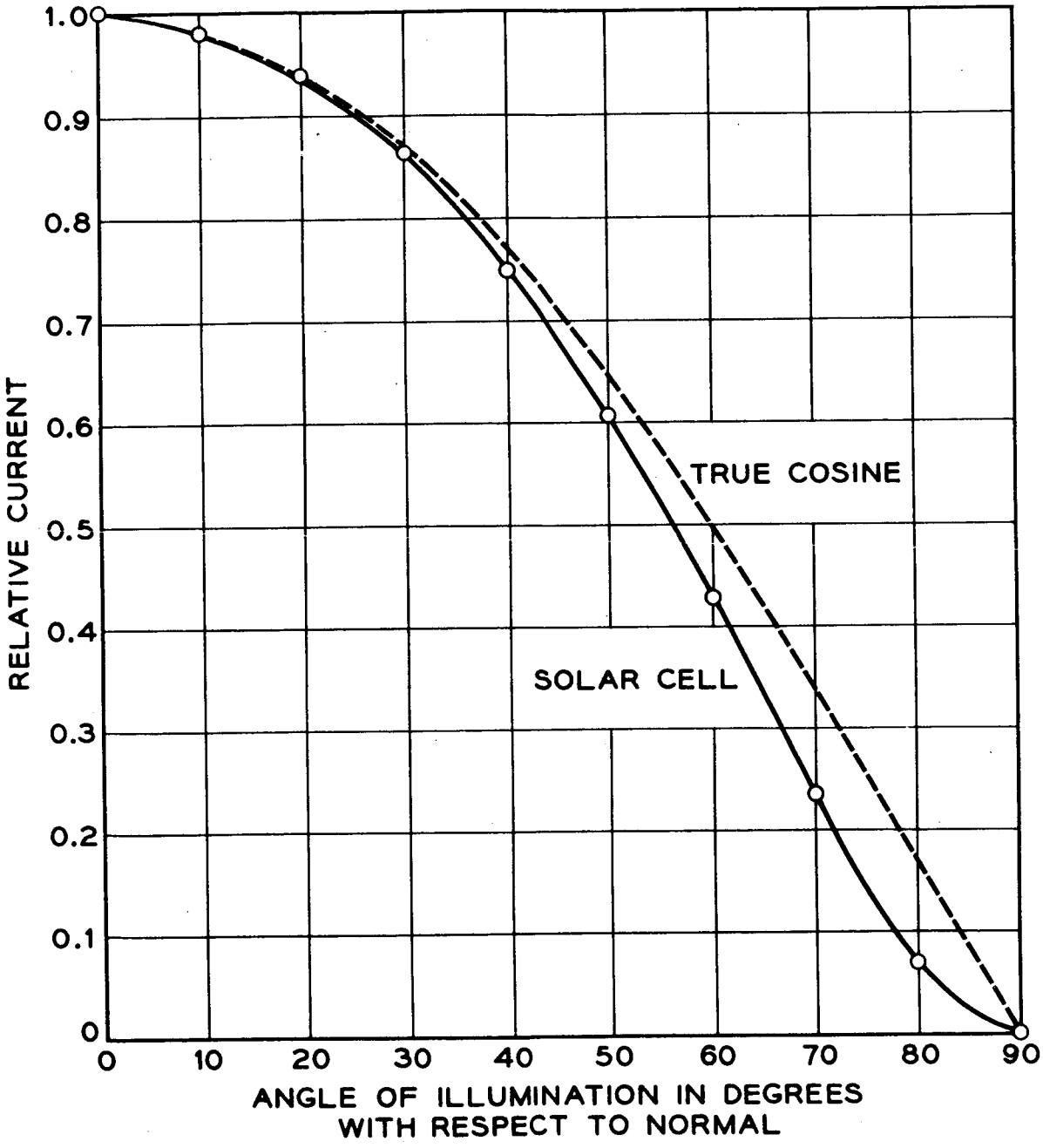

Fig. 3-~~18~~ 19

N86 26-6
6

PUBLICATION: BSTJ
AUTHOR: W. L. Brown, Et Al.
FIGURE NO.: 2 DATE: APR 63

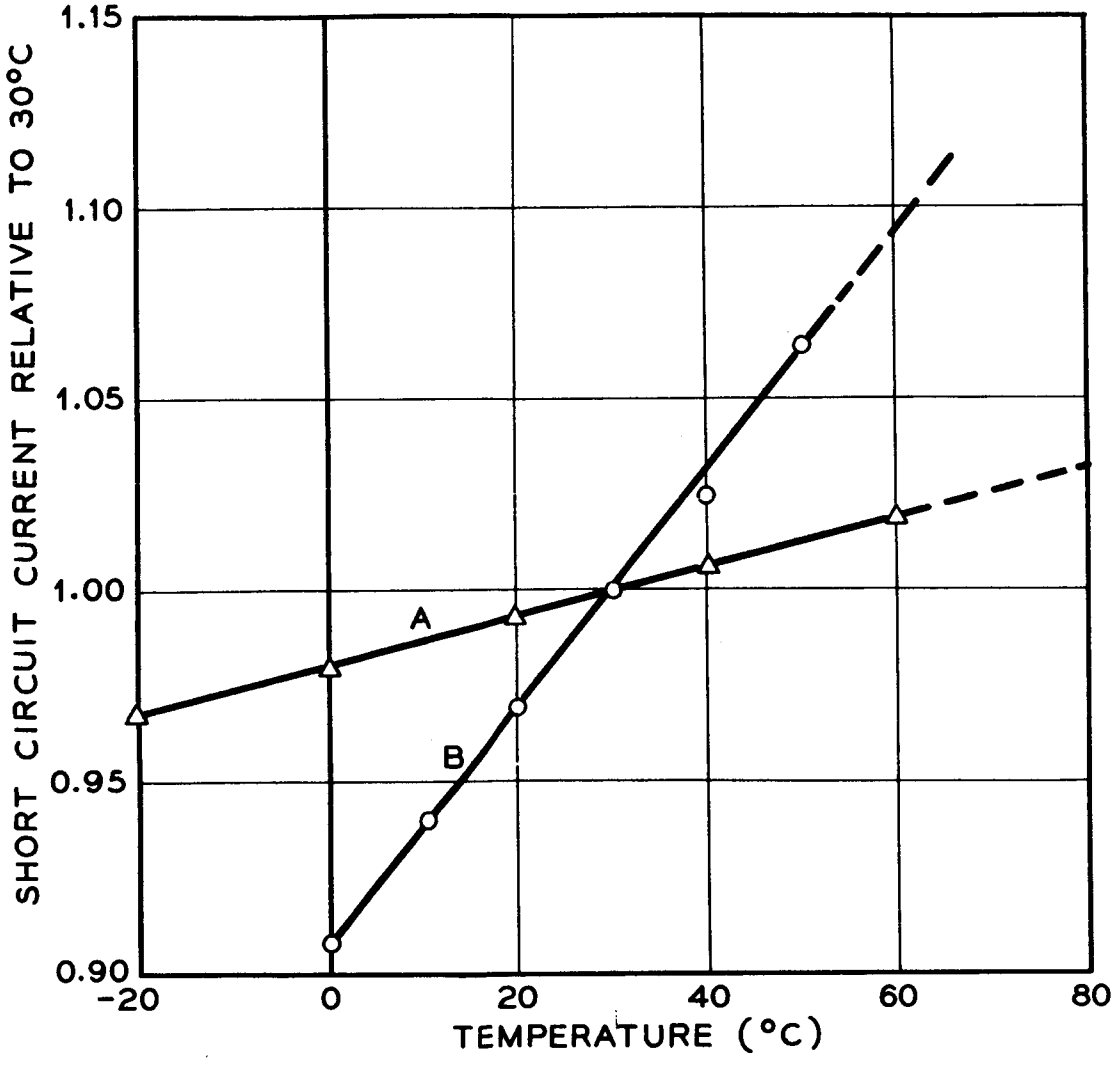
1.15
1.10
1.05
1.00
0.95
0.90
SHORT CIRCUIT CURRENT RELATIVE TO 30°C
A
B
-20
0
20
40
60
80
TEMPERATURE (°C)

Fig. 3-20

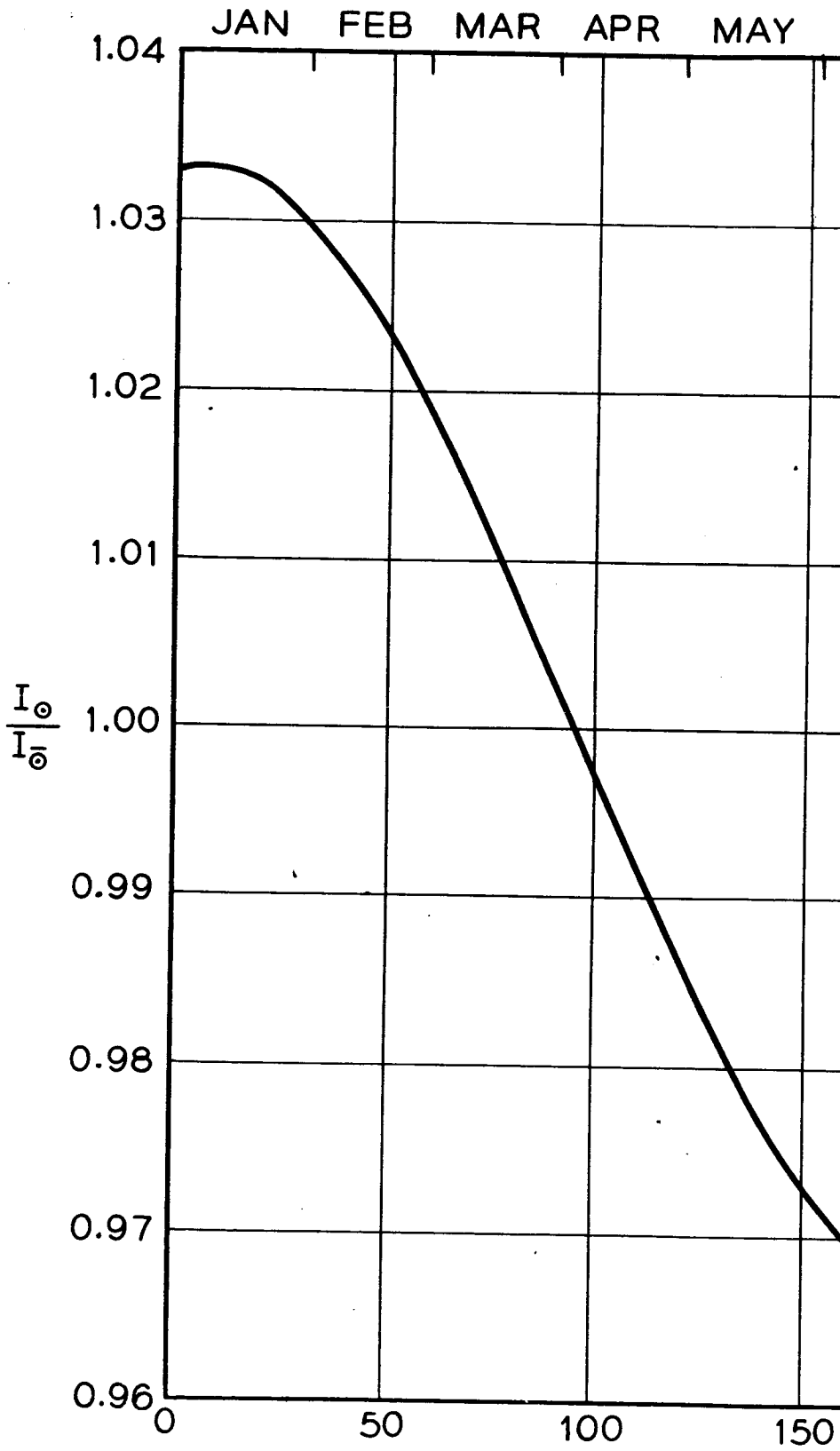
JAN
FEB
MAR
APR
MAY
1.04
1.03
1.02
1.01
1.00
0.99
0.98
0.97
0.96
$\frac{I_\odot}{I_{\bar{\odot}}}$
0
50
100
150

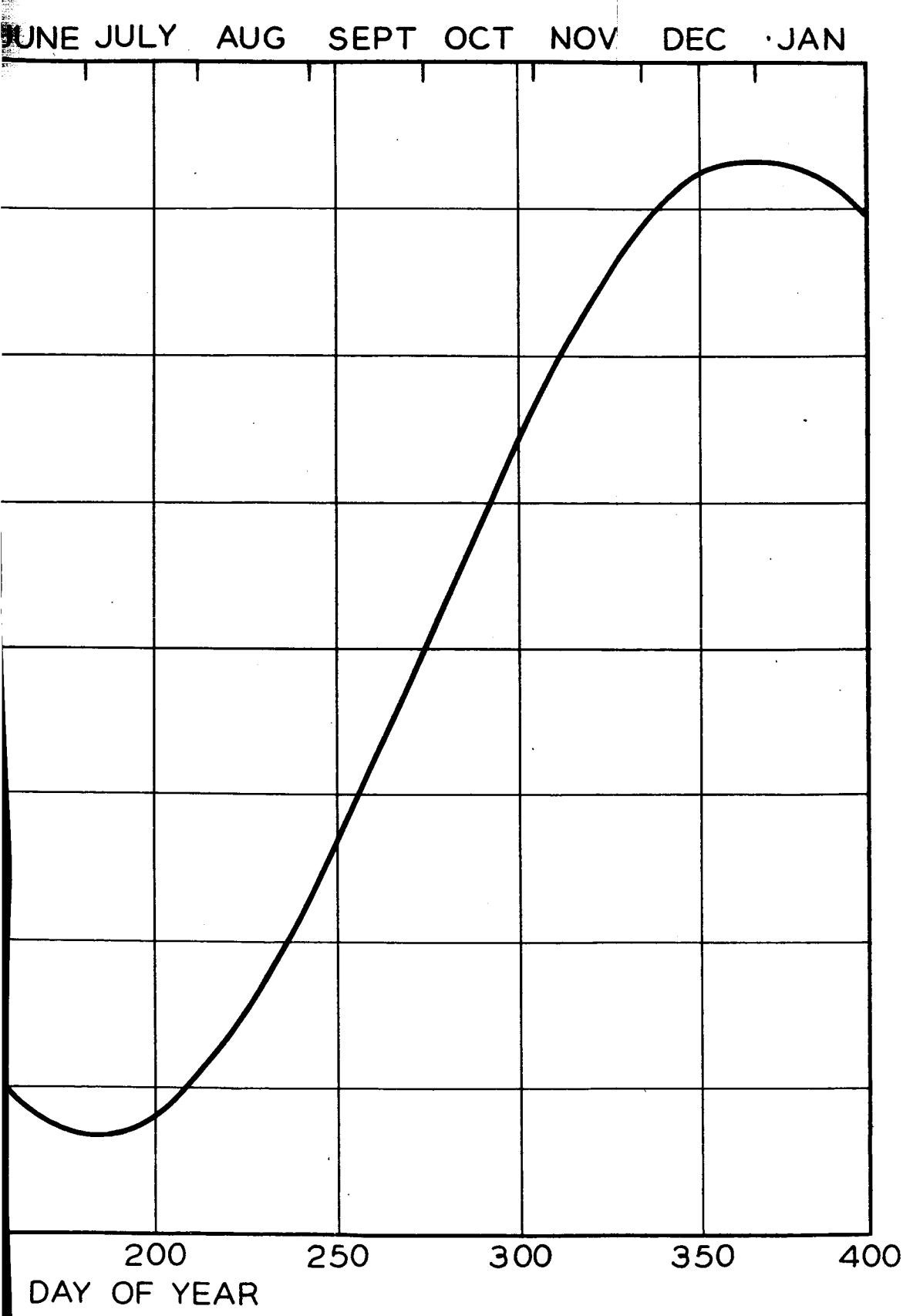
JUNE JULY AUG SEPT OCT NOV DEC JAN
200
250
300
350
400
DAY OF YEAR

Fig. 3-21

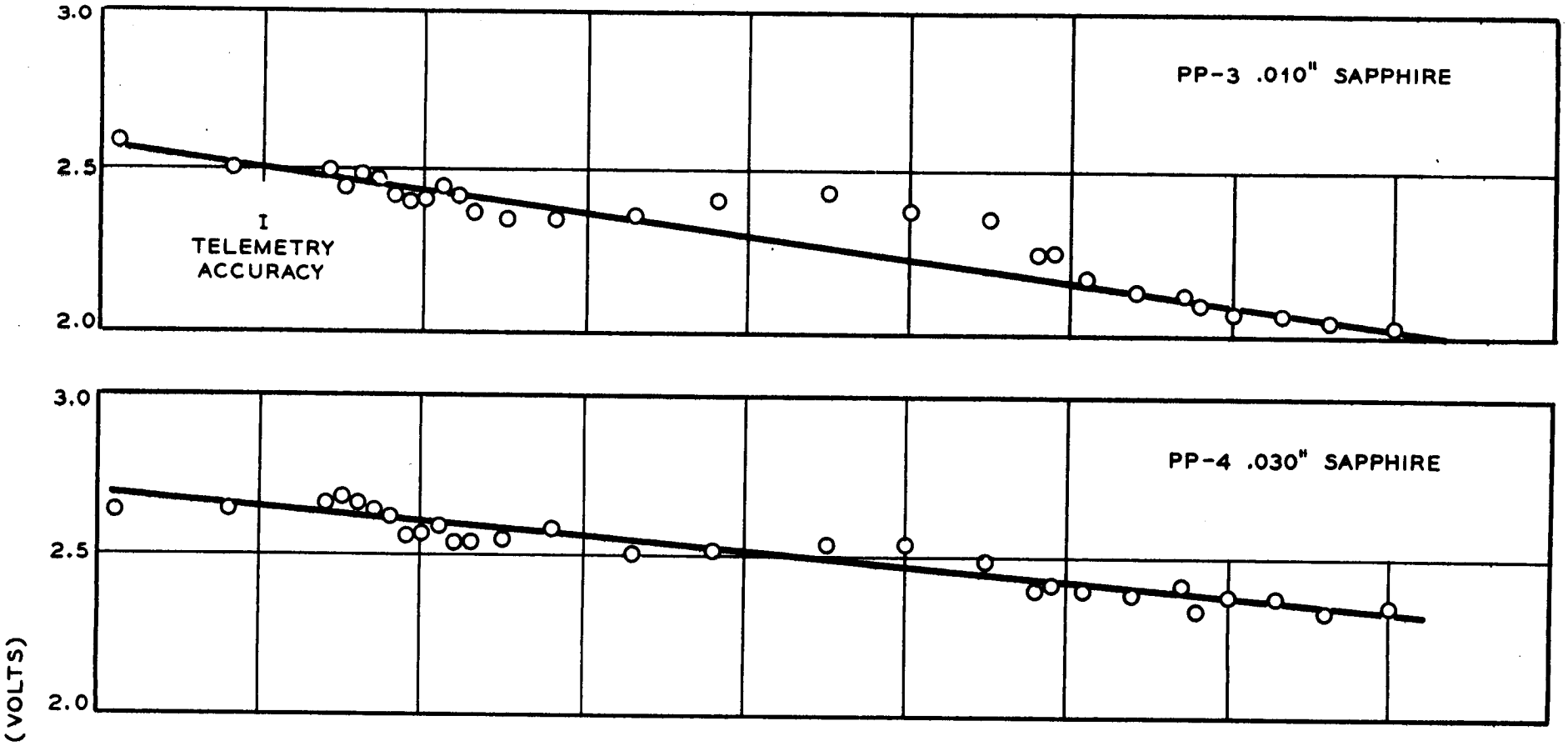
3.0
2.5
2.0
PP-3 .010" SAPPHIRE
I
TELEMETRY
ACCURACY
3.0
2.5
2.0
PP-4 .030" SAPPHIRE
(VOLTS)

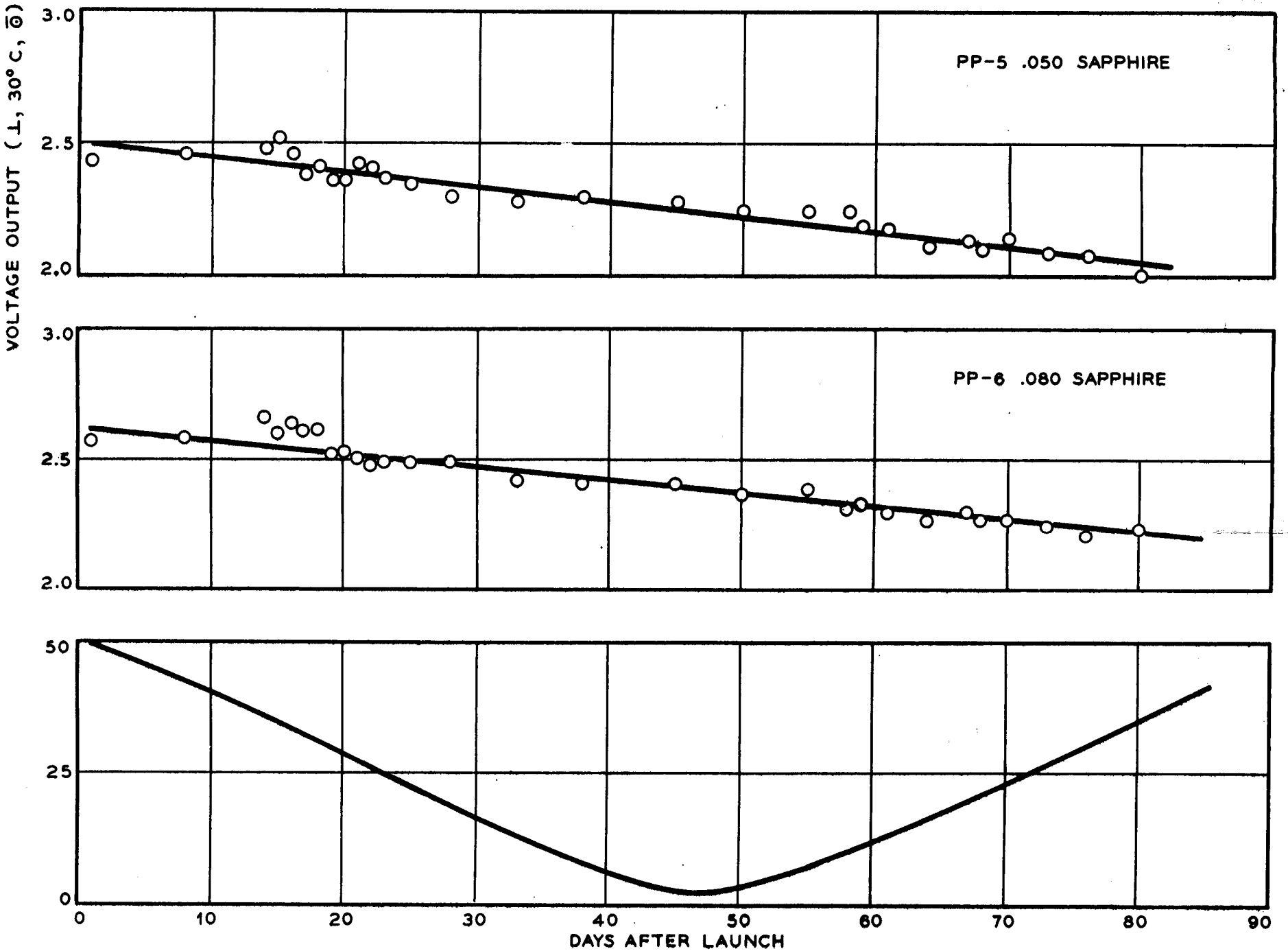
VOLTAGE OUTPUT (⊥, 30° C, ⊙)
3.0
2.5
2.0
PP-5 .050 SAPPHIRE
3.0
2.5
2.0
PP-6 .080 SAPPHIRE
50
25
0
0
10
20
30
40
50
60
70
80
90
DAYS AFTER LAUNCH

Fig. 3-22

BELL TELEPHONE LABORATORIES
INCORPORATED

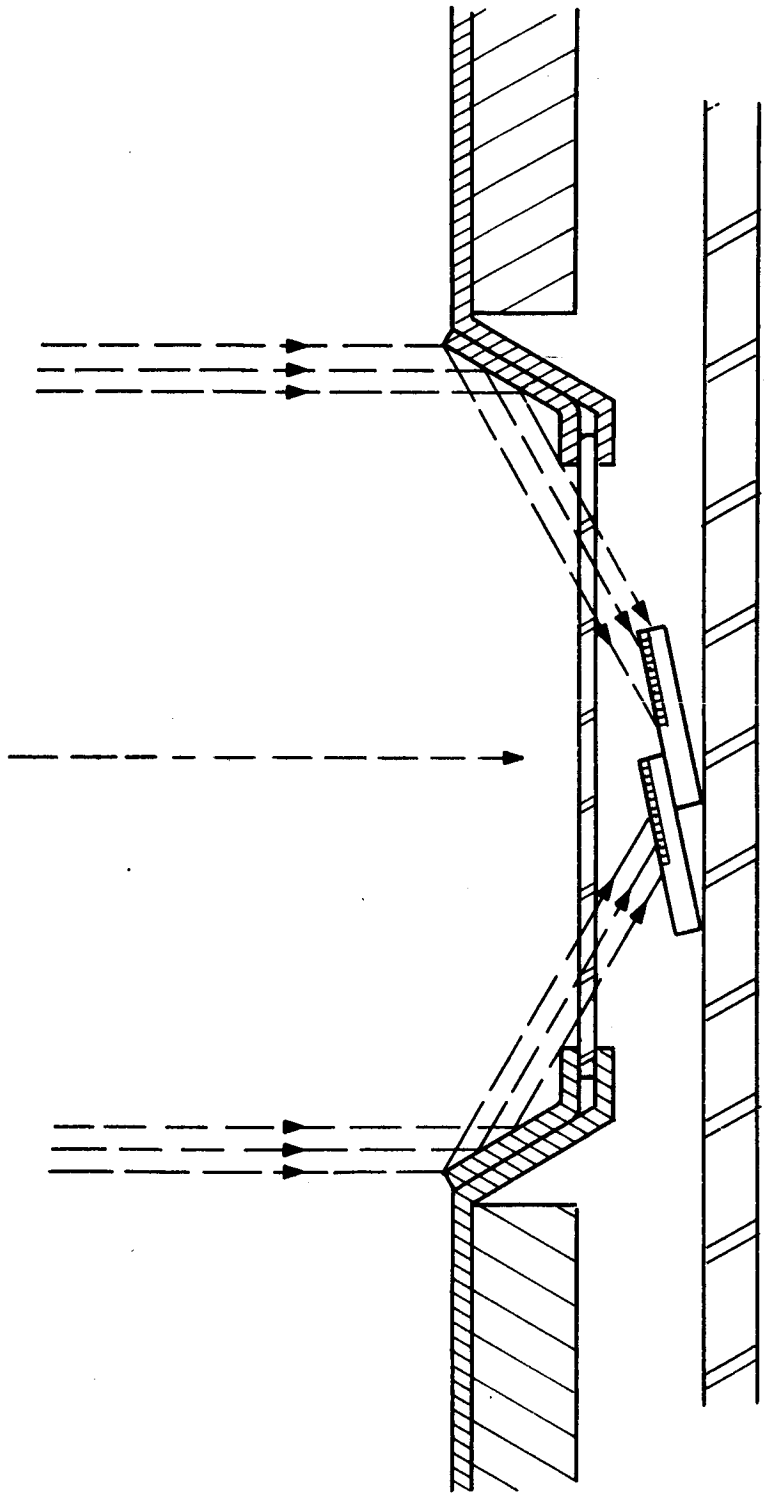

Fig. 3-23

			ENGR
			DRAWN
		DATE	CASE

OGILVIE PRESS, INC. PI 128
PRINTED IN U.S.A. E-7544 (8-60)

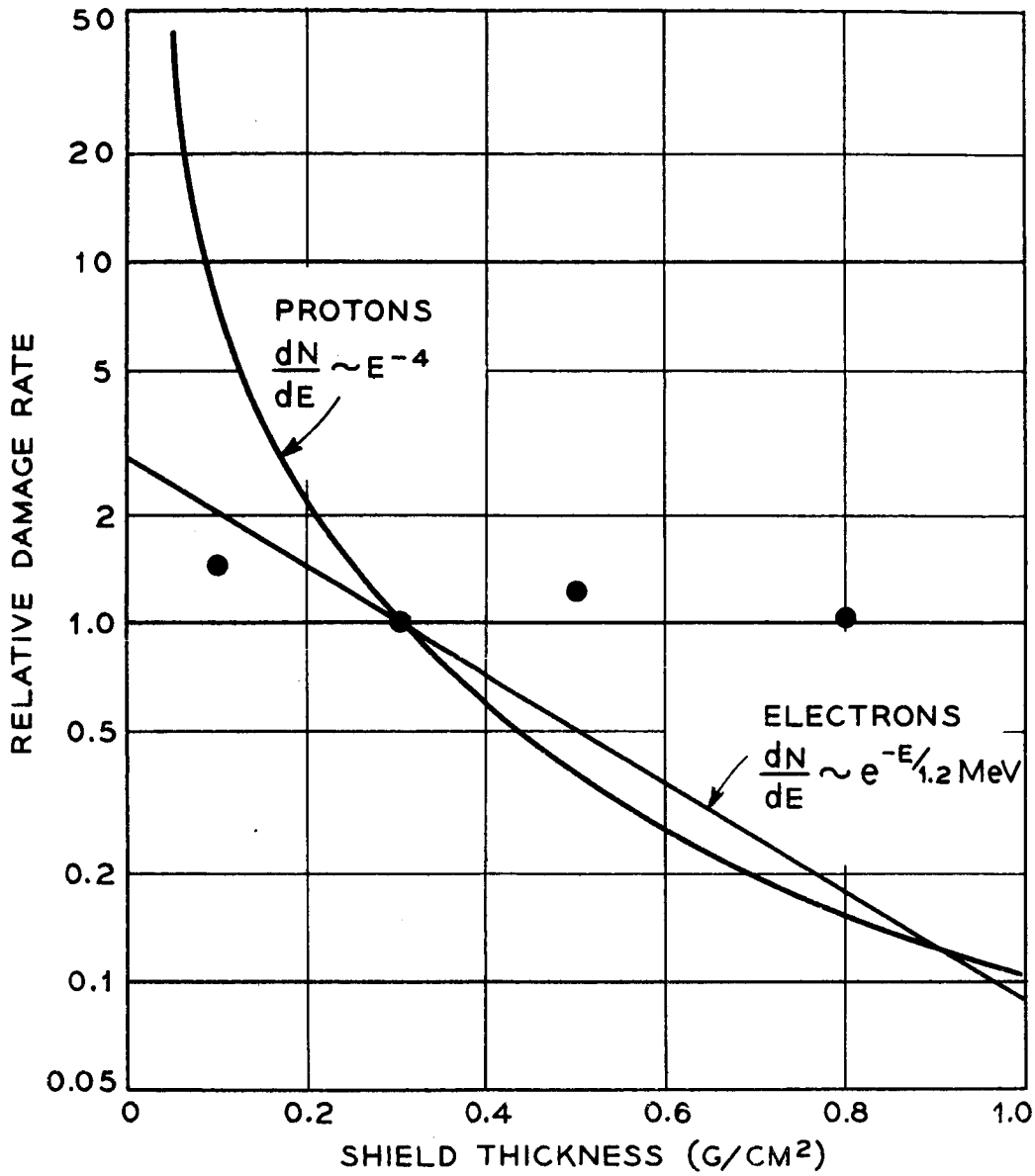

Fig. 3-24

		ENGR
		DRAWN
	DATE	CASE